Faculty of Mathematics and Physics, Charles University, Prague

and

Institute of Radio Engineering and Electronics,
Academy of Sciences of the Czech Republic
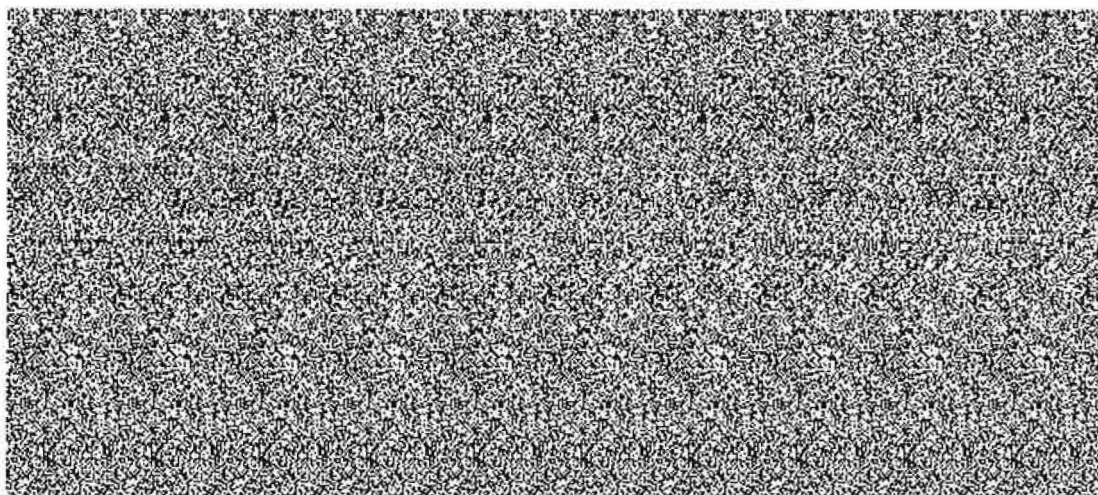
Radan Slavík

SPECTRAL FIBER OPTIC SENSOR BASED ON SURFACE PLASMON RESONANCE

Ph.D. THESIS

Prague 2000

Prague, 9/3/2000

Radan Slavík

Contets

1. Introduction

Optical sensors are devices that allow measuring variations of a desired quantity by optical means. Even non-optical quantities may be measured, if a change in the quantity of interest is converted into a change in an optical quantity. Optical sensors have been demonstrated for measurement of numerous variables such as pressure [1], temperature [2], flow [3], vibration [4], electric and magnetic fields [5], linear and rotary displacements [6], velocity [3], chemical concentration [7], pH [8], and partial pressure of gases [9]. Optical sensors offer several advantages over other methods. Generally, they could be operated in (chemically) aggressive environments due to the inertness of the used materials (glass, plastics, etc). Because optical sensors do not require electrical signal in the sensing region, they can be operated also in hazardous environments. Moreover, their performance is insensitive to electromagnetic interference. As the optical wave usually does not change the medium being measured, optical sensors may be used for in situ analysis. Optical sensors also hold potential for remote sensing and multi-point measurement via distributed sensors and sensor networks.

In most optical sensors, an optical wave emitted from an appropriate light source enters the sensing region, where it is changed by variations in the measured quantity. These changes include changes in the light amplitude, wavelength, phase or polarization. The light amplitude changes can be measured by standard light intensity detectors [10]. Measurement may be also performed at several wavelengths in order to improve the signal-to-noise ratio [11]. Phase changes may be monitored by various interferometric detection techniques based on Michelson [2], Sagnac [6], Fabry-Perot [12] or Mach-Zehnder [13] interferometers. Changes in the wavelength of the radiation are measured by heterodyne detection [3], using a spectrum analyzer [14], etc. Polarization changes are usually measured using polarization selective devices and elements, such as crossed polarizers [15]. The sensing process is often, especially in chemical sensors and biosensors, indirect - changes in the quantity to be measured change optical properties of a *transducer* and the optical wave is consequently modulated by this change.

There are two types of interrogation of the *analyzed medium,* which refers to all the sensor parts changed due to the sensing event, by the light wave. Either the light wave passes through the analyzed medium or the interaction is realized through the evanescent field of the light wave. The advantage of the first approach is that the interaction can take place in the whole volume of the analyzed medium, but, on the other hand, it requires transparent media. The latter method does not require transparent media, but only a fraction of the light wave power interacts with the analyzed medium, which may reduce the sensor sensitivity. On the other hand, the evanescent field-based methods probe processes only within a limited distance from the sensing element making the measurement insensitive to background interference effects.

Optical sensors have benefited tremendously from the development of optical waveguides, especially optical fibers [16]. The use of optical fibers allows the preparation of sensors with miniature sensing elements, usually referred to as *optodes,* where electric and electro-optic components of the sensor (source and detector) may be remote. The interaction of the light wave in the optode is then completely electronically passive and cannot be disturbed by electromagnetic interference in the vicinity of the

optode. Other advantages of optical fibers include geometrical versatility enabling fiber optic sensors to be configured in a variety of shapes, low weight and small volume.

Optical fiber sensors can be classified according to the way in which the optical fiber is used. *Extrinsic* optical fiber sensors use optical fibers to guide light to and from the optode. The optode of an extrinsic fiber optic sensor is an assembly usually based on miniature conventional optical components, which is designed to modulate the properties of the light wave in response to changes in the analyzed medium. These sensors can benefit from the evanescent wave interaction as well as from direct interaction of the light wave with the analyzed medium. The other family of optical fiber sensors are *intrinsic* fiber optic sensors, which utilize direct modulation of the light wave guided in the fiber. The light does not leave the fiber, except at the detection end (the output) of the sensor. In intrinsic sensors, the quantity of interest modifies characteristics of the optical waveguide and affects the light carried by the fiber. Standard optical fibers are, however, designed to prevent such effects, which are undesirable in communication systems. Therefore, it is necessary to use either special fibers or packaging, or a more sophisticated sensor system designed to be sensitive to specific perturbations. Intrinsic sensors are generally evanescent interaction based, though there are some exceptions (critical angle fiber optic refractometers, porous fiber core based sensors, fiber Bragg grating tension and temperature sensors, etc.).

The fraction of power carried by the evanescent field in standard fiber optic structures is rather small (typically less than 10 percent). It limits the sensitivity of intrinsic fiber optic sensors based on the interaction between the evanescent field of guided modes and the analyzed medium. This can be overcome by employing a more sophisticated high-resolution schemes and by increasing the evanescent field, respectively. A typical example of a high resolution scheme is interferometry [2]. The evanescent field can be increased by the use of specially designed waveguide structures (e. g., waveguides with a high refractive index overlayer [17]) or by intermodal conversion transferring the radiation predominantly in guided modes which exhibit stronger evanescent field. The latter can be realized, for example, by using modes of free space (decoupling the light from the waveguide [18]). Alternatively, one can exploit special surface waves allowing concentration of vast part of optical radiation in the analyzed medium, such as surface *plasma waves* (**SPW**) [19].

1.1 Optical Biosensors

Main challenges in bioanalysis are very low chemical concentrations of biological analytes which need to be measured. Measurement of concentrations ranging from 10^{-10} M (IgG in blood) up 10^{-17} M (insulin in blood) [20] is desired. In addition, the analyte is contained in a complex media (e. g., blood) often interfering the measurement.

Traditional analytical biochemical methods, e. g. enzyme-linked immunosorbent assay (ELISA) [21], are, in principle, indirect, encompassing several consecutive steps. In first step, a sample containing analyte molecules is brought into contact with receptor molecules specifically interacting with the analyte molecules (usually antibodies), which are immobilized on a substrate surface. The next step includes washing of the substrate to remove the sample leaving only the analyte molecules bound to the immobilized receptor molecules. Then the substrate is incubated with a solution in which labeled molecules or enzymes capable of specific binding to the analyte are

4

present. After washing out this solution, the concentration of the bound-labeled molecules or enzymes is measured. The concentration of the labeled molecules is usually measured directly. To measure the concentration of enzymes, the substrate is incubated with a solution containing molecules which in the presence of the enzyme produce a compound with a characteristic spectral absorption, which is eventually optically detected providing information on the amount of the bound analyte. Though techniques such as ELISA attain high resolution and specificity, they cannot perform in situ nor real-time measurement. On the contrary, they are rather time consuming, requiring typically several hours for the analysis.

Biosensors are sensors that are capable of measuring biochemical quantities (e.g., antibody concentration), usually in a biological medium (e.g., whole blood, serum, urine, and tissue). In the sensing region they incorporate a biochemical compound (enzyme, antigen), which can recognize and specifically bind analyte of interest.

In principle, biosensing can be either direct or indirect. In direct optical biosensors, binding of analyte onto functionalized sensor surface results in a slight change in the refractive index in the vicinity of the sensor surface which is directly measured by optical means. Indirect optical biosensing usually involves a pre-detection sample treatment linking the analyte molecules with compounds, the concentrations of which may be measured directly. Frequently, fluorescent compounds (labels) are attached to the analyte molecules and the analyte concentration is determined through the measurement of concentration of the bound labels. Modern fluorescence-based sensing systems offer high sensitivity making the detection of very low analyte concentrations possible [22].

Optical biosensor technologies capable of direct detection of bioanalytes include sensors based on the excitation of an SPW, grating coupling into an integrated optical waveguide, integrated optical interferometry and resonance effects in multilayer dielectric mirrors. The excitation of an SPW manifests itself as damping of light reflected at a metal-dielectric boundary for specific angle of incidence or wavelength, which is changed by changes of the propagation constant of the SPW. The propagation constant of the SPW is strongly affected by the analyte placed in the region of the SPW evanescent field [23,24]. In the grating coupler, the analyte immobilized onto an integrated optical waveguide changes through the evanescent field the propagation constant of a guided mode. It leads to variation in the angle at which the light is coupled into the waveguide via the coupling grating [25]. Biosensors based on interferometry use in most cases a two-beam interferometer, where the light wave propagating in one interferometer arm changes its phase due to interaction with the analyte, which affects the interference pattern at the output. In biosensing, the integrated optical Mach-Zehnder interferometer, which utilizes the evanescent-based interaction, is the most convenient configuration [26,27]. The resonant mirror is a leaky planar waveguide that uses attenuated total internal reflection to couple light into and out of the waveguiding layer. The coupling is dependent on the polarization, wavelength and angle of the incident light. The binding of analyte produces a change in the effective refractive index of modes of the structure altering the coupling condition. This change may be determined through measuring changes in the polarization of optical wave, for instance by using crossed input and output polarizers [28,29].

Direct biosensing methods offer several advantageous features such as rapid analysis, reagentlessness, and potential for continuous monitoring. Major drawbacks include sensitivity to interference effects producing background refractive index variations (e.g. temperature and sample composition variations) and adsorption of non-target molecules on the sensor surface (non-specific adsorption). This might be overcome by multichannel detection allowing compensation for changes not attributed to the sensing event. The multichannel detection is usually realized by employing special geometry of the sensing element (for example, [30]).

Currently, biosensors attract increasing interest as they may provide new tools for bioanalysis offering advantages of in situ, simple, fast, and multicomponent analysis. Biosensors are targeted mainly at medicine for clinical analyses and at in vivo measurements. Other applications include biotechnology, environmental monitoring, drug and food screening. A more detailed overview of methods used in biosensing may be found, for example, in [20].

1.2   Optical Sensors with Surface Plasma Waves

SPW is a charge density oscillation that may exist at the interface of two media with dielectric constants of opposite signs, for instance, a metal and a dielectrics. The charge density wave is associated with an electromagnetic wave, the field vectors of which reach their maxima at the interface and decay evanescently into the both media (Fig. 1.2.1). The SPW is a TM polarized evanescent wave. Owing to high loss in the metal, the SPW propagates with very high attenuation in the visible and near infrared spectral region. In this spectral region, majority of power of the SPW is carried by the dielectrics. The propagation constant of the SPW is always higher than that of the optical wave propagating in the dielectrics. As a consequence, the SPW cannot be excited directly by an incident optical wave at a planar metal-dielectric interface. To excite the SPW by an optical wave, a coupler has to be used.

The SPW couplers are most commonly based on the attenuated total reflection (**ATR**) – *an ATR coupler*, or on diffraction on a grating – *a grating coupler*. As the excitation of the SPW by an optical wave results in resonant transfer of energy into the SPW (**SPR- surface plasmon resonance**), SPR manifests itself by resonant absorption of energy of the optical wave. Owing to strong concentration of the SPW electromagnetic field in the analyzed medium (usually over 90 percent of the total power), the propagation constant of the SPW and consequently the SPR condition are very sensitive to variations in the spatial profile of the refractive index of the analyzed medium. Therefore, variations in the spatial profile of the refractive index of the analyzed medium strongly affect the SPR dip position (Fig. 1.2.1), which is measured by observing the interaction between the SPW and the optical wave. As the SPW is an evanescent wave, sensors based on the SPR utilize evanescent interaction with the analyzed medium.

In the following part an overview of SPR-based sensors is given. In order to compare various sensor configurations, several parameters have to be defined. The two most important parameters are *sensitivity* and *resolution*. The sensitivity is defined as a change in the detected parameter (for example, amplitude) to the unity change in the measured parameter (for example, chemical concentration). The resolution is defined as the ultimate value of the measured parameter which can be resolved with the sensor. Other important sensor parameters are *response time, selectivity* and *reversibility*. These parameters are influenced mainly by transducers.
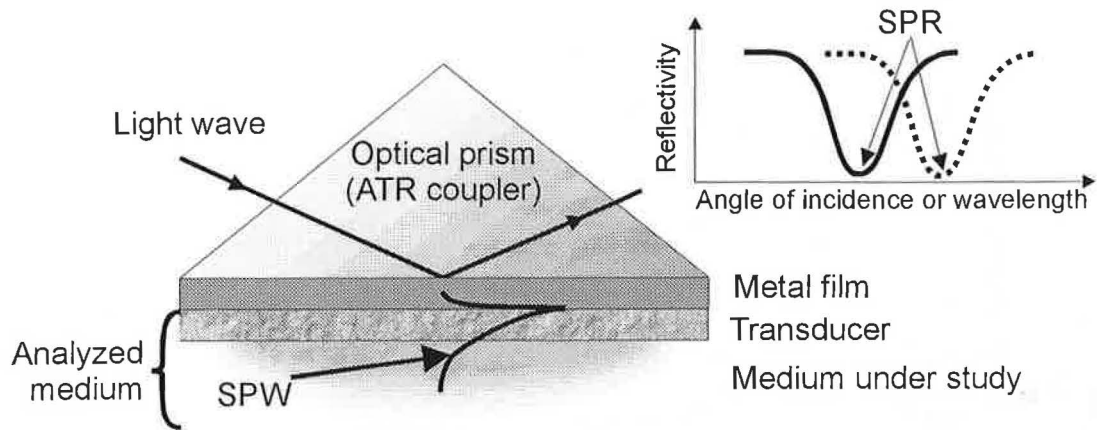
Fig. 1.2.1 ATR method in the Kretschmann geometry and its response to different spatial profiles of the refractive indices of the analyzed medium.

The utilization of the SPW in sensing was pioneered by Nylander et al. in 1982 [31]. They utilized the Kretschmann geometry of the ATR coupler (Fig. 1.2.1), which has been up to now (review [32] and reference therein) the most common configuration of the SPR sensors. Its popularity may originate in its relative simplicity combined with high sensitivity [33].

There are several approaches that utilize resonant transfer of energy into the SPW in the ATR coupler. In the first one the SPW is excited by a monochromatic light incident at a fixed angle. As follows from Fig. 1.2.2, a change in the refractive index of the analyzed medium causes a change in the reflected light power of the intensity measured in the neighborhood of the resonance. The changes in the refractive index of the analyzed medium are then monitored by measuring the intensity of the reflected light [31,34,35]. The intensity measurement is simple, but, generally, not very suitable for sensing as any system instability results in changes in the detected intensity, which may significantly decrease the sensor resolution. The second approach uses a fixed angle of incidence and broadband incident light. The changes in the refractive index of the analyzed medium cause a shift in the SPR spectral position (Fig. 1.2.2), which is monitored by spectral analysis [36,37]. Using a white light source and a spectrum analyzer as a detector, a sensor without any moving parts may be built. Moreover, this configuration allows the use of multimode optical fibers for delivering light from the source to the optode and from the optode to the detector (spectrum analyzer). In this way an extrinsic fiber optic sensor may be constructed [11]. The reported experimental sensitivity is 10^4 nm/RIU (**RIU** is an acronym for refractive index unit) with a wavelength resolution of 0.02 nm, which results in a resolution of 2×10^{-6} RIU [38]. The third approach utilizes the fact that the SPR dip similar to that in Fig. 1.2.2 can be obtained also by varying the angle of incidence if monochromatic incident light is used [19]. In this approach the angle of incidence is scanned around the SPR and the SPR dip position is then interpolated [23,39]. The angle of incidence that corresponds to the SPR can be found by rotating the ATR coupler [31] or by using a convergent beam of incident light and an array of photodetectors at the output [39]. The second approach is more advantageous, because the device does not comprise any moving parts. The reported experimentally achieved sensitivity is 160 deg/RIU with an angular resolution of 10^{-4} deg, which leads to a sensor resolution of 6×10^{-7} RIU [23,24].
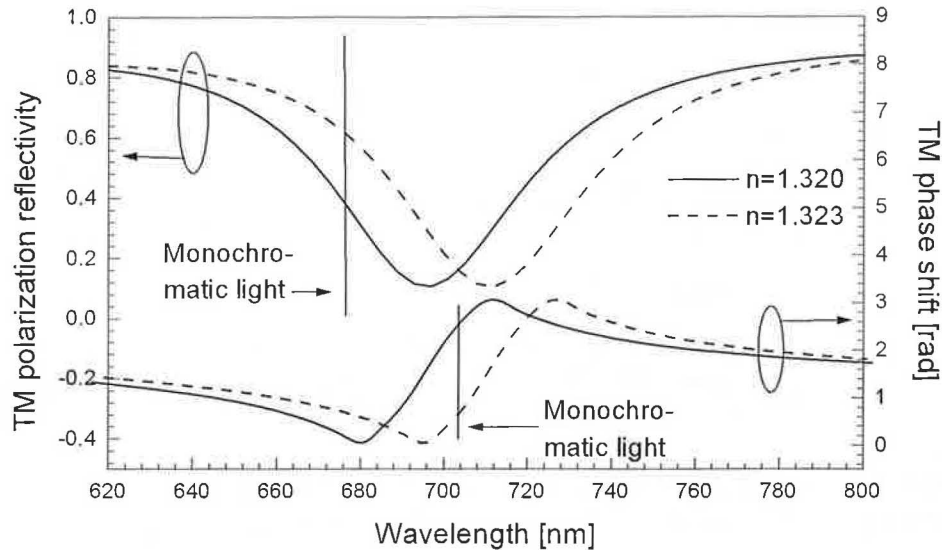
Fig. 1.2.2 Amplitude and phase response of an optical wave in the ATR coupler in the Kretschmann geometry (Fig. 1.2.1) to different refractive indices of homogenous analyzed medium for the following parameters: angle of incidence – 67 deg, optical prism made of BK7 glass and 50 nm thick gold film.

Other detection approaches utilize the fact that the phase of the TM reflected wave is affected as well as the amplitude under the SPR (Fig. 1.2.2). This phenomenon appears very attractive for sensing as detection schemes based on interferometry usually offer very high resolution. Recently, several schemes of SPR sensors in which phase monitoring is utilized were published [40,41,42]. In [40] the incident light wave is not TM polarized, as is usual in the above mentioned approaches, but comprises TM as well as TE polarized components. As the TE polarization is not affected by the SPR, it is used as a reference necessary for interferometric detection. An additional reference channel monitors the variations in the laser source wavelength. In [41] a more sophisticated detection scheme based on heterodyne detection is employed in order to compensate for wavelength and amplitude instability of the laser and perturbations in the system. The reported experimentally achieved sensitivity is 5×10^4 deg/RIU with a detection system capable of detecting a phase change of 2.5×10^{-2} deg, which leads to the sensor resolution of 5×10^{-7} RIU [41]. Generally, SPR sensing devices based on phase interrogation may provide better sensitivity than amplitude-based SPR sensors, although more sophisticated detection schemes need to be employed.

The theoretical sensitivity and resolution of the ATR-based SPR sensors for two different wavelengths are given in Table 1.2.1 [32]. As a model system, an ATR coupler made of BK7 glass, a 50 nm gold film (optical constants taken from [43]) and an analyzed uniform medium with a refractive index value of 1.32 (aqueous environment) are used. The gold film surfaces are assumed to be ideally smooth. The resolution is calculated assuming a detection system which can resolve changes of 0.2 percent in the power [44], changes in the SPR angle of 10^{-4} deg [24], an SPR wavelength change of 0.02 nm [38], and a change of 2.5×10^{-2} deg in the phase [41]. From Table 1.2.1 it follows that the resolution of SPR sensors should be better than 10^{-6} RIU and also that the proper choice of the wavelength depends on the detection scheme. For example, angular and phase interrogating systems show higher sensitivity for shorter wavelengths

8

while amplitude and wavelength interrogating systems exhibit higher resolution for longer wavelengths.

Table 1.2.1 Refractive index sensitivity and resolution of the ATR-based SPR sensors

INTERROGATION:		SENSITIVITY	RESOLUTION
Amplitude	λ=630 nm	180 dB/RIU	5×10^{-5} RIU
	λ=850 nm	690 dB/RIU	1×10^{-5} RIU
Angular	λ=630 nm	191 deg/RIU	5×10^{-7} RIU
	λ=850 nm	97 deg/RIU	1×10^{-6} RIU
Wavelength	λ=630 nm	970 nm/RIU	5×10^{-5} RIU
	λ=850 nm	1.4×10^4 nm/RIU	1×10^{-6} RIU
Phase	λ=630 nm	1.2×10^5 deg/RIU	2×10^{-7} RIU
	λ=850 nm	4×10^4 deg/RIU	6×10^{-7} RIU

The fact that the SPW supporting metal film is never ideally smooth, as assumed in the presented theoretical considerations, leads mainly to broadening and deforming the SPR dip rather than to affecting the position of the SPR [19]. This agrees well with the fact that the experimentally achieved sensitivities in the angularly and spectrally interrogating systems, which monitor the SPR position, are similar to the theoretically predicted values (Table 1.2.1) (for example, [11, 39]). The SPR dip broadening, however, reduces the steepness of the arms of the SPR dip as well as the steepness of the phase response, which reduces the experimentally achieved sensitivity and resolution of systems based on amplitude and phase interrogations.

The grating SPW coupler is shown in Fig. 1.2.3. The diffraction on the grating may add the required momentum to the incident optical wave in order to match that of the SPW, and thus SPR may occur [45]. Grating-based optical SPR sensors employing light intensity monitoring [46,47] and wavelength interrogation [48,49] have been demonstrated. Although the interrogation of SPR in optical systems using prism and grating coupler are the same, accurate control of the thickness of the plasmon-active metal film is not necessary in the grating-based SPR sensors. The possible smaller popularity of grating coupler may originate in the fact that the incident light beam propagates through the sample solution. Sensitivity of wavelength interrogation-based SPR sensors with grating couplers is several times smaller than those with prism couplers. In the angular interrogation mode, sensitivity of SPR sensors based on prism and grating couplers are comparable [33].
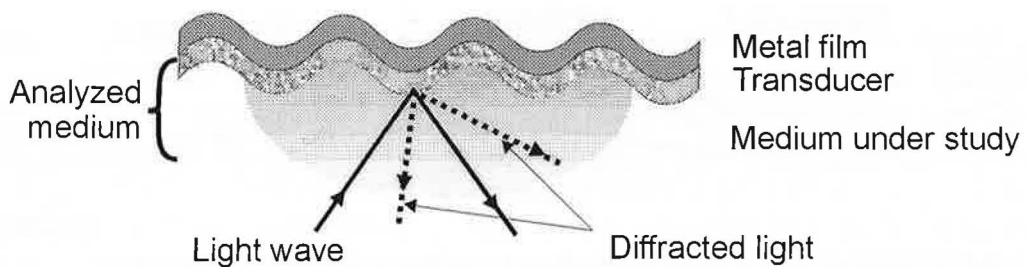

Fig. 1.2.3 Grating coupler for the excitation of the SPW.

A biosensor based on SPR was first reported in 1983 [34]. Since then, many biomolecular interactions like antigen-antibody, receptor-ligand, and hormone-receptor binding were studied using SPR biosensor technology [50]. Usually one compound (for example, antibody) is immobilized on the sensor surface forming the chemo-optical transducer. Binding of the analyte molecules (for example, antigen) presented in the medium under study, changes the refractive index profile near the SPW supporting metal surface and thus also the SPR condition. The chemo-optical transducer may be formed in several ways. The most popular techniques are the immobilization of streptavidin with biotin on the metal surface further functionalized with biotinylated receptors [51], formation of self assembled monolayers of thiol molecules [52] in order to introduce important biological substituents as tail groups to which receptors are covalently attached, and spreading out liposomes on the hydrophobic metal surface.

Several SPR sensing, mainly those based on the ATR configuration, are already commerically available. The BIAcore AB, Sweeden, brought as the first their biosensor on the market in 1990 [50]. This sensor utilizes angular interrogation with a convergent incident light beam and a CCD detector. It has four independent parallel sensing channels. This sensor is also very stable, which leads to high resolution of 3×10^{-7} RIU. This device, which comprises also a very advanced sensed media delivery system, is targeted mainly at research. In recent years there have appeared a large number of other commercially available SPR sensors, e. g., Texas Instruments (USA) [53] SPR sensor utilizing angular interrogation. The used source, prism and photodiode array are integrated into a single chip, which, however, makes the chip rather expensive. Among others, sensors produced by BioTuL Bio Instruments GmbH (Germany) [54] with eigth channels, by Quantech (USA) [55], and by Xantec Analysensysteme GbR (Germany) can be mentioned. An increasing number of commercialized SPR sensors is witnessing great potential of these devices. However, up to now commercialized SPR sensors have been relatively expensive, bulky, and generaly laboratory table-top.

The current trends in SPR sensing are miniature sensors and sensors capable of a multicomponent analysis. The sensor miniaturization may broaden the range of sensor applications and also reduce the price. The multicomponent analysis may speed up analysis of complex samples resulting in the reduction of analysis time and costs.

Logically, but not historically, the first step towards these aims was device referred as *light pipe* [30,56,57]. This device consists of an ATR coupler, where instead of the prism a glass slide is used, Fig. 1.2.4. The light wave undergoes several total internal reflections allowing for multicomponent analysis as sketched in Fig. 1.2.4.
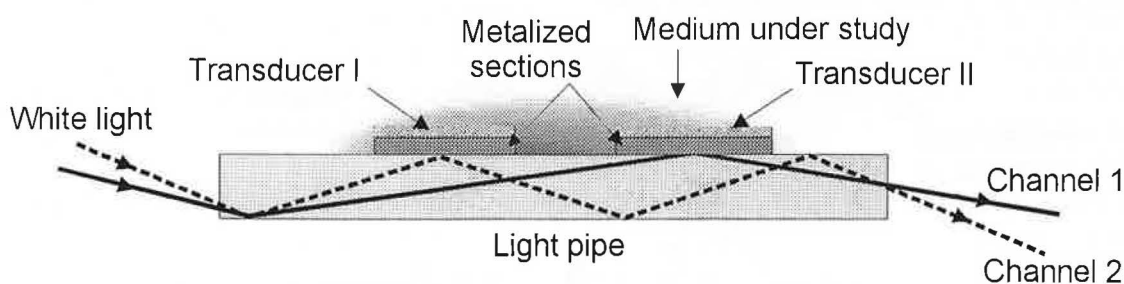

Fig. 1.2.4 Scheme of planar light pipe allowing multicomponent analysis [30].

Excitation of an SPW by light guided in a waveguide is the further step in sensor miniaturization. The process of the SPW excitation in optical waveguide-based intrinsic SPR sensing structures is, in principle, similar to that in the light pipe. A light wave is guided by the waveguide and enters the region with a thin metal film. It evanescently penetrates through the metal film and, if the SPW and the guided mode are phase-matched, it excites the SPW at the outer interface of the metal film. Theoretically, the sensitivity of waveguide-based SPR devices is approximately the same as that of the corresponding ATR-based sensors. Despite certain lack in degrees of freedom compared to bulk prism-based SPR sensing devices, all the main SPR detection approaches have been implemented into waveguide SPR sensors. The intrinsic waveguide SPR sensors can be divided into two major groups – sensors based on integrated optical waveguides and on optical fibers.

Research into integrated optical waveguide SPR sensors was pioneered in the late eighties [58]. Since then, various groups have developed SPR sensing devices using slab [59] and channel [60] single-mode or few-mode integrated optical waveguides. Channel waveguide technology also allows more optical elements to be incorporated in a single glass substrate (e.g., couplers), which can be with advantage utilized for creating a reference channel [61] or even more sophisticated sensing structures [61] with potential for multichannel analysis. An intensity-based integrated optical waveguide SPR sensing device with a sensitivity of 2000 dB/RIU has been reported [59]. As the operation range of these sensors is rather limited (like in the case of fiber optic SPR sensor), various possibilities of tuning the operation range of the sensors have been explored. It covers using waveguides fabricated in a low refractive index glass [62], waveguides with a buffer layer [63], waveguides with a high refractive index overlayer [64] and waveguides with even more complex multilayer structures [65]. However, all these approaches comprise incorporation of additional layers which leads to reduction of the SPR sensitivity because of relatively lower concentration of the electromagnetic field in the analyzed medium.
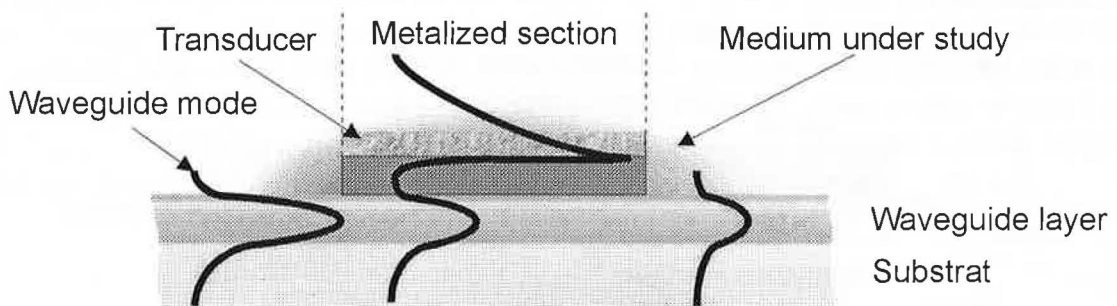

Fig. 1.2.5 Waveguide-based SPR sensor sensing element.

Nowadays, optical fiber SPR sensors represent the highest level of miniaturization of SPR sensing devices allowing for chemical and biological sensing in inaccessible locations, where their mechanical flexibility and ability to transmit optical signals over long distances make the use of optical fibers very attractive. The use of optical fibers for SPR sensing has been first proposed by Jorgenson and Yee [37]. They used wavelength interrogation technique and formed an SPR sensing structure by using a conventional polymer clad silica (PCS) mutlimode fiber with partly removed cladding and an SPR active metal film deposited symmetrically around the exposed section of the fiber core. This approach allows constructing miniaturized optical fiber SPR probes with a limited interaction area whose length was about 10 mm. The interaction region could be in the

11

middle of the fiber or at the fiber tip (Fig. 1.2.6). The geometry with the interaction region at the fiber tip is more advantageous because only a single fiber is used for delivering the light to and from the sensor active region. This sensor is capable of measuring refractive index in the range of 1.2-1.4 with the resolution of up to 5×10^{-5} RIU assuming the resonant wavelength resolution of 0.5 nm. A similar, but intensity-based fiber optic sensor with the interaction region in the middle of the fiber was also reported [44], Fig. 1.2.7. In this configuration collimated monochromatic light is launched into a straight fiber in such a way that only modes with propagation constants within a narrow range are efficiently excited. Variations in the refractive index of analyte are determined by measuring the transmitted optical power. The refractive index resolution of 8×10^{-5} RIU was reported [44] using a system with amplitude resolution of 0.2 percent. The sensitivity of this SPR sensor is negatively influenced by exciting the SPW by fiber modes incident on the metal surface at slightly different angles. This approach is very similar to that of the light pipe described above. Generally, the both types of multimode fiber optic SPR sensing devices may suffer from rather low stability and thus also low resolution. The modal distribution of light in the fiber is very sensitive to mechanical disturbances, which may cause intermodal coupling and modal noise. Because of the cylindrical shape of the sensing area, the fabrication of homogenous SPR coatings (metal films and transducers) makes the device technologically complicated.
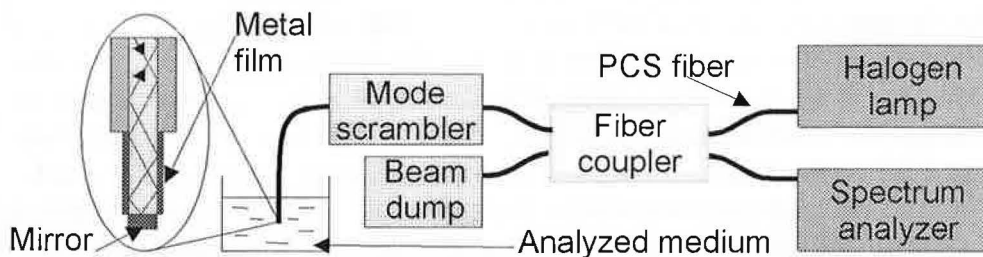

Fig. 1.2.6 Multimode fiber-based SPR sensor configuration with wavelength interrogation [37].
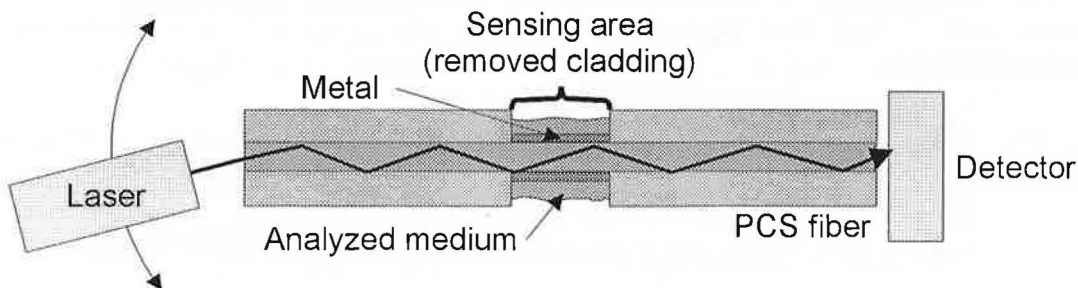

Fig. 1.2.7 Multimode fiber-based SPR sensor configuration with amplitude interrogation [44].

In order to overcome these drawbacks and to allow further reduction of the size of the sensing area, SPR sensors based on single-mode optical fibers have been proposed. Two approaches were suggested [66,67,68]. The use of a tapered [66] single-mode fiber is a well-known technique in sensing. In the tapered region the light is coupled into cladding modes. In this region the fiber behaves in the same way as the decladed multimode fiber in Fig. 1.2.6. In [66] (Fig. 1.2.8), a silver film was deposited in one plane resulting in variation of its thickness around the tapered fiber. This makes the evaporation process easy, but results in broadening of the SPR dip as the SPR condition slightly depends on

12

the metal film thickness. The reported sensitivity and resolution are rather low compared to the multimode fiber-based configurations being of about 60 dB/RIU and 5×10^{-4} RIU, respectively, in fixed wavelength amplitude-based interrogation, Fig. 1.2.8. The sensor is set to operate in aqueous environment by a proper choice of the operating wavelength in the visible region of spectrum. Operation of the sensor with a thermal source, which emits non-polarized broadband light, makes the device insensitive to polarization dependent interaction with the SPW. The polarization sensitivity is expected to be high, as the sensing region is not circularly symmetric due to the planar deposition of the metal film. The drawback is that the coupling efficiency of light emitted by the thermal source into a single-mode fiber is very poor (typically in the order of tens of pW) and more sophisticated (e.g., lock in) detection techniques have to be used.
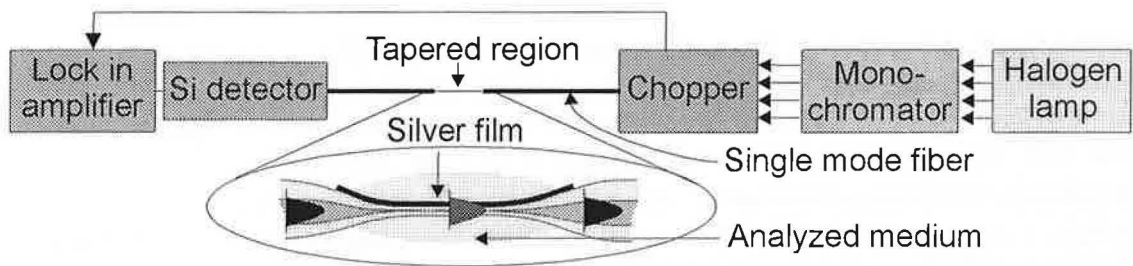

Fig. 1.2.8 Amplitude-based detection scheme using a single-mode tapered fiber [66].

Another method [67,68] uses a side-polished single-mode fiber (Fig. 1.2.9), which is well known from the production of fiber polarizers and tunable couplers. The cladding of the single-mode fiber is locally removed to get access to the evanescent field of the guided mode and this area is covered with a thin metal film. In the previously published work [10], the response of the sensor element was detected by monitoring the output power changes at a fixed wavelength (amplitude mode), Fig. 1.2.10. Because the SPR manifests itself by a more than 50 dB decrease in the power of the guided mode in a very narrow range of refractive indices of analyzed medium, this approach leads to the sensitivity better than 2500 dB/RIU, which was the experimentally achieved value in [10]. It results in a resolution of 3×10^{-6} RIU using the optoelectronic system assumed in Table 1.2.1. As follows from Table 1.2.1, this value is comparable with the bulk optics-based configurations.
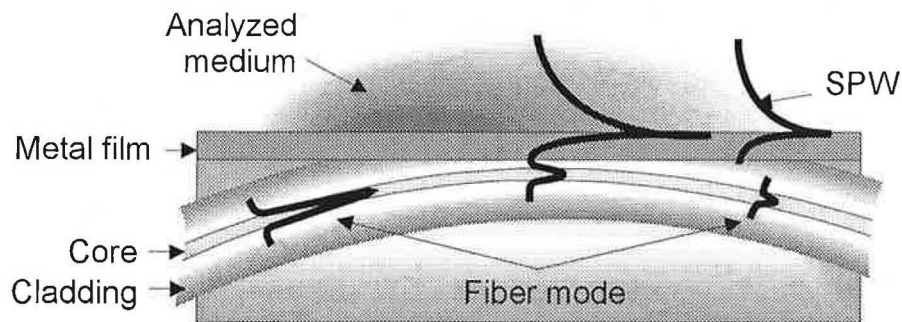

Fig. 1.2.9 SPR sensor element structure based on the side-polished single-mode fiber.

This approach overcomes all the drawbacks of the multimode fiber SPR sensors. Moreover, the sensing area is further miniaturized (its size is only 2×0.01 mm^2).

However, the planar metal film allows excitation of the SPW only by one polarization of the fiber mode (due to inherent TM character of the SPW). As the polarization of the fiber mode changes due to fiber deformations (bending and twisting), this represents a serious challenge in development of SPR sensors based on a side-polished single-mode fiber. It may be overcome by employing *polarization maintaining* (**PM**) fibers or by using a non-polarized light.

The advantage brought by PM fibers is the possibility of using a simple, high-resolution amplitude-based detection scheme, where a semiconductor laser source and a silicon photodiode detector can be utilized (Fig. 1.2.10). The drawbacks are the high price of PM fibers, the need of precise orientation of the PM fiber before side-polishing, and limited mechanical stability of PM fibers, which may cause problems during the side-polishing.

The use of non-polarized light allows the employment of a conventional fiber. The presence of TE polarized light in the optode, however, shallows the SPR dip significantly – as the TE polarized part of the guided mode carries one half of its power, the SPR dip cannot be, in principle, deeper than 3 dB. As a consequence, the simple amplitude detection scheme (Fig. 1.2.10) results in a device with drastically reduced amplitude sensitivity. On the other hand, the high sensitivity in the spectral domain is retained, which suggests utilizing the wavelength interrogation with a spectrally broadband source and a spectrum analyzer as a detector. Though, there are several challenges, which have to be overcome. Light sources capable of launching enough light into a single-mode fiber are usually narrow-band and, moreover, partially polarized. Another problem is that the SPR optode produces partially polarized light (it absorbs only TM polarized light), which cannot be reliably analyzed by a spectrum analyzer, as standard spectrum analyzers are input polarization dependent.
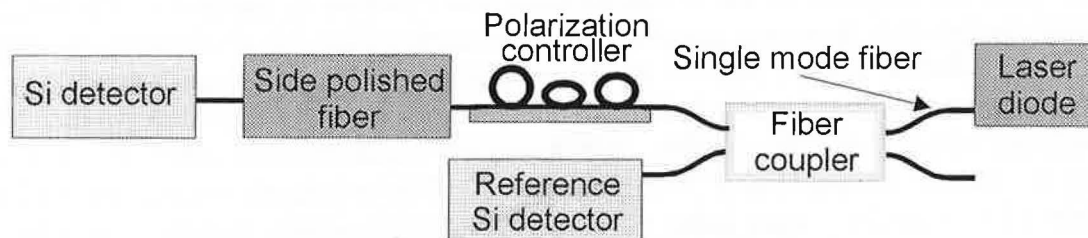

Fig. 1.2.10 Amplitude-based detection scheme using a single-mode side-polished fiber [10].

2. Research Goals

The aim of this thesis is to develop a remote intrinsic fiber optic biosensor based on resonant excitation of SPW in a thin gold film by light guided in a standard single-mode optical fiber. To construct the sensor system I chose spectral interrogation of a surface plasma wave with a non-polarized light. This configuration promises high sensitivity and resolution together with resistance to bending and twisting of the sensor element input and output fibers. This thesis consists of the design, realization and testing of the biosensor and is focused on the following issues.

- Particular attention is given to theoretical analysis of the sensor element by rigorous bi-directional beam expansion and propagation method (BEM), Chapter 3.3.

- Optimization of the sensing element design in terms of parameters such as residual amount of the fiber cladding, thickness of the gold film supporting SPW and thickness of the tantalum pentoxide tuning overlayer, Chapter 3.4.

- On the basis of the theoretical analysis the sensor element samples with optimized parameters are prepared. The samples are studied experimentally in order to evaluate sensor element parameters, Chapter 4.2.

- Parasitic polarization sensitivity of the available sources and detectors is overcome by employing a Lyot depolarizer and a fiber mode mixer, Chapter 4.3.

- The whole sensor system is analyzed and its limitations are determined, Chapter 4.3.

- The sensor system is built and its sensitivity and resolution are evaluated by performing simple refractometric measurement, Chapter 4.4.

- The potential of the sensor system for biosensing is demonstrated in model immunosensing experiment, Chapter 4.4.

3. Theoretical Analysis of the Sensor Element

As the designed SPR sensing element is based on a standard single-mode optical fiber, the theoretical analysis is based on electromagnetic theory of optical fibers.

3.1 Single-Mode Fibers

A standard single-mode fiber has circular symmetry of its cross-section, so that electric and magnetic vector fields, $\vec{E}$ and $\vec{H}$, of the fiber modes can be expressed as:

$$\vec{E}(r,\theta,z) = \vec{e}(r,\theta) \cdot \exp(-i\beta z), \qquad (.1.1)$$

$$\vec{H}(r,\theta,z) = \vec{h}(r,\theta) \cdot \exp(-i\beta z), \qquad (3.1.2)$$

where β is the modal propagation constant, r and θ are polar coordinates on the fiber cross section, and z is the distance along the axis of the fiber as shown in Fig. 3.1.1.
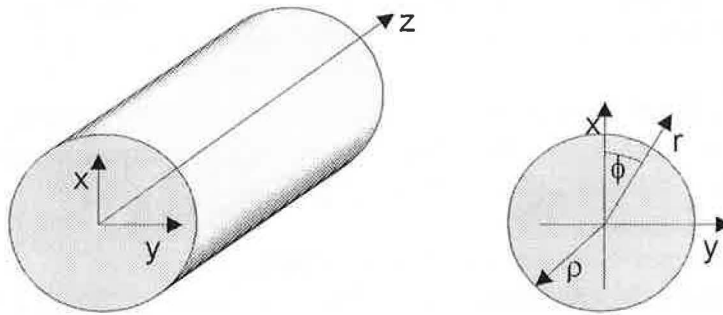

Fig. 3.1.1 Optical fiber of circular cross section.

In general, $\vec{E}$ and $\vec{H}$ can be found by solving Maxwell's equations. However, because standard single-mode fibers are *weakly guiding* (they have refractive index profile *n(r)* with a very small difference between the maximum and minimum values of *n(r)* - typically less than 1 percent), it turns out that $\vec{E}$ and $\vec{H}$ are approximate solutions of the scalar wave equation. Simply, the propagation constant β of the fundamental mode has to lie somewhere between two extremes given by the value of β for a *z*-directed plane wave propagating in an infinite medium of refractive index equal to the maximum (n_{c0}) and minimum (n_{c1}) values of *n(r)* [69]. Then β is bound by:

$$2\pi n_{c1}/\lambda < \beta < 2\pi n_{c0}/\lambda, \qquad (3.1.3)$$

where λ is the wavelength in vacuum. Due to weak guiding, $n_{c0} \cong n_{c1}$ and $\beta \cong 2\pi n/\lambda$, which is the propagation constant of a *z*-directed plane wave in an unbounded medium of refractive index $n_{c1} < n < n_{c0}$.

Accordingly, the fundamental mode of an optical fiber has to be nearly a transverse electromagnetic (TEM) wave the polarization state of which may be expressed by using two orthogonal polarization states. Therefore a *single*-mode fiber guides *two* modes with orthogonal polarizations. In an ideal fiber, these polarization modes are degenerate with identical propagation constants and group phase velocities and therefore the polarization of the light propagating through such a fiber is preserved. However, in real fibers there are slight imperfections that break the circular symmetry and lift this degeneracy so that the modes propagate at different phase velocities, which leads to a change in the polarization state of the light propagating in the fiber. Further, randomly distributed thermally and mechanically introduced stresses act on the fiber and cause

16

cross talk between the two polarization modes (through elasto-optic and thermo-optic effects), which further changes the original input polarization state [70]. For example, bending the fiber in the y-z plane induces through the elasto-optic effect changes in the refractive index along the y-axis. This causes birefringence, which usually changes the polarization state of the guided mode like a zero-order wave plate [70].

3.2   Element Structure and Principle of Operation

The proposed sensor element is based on a standard single-mode optical fiber. Its cladding is locally removed to get access to the evanescent field of the guided mode and this area is covered with a thin gold film, a tantalum pentoxide tuning overlayer, a chemo-optical transducer, and a medium under study. The guided mode propagates in the fiber and excites SPW at the outer interface of the gold film in case the two modes are closely phase-matched (Fig. 3.2.1). The propagation constant of SPW depends dramatically on the spatial profile of refractive index of the structure adjacent to the tantalum pentoxide overlayer (analyzed medium). Therefore changes in the spatial profile of the refractive index of the analyzed medium cause mismatch of the two modes. As SPW is highly lossy, the mismatch results in changes of the fiber mode attenuation. Consequently, variations in the spatial profile of refractive index of the analyzed medium can be sensitively detected by monitoring changes in the output power at a fixed wavelength (amplitude mode) or by monitoring changes in the wavelength at which the resonant attenuation of the fiber mode occurs (spectral mode). Since the SPW is inherently TM polarized wave, only the fiber mode of the corresponding polarization state may be involved in the interaction, while the mode with the orthogonal polarization state is attenuated only due to ohmic loss in the metal layer.
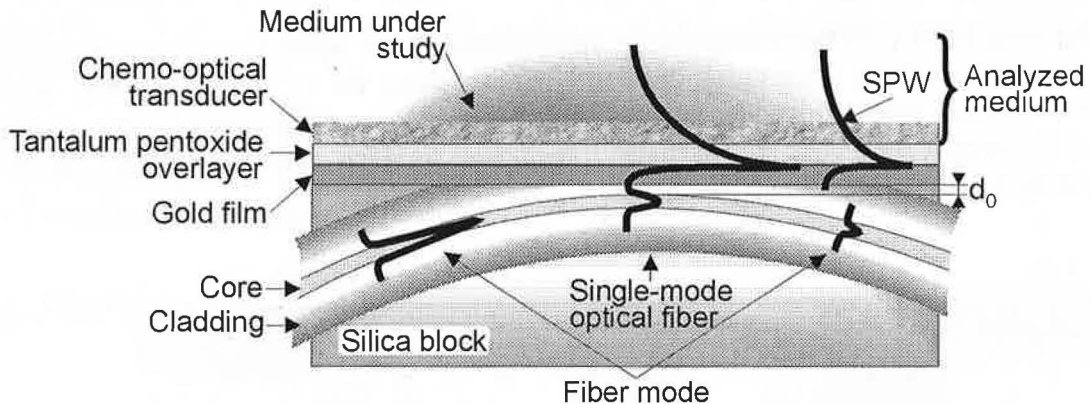

Fig. 3.2.1 SPR single-mode optical fiber sensor element structure.

3.3   Beam Expansion and Propagation Method

We intend to calculate how a light wave propagates through the sensor element with a defined refractive index distribution. A rigorous analysis of the sensor element structure is difficult due to its low symmetry and the presence of a very lossy metal film. On the other hand, we are interested only in the steady state, in which a steady-state input field excites the fields inside the structure. This situation can be simulated numerically and the analysis can be performed by *Beam Propagation Methods* (**BPM**). Assuming a wave is propagating in the longitudinal +z direction of the element and assuming the steady-state field distribution is known in the cross-section plane A ($z=z_k$), the task is to

determine the stationary field at the plane B ($z=z_k+\Delta z=z_{k+1}$). Repeating this calculation stepwise from the input to the output, the whole device can be approximately analyzed.

There are several BPM algorithms based on different approaches leading to various restrictions (FFT (fast Fourier transform) BPM [71], FD (finite difference) BPM [72], FE (finite elements) BPM [73], MoL (methods of lines) BPM [74], BEM (bi-directional mode expansion propagation method [75]), etc.).

For our purpose, the BEM is the most suitable. It allows analysis of structures with steep layer boundaries, i.e. including very thin (tens of nm) films [75], which is the case of a metal film supporting SPW. To follow the approach from [75], the fiber has to be approximated with a planar structure first.

As the replacement of an optical fiber with a planar waveguide is a rather rough approximation, there is no known general way to determine parameters of the equivalent planar waveguide. We will use an approach described in [76], which was developed for modeling the behavior of SPR polarizers based of the side-polished fiber, which is a structure very similar to ours. As coupling of the fiber guided mode with SPW through the evanescent field is important, the amount of energy carried in the evanescent field of the fiber is of interest. It should be identical with that of the equivalent planar waveguide. We would also like to have the same space-time evolution of the mode in the fiber and in the planar waveguide, so their effective refractive indices have to be equal. Having known the fiber refractive profile, applying the above conditions and using similar calculations as in [76], we obtain parameters of the equivalent step-index planar waveguide, i. e. refractive index of the guiding layer and its thickness.

In the used BEM [75] the waveguide is approximated by a layered structure shown in Fig. 3.3.1. The whole structure is divided laterally (along the z direction) so that each section can be approximated with a laterally homogeneous. The optical wave at the input is partially reflected and partially transmitted on each lateral boundary. At the output there is only the transmitted wave.
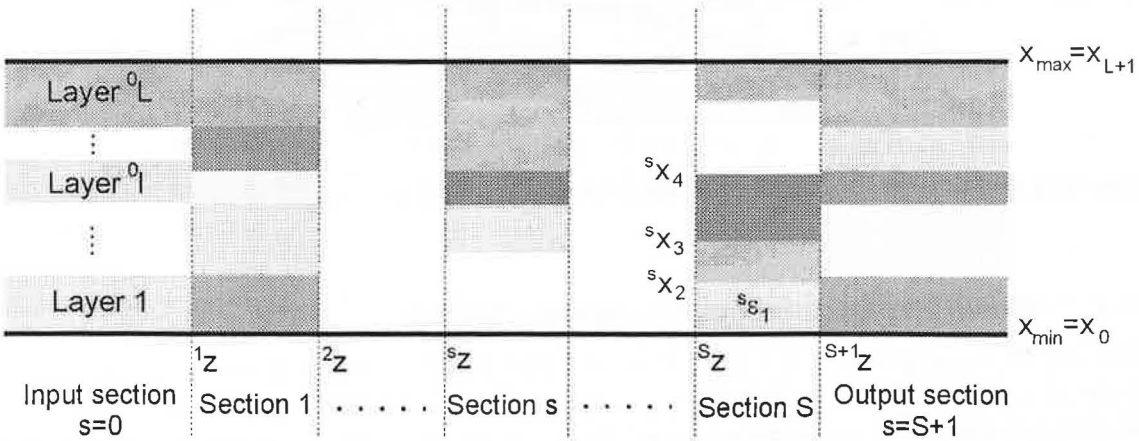

Fig. 3.3.1 Layered structure for BEM.

The structure consists of S lateral sections of finite length, and of input and output semi-infinite sections. Every section consists of a finite number (L) of homogeneous layers

18

and the *l*-th layer in the *s*-th section is denoted as $^s l$ and its permittivity as $^s \varepsilon_l$. The lateral coordinate of the *s*-th section's front face is $^s z$ and the *(l+1)/l*-th layer interface is at $^s x_l$.

At all boundaries the normal field components have to be equal, so that:

$$({}^s \vec{E} - {}^{s\pm1} \vec{E})_\perp = 0 \text{ and } ({}^s \vec{H} - {}^{s\pm1} \vec{H})_\perp = 0. \qquad (3.3.1)$$

We decompose the field in every section into eigenmodes which propagate in both directions, so that the field can be described by complex amplitudes of the modes. The conditions (3.3.1) give relationships among the amplitudes at the boundaries, which enables us to calculate the mode amplitudes in every section.

The spectrum of eigenmodes of an open structure is complex because of a continuous spectrum of radiation modes. To avoid this difficulty, we enclose our structure in the direction of the normal into an interval $\langle x_0, x_{L+1} \rangle$ (see Fig. 3.3.1) by hypothetical electric and magnetic 'ideally conducting' walls for TE and TM polarized modes, respectively. This makes the spectrum discrete.

Basic Relations

Electromagnetic waves obey Maxwell's equations. For monochromatic waves in a linear, non-magnetic dielectrics without sources the equations can be in complex representation with the time-dependence $\exp(-i\omega t)$ written as:

$$\nabla \times \vec{E}(\vec{r}) = i\omega\mu_0 \vec{H}(\vec{r}), \qquad \nabla \times \vec{H}(\vec{r}) = -i\omega\varepsilon_0 \varepsilon \vec{E}(\vec{r}), \qquad (3.3.2)$$
$$\nabla \cdot [\varepsilon(\vec{r})\vec{E}(\vec{r})] = 0, \qquad \nabla \cdot \vec{H}(\vec{r}) = 0.$$

Each section in Fig. 3.3.1 is a planar waveguide in which the field can be decomposed into TE (with the components E_y, H_x, and H_z) and TM modes (with the components H_y, E_x, and E_z).

In every section of the waveguide (Fig. 3.3.1), the field component E_y for the TE polarization and the field component H_y for the TM polarization can be decomposed into eigenmodes propagating in the $+z$ and $-z$ directions:

$$\varphi(x, z) = \sum_m \varphi^m(x)(f_m^+(z) + f_m^-(z)), \qquad (3.3.3)$$

$$\varphi(x, z) = \begin{cases} E_y(x, z) \\ H_y(x, z) \end{cases}, \quad \varphi^m(x) = \begin{cases} E_y^m(x) & \text{TE modes,} \\ H_y^m(x) & \text{TM modes,} \end{cases}$$

where:

$$f_m^\pm(z) = C_m^\pm \exp(\mp i\beta_m z), \qquad (3.3.4)$$

where *m* is the mode index, β_m is the propagation constant, and C_m the complex amplitude of the mode. The $\varphi^m(x)$ is a solution of the wave equation derived from Maxwell's equations (3.3.2):

$$\frac{d^2 \varphi^m(x)}{dx^2} + (k_0^2 \varepsilon(x) - \beta_m^2)\varphi^m(x) = 0. \qquad (3.3.5)$$

The other field components can be derived from Maxwell's equations as follows:

19

$$\text{TE:} \qquad H_x^m(x) = -\sqrt{\frac{\varepsilon_0}{\mu_0}} \frac{\beta^m}{k_0} \varphi^m(x), \qquad H_z^m(x) = -\frac{i}{k_0} \sqrt{\frac{\varepsilon_0}{\mu_0}} \frac{\partial \varphi^m(x)}{\partial x}, \qquad (3.3.6)$$

$$\text{TM:} \qquad E_x^m(x) = +\sqrt{\frac{\mu_0}{\varepsilon_0}} \frac{k_z^m}{k_0 \varepsilon(x)} \varphi^m(x), \qquad E_z^m(x) = -\frac{i}{k_0} \sqrt{\frac{\mu_0}{\varepsilon_0}} \frac{\partial \varphi^m(x)}{\partial x}.$$

If the structure is surrounded by ideally electric conducting walls for the TE modes and by ideally magnetic conducting walls for the TM modes (they are placed at the x_{min}, x_{max} positions), the field at these walls is zero, which gives us boundary conditions:

$$\varphi^m(x_{\min}) = \varphi^m(x_{\max}) = 0. \qquad (3.3.7)$$

Complex Mode Solver for Multilayer Waveguide

For calculation of the eigenmodes in every section, the transfer matrix method [77] with small modifications is used. This method allows us to solve (3.3.5) for a step-index structure with boundary conditions (3.3.7) at the ideally conducting electric and magnetic walls.

Let us consider a single layer. To calculate the field in the point $(x + \Delta x)$ having known it in another point (x), we have to know not only $\varphi(x)$, but also the derivation $d\varphi(x)/dx$, as can be seen from the solution of (3.3.5) inside one layer:

$$\begin{pmatrix} \varphi(x) \\ d\varphi(x)/dx \end{pmatrix} = \begin{pmatrix} \cos(\gamma \Delta x) & \dfrac{\varepsilon^v}{\gamma} \sin(\gamma \Delta x) \\ -\dfrac{\varepsilon^v}{\gamma} \sin(\gamma \Delta x) & \cos(\gamma \Delta x) \end{pmatrix} \begin{pmatrix} \varphi(x + \Delta x) \\ d\varphi(x + \Delta x)/dx \end{pmatrix}, \qquad (3.3.8)$$

$$\begin{pmatrix} \varphi(x + \Delta x) \\ d\varphi(x + \Delta x)/dx \end{pmatrix} = \begin{pmatrix} \cos(\gamma \Delta x) & -\dfrac{\varepsilon^v}{\gamma} \sin(\gamma \Delta x) \\ \dfrac{\varepsilon^v}{\gamma} \sin(\gamma \Delta x) & \cos(\gamma \Delta x) \end{pmatrix} \begin{pmatrix} \varphi(x) \\ d\varphi(x)/dx \end{pmatrix},$$

where $\gamma = \sqrt{\varepsilon - N^2}$ is the transverse propagation constant and N is the effective refractive index ($N = \beta k_0$). From (3.3.6) we see that the derivative $d\varphi(x)/dx$ corresponds to the z-component of the field, which together with the field y-component described by $\varphi(x)$ represents field components parallel to an interface among the layers, which values have to be conserved going through the interface. Thus, we can assign a transfer matrix to every layer:

$$M_l^{\pm} = \begin{pmatrix} \cos(\gamma(x_{l+1} - x_l)) & \pm \dfrac{\varepsilon^v}{\gamma} \sin(\gamma(x_{l+1} - x_l)) \\ \mp \dfrac{\varepsilon^v}{\gamma} \sin(\gamma(x_{l+1} - x_l)) & \cos(\gamma(x_{l+1} - x_l)) \end{pmatrix}, \qquad (3.3.9)$$

which transforms the field passing through the l-th layer 'up' or 'down':

$$\begin{pmatrix} \varphi(x_{l+1}) \\ d\varphi(x_{l+1})/dx \end{pmatrix} = M_l^+ \begin{pmatrix} \varphi(x_l) \\ d\varphi(x_l)/dx \end{pmatrix}, \qquad \begin{pmatrix} \varphi(x_l) \\ d\varphi(x_l)/dx \end{pmatrix} = M_l^- \begin{pmatrix} \varphi(x_{l+1}) \\ d\varphi(x_{l+1})/dx \end{pmatrix}, \qquad (3.3.10)$$

where x_l are the coordinates of the layer interfaces.

Numerically well-behaving formulation of the dispersion equation can be obtained by calculation the field amplitudes in an r-th layer starting from the both walls. For example, to calculate the filed amplitudes at the upper r-th layer interface, (3.3.9) is used starting from the upper wall. The condition of matching the field components calculated from both sides at the upper side of r-th layer can thus be, using border conditions (3.3.7), written in the form:

$$\begin{pmatrix} \varphi(x_r) \\ d\varphi(x_r)/dx \end{pmatrix} = M^+ \begin{pmatrix} 0 \\ d\varphi(x_{min})/dx \end{pmatrix}, \qquad \begin{pmatrix} \varphi(x_r) \\ d\varphi(x_r)/dx \end{pmatrix} = M^- \begin{pmatrix} 0 \\ d\varphi(x_{max})/dx \end{pmatrix}, \qquad (3.3.11)$$

where:

$$M^+ = \prod_{l=1}^{r} M_l^+, \qquad M^- = \prod_{l=r}^{L} M_l^-. \qquad (3.3.12)$$

From (3.3.11) we obtain the dispersion equation in the form:

$$M_{12}^+(N) \cdot M_{22}^-(N) - M_{22}^+(N) \cdot M_{12}^-(N) = 0. \qquad (3.3.13)$$

The proper choice of r contributes to numerical stability of the solutions. It may be chosen to advantage at the position where the mode fields are expected to be rather strong.

It is well known that the (properly formulated) dispersion equation of a closed multilayer waveguide is an analytic function of a complex variable N^2. To find roots of dispersion equation (3.3.13) a simple algorithm derived from the solution of lossless waveguides is used: in the first step the equation as well as N^2 are set to be real and N^2 may be found by an extremely simple interval halving procedure. The presence of a metal layer in the waveguide structure does not cause problems because it is known that the surface plasma wave solutions exist also for a zero imaginary part of the metal permittivity. The only difference is that the interval in which the solution has to be sought has to be increasingly extended over the maximum value of the permittivity of the waveguide increasingly, as the metal layer becomes thinner and thinner. After the solutions of the lossless case are known, the imaginary parts of the permittivities are gradually increased, and the zeros are traced into the complex plane using the Newton method; the regularity of the dispersion function is thus utilized to advantage.

BEM

Boundary conditions between the sections require the continuity of tangential components of electric and magnetic fields at the interface z_s:

$$^{s+1}\varphi(x,z)\big|_{z=z_s} = {}^s\varphi(x,z)\big|_{z=z_s} \qquad (3.3.14)$$

and

$$\frac{1}{^s\varepsilon^v(x)} \frac{\partial}{\partial z} {}^{s+1}\varphi(x,z)\bigg|_{z=z_s} = \frac{1}{^s\varepsilon^v(x)} \frac{\partial}{\partial z} {}^s\varphi(x,z)\bigg|_{z=z_s}, \qquad (3.3.15)$$

where $v=0,1$ for TE and TM modes, respectively. Using (3.3.3) and (3.3.4), (3.3.14) and (3.3.15) can be rewritten as:

$$^{s+1}\hat{\Theta}(x)\cdot{}^{s+1}\hat{P}(z_s)\cdot\begin{pmatrix} ^{s+1}C^+(z_s) \\ ^{s+1}C^-(z_s) \end{pmatrix} = {}^s\hat{\Theta}(x)\cdot{}^s\hat{P}(z_s)\cdot\begin{pmatrix} ^sC^+(z_s) \\ ^sC^-(z_s) \end{pmatrix}, \qquad (3.3.16)$$

with the 2M×2 matrix $^s\hat{\Theta}(x)$:

$$
^s\hat{\Theta}(x) = \begin{pmatrix} ^s\varphi_1(x) & \cdots & ^s\varphi_M(x) & 0 & \cdots & 0 \\ 0 & \cdots & 0 & \dfrac{^s\varphi_1(x)}{^s\varepsilon^v(x)} & \cdots & \dfrac{^s\varphi_M(x)}{^s\varepsilon^v(x)} \end{pmatrix},
$$

(3.3.17)

the propagation 2M×2M matrix $^s\hat{P}(z)$:

$$
^s\hat{P}(z) = \begin{pmatrix}
e^{-i\,^s\beta^1(z-z_{s-1})} & 0\ldots 0 & 0 & e^{i\,^s\beta^1(z-z_{s-1})} & 0\ldots 0 & 0 \\
0 & & \vdots & 0 & & \vdots \\
\vdots & & 0 & \vdots & & 0 \\
0 & 0\ldots 0 & e^{-i\,^s\beta^M(z-z_{s-1})} & 0 & 0\ldots 0 & e^{i\,^s\beta^M(z-z_{s-1})} \\
i\,^s\beta^1 e^{-i\,^s\beta^1(z-z_{s-1})} & 0\ldots 0 & 0 & -i\,^s\beta^1 e^{i\,^s\beta^1(z-z_{s-1})} & 0\ldots 0 & 0 \\
0 & & \vdots & 0 & & \vdots \\
\vdots & & 0 & \vdots & & 0 \\
0 & 0\ldots 0 & i\,^s\beta^M e^{-i\,^s\beta^M(z-z_{s-1})} & 0 & 0\ldots 0 & -i\,^s\beta^M e^{i\,^s\beta^M(z-z_{s-1})}
\end{pmatrix}
$$

(3.3.18)

and the 2M vector $\left(^sC^\pm\right)_m = {}^sC_m^\pm$ for $m=1, ..\, M$. There is an inherent numerical problem in the formulation of the matrix $^s\hat{P}(z)$. Namely, for complex $^s\beta$ and large $(z-z_{s-1})$, some of the matrix elements for higher order modes become rather large, which will be discussed later.

Formulating the orthogonality of the local eigenfunctions $^s\varphi_m(x)$ as:

$$
\int_{x_{\min}}^{x_{\max}} \frac{^s\varphi_n(x)\cdot{}^s\varphi_m(x)}{^s\varepsilon^v(x)} dx = \delta_{mn},
$$

(3.3.19)

the system of equations (3.3.15) can be resolved by using the transposed matrix $^s\hat{\Theta}^T(x)$, for which it holds:

$$
\int_{x_{\min}}^{x_{\max}} {}^s\hat{\Theta}(x)\cdot{}^s\hat{\Theta}^T(x)dx = \hat{I},
$$

(3.3.20)

because of the completeness of the set of eigenfunctions $^s\varphi_m(x)$; here $\hat{I}$ is the unity matrix of rank M. Multiplying both sides of (3.3.16) by $^s\hat{\Theta}^T(x)$, integrating over the entire x-range and then multiplying by $^s\hat{P}^{-1}(z)$, we obtain the solution in the form:

$$
^{s+1}\vec{C} = {}^{s+1,l}\hat{T}\cdot{}^s\vec{C}, \qquad ^{s+1,s}\hat{T} = {}^{s+1}\hat{P}^{-1}(z_s)\cdot{}^{s+1,s}\hat{O}\cdot{}^s\hat{P}(z_s).
$$

(3.3.21)

In this expression the matrix $^{s+1,s}\hat{O}(x)$ consists of two different overlap integrals of the eigenfunctions, which represent the coefficients of the expansion of the field in terms of the eigenfunctions in either interfaces:

$$
{}^{s+1,s}\hat{O} = \int_{x_{\min}}^{x_{\max}} {}^{s+1}\hat{\Theta}^T(x) \cdot {}^{s}\hat{\Theta}(x)dx = \begin{pmatrix} {}^{s,s+1}O_{1,1} & \cdots & {}^{s,s+1}O_{1,M} & & & & \\ \vdots & \ddots & \vdots & & 0 & & \\ {}^{s,s+1}O_{M,1} & \cdots & {}^{s,s+1}O_{M,M} & & & & \\ & & & {}^{s+1,s}O_{1,1} & \cdots & {}^{s+1,s}O_{1,M} \\ & 0 & & \vdots & \ddots & \vdots \\ & & & {}^{s+1,s}O_{M,1} & \cdots & {}^{s+1,s}O_{M,M} \end{pmatrix}.
$$

(3.3.22)

The forward propagation, $s \to s+1$:

$$
{}^{s,s+1}O_{m,n} = \int_{x_{\min}}^{x_{\max}} \frac{{}^{s}\varphi_m(x) \cdot {}^{s+1}\varphi_n(x)}{{}^{s+1}\varepsilon^v(x)}dx,
$$

(3.3.23)

and backward propagation, $s+1 \to s$:

$$
{}^{s+1,s}O_{m,n} = \int_{x_{\min}}^{x_{\max}} \frac{{}^{s+1}\varphi_m(x) \cdot {}^{s}\varphi_n(x)}{{}^{s}\varepsilon^v(x)}dx,
$$

(3.3.24)

for $m,n = 1, \dots M$. For every s the functions ${}^{s}\varphi_m$ are the solutions of the dispersion equation in the layered step-index waveguide (3.3.13). As ${}^{s}\hat{P}(z)$ is a sparse tri-diagonal matrix, the matrix inversion and multiplication forming ${}^{s+1,s}\hat{T}$ can be worked out analytically. The 2M×2M elements of the transfer matrix ${}^{s+1,s}\hat{T}$ are then:

$$
{}^{s+1,s}\hat{T} = \frac{1}{2}\begin{pmatrix} & \vdots & & & \vdots & \\ \cdots & \left({}^{s,s+1}O_{mi}+{}^{s+1,s}O_{mi}\dfrac{{}^{s}\beta^i}{{}^{s+1}\beta^m}\right)e^{-i\,{}^{s}\beta^i d_s} & \cdots & \left({}^{s,s+1}O_{mi}-{}^{s+1,s}O_{mi}\dfrac{{}^{s}\beta^i}{{}^{s+1}\beta^m}\right)e^{+i\,{}^{s}\beta^i d_s} & \cdots \\ & \vdots & & & \vdots & \\ \cdots & \left({}^{s,s+1}O_{mi}-{}^{s+1,s}O_{mi}\dfrac{{}^{s}\beta^i}{{}^{s+1}\beta^m}\right)e^{-i\,{}^{s}\beta^i d_s} & \cdots & \left({}^{s,s+1}O_{mi}+{}^{s+1,s}O_{mi}\dfrac{{}^{s}\beta^i}{{}^{s+1}\beta^m}\right)e^{i\,{}^{s}\beta^i d_s} & \cdots \\ & \vdots & & & \vdots & \end{pmatrix}.
$$

(3.3.25)

Finally, the product of all ${}^{s+1,s}\hat{T}$'s describes the wave transmission through the whole structure:

$$
\hat{T}_{sys} = \prod_{s=1}^{S-1} {}^{s+1,s}\hat{T},
$$

(3.3.26)

so that:

$$
{}^{S}\vec{C} = \hat{T}_{sys} \cdot {}^{1}\vec{C},.
$$

(3.3.27)

The calculation of (3.3.26) may cause numerical problems (some of the matrix elements become rather large) particularly with nearly laterally symmetric (large $x_{l+1}-x_l$) lossy (large imaginary part of ${}^{s}\beta^m$) structures. This difficulty can be overcome by using another method for mode-solving [78] instead of the transfer matrix method or by calculating only forward traveling modes neglecting multiple reflections. We have chosen the second approach. Then, (3.3.25) simplifies to:

23

$$^{s+1,s}\hat{T} = \frac{1}{2}\begin{pmatrix} & & \vdots & & & \vdots & \\ \cdots & \left(^{s,s+1}O_{mi} + {}^{s+1,s}O_{mi}\dfrac{^s\beta^i}{^{s+1}\beta^m}\right)e^{-i\,^s\beta^i d_s} & \cdots & 0 & \cdots \\ & & \vdots & & & \vdots & \\ \cdots & \left(^{s,s+1}O_{mi} - {}^{s+1,s}O_{mi}\dfrac{^s\beta^i}{^{s+1}\beta^m}\right)e^{-i\,^s\beta^i d_s} & \cdots & 0 & \cdots \\ & & \vdots & & & \vdots & \end{pmatrix}. \tag{3.3.28}$$

Supposing the structure is excited only by a single guided mode at the input:

$$^1\vec{C} = \left(^{in}C,\ 0\ \dots\ 0\right), \tag{3.3.29}$$

and that only this mode propagates at the output of the waveguide:

$$^s\vec{C} = \left(^{out}C,\ 0\ \dots\ 0\right). \tag{3.3.30}$$

From (3.3.27) and (3.3.30) then follows:

$$^{out}C = \left(\hat{T}_{sys}\right)_{11}{}^{in}C, \tag{3.3.31}$$

where $\hat{T}_{sys}$ is given by (3.3.28) and (3.3.26).

3.4 Results

The BEM method together with the mode solver described in previous sections was programmed in the FORTRAN language at IREE AS CR by Dr. Jiří Čtyroký according to [75,77]. The curved, side-polished single-mode fiber in the planar waveguide approximation was divided into 21 laterally homogenous regions for performing BEM. The resulted structure is depicted in Fig. 3.4.1.
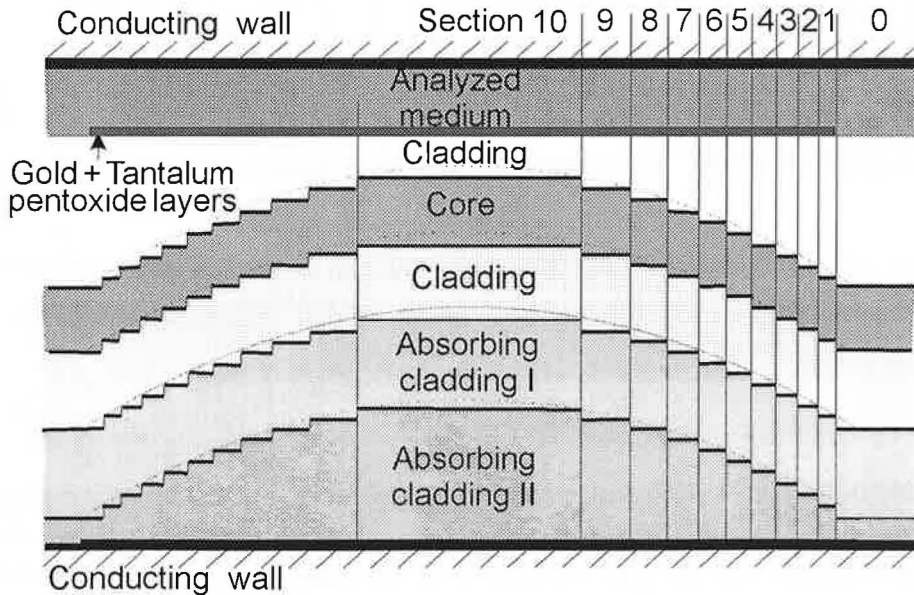

Fig. 3.4.1 Structure for BEM analysis.

Several parameters can be controlled in the process of sensor element preparation. These are:

- The amount of residual fiber cladding after side-polishing. It is characterized by the minimum distance d_0 between the fiber core and the polished fiber cladding surface.

- The thickness of the gold film supporting SPW.

- The thickness of the tantalum pentoxide tuning overlayer.

The theoretical analysis should result in determination of these parameters in order to achieve maximum sensor sensitivity and resolution. The sensitivity is given by a change in the spectral position of the SPR dip induced by a change in the spatial profile of the refractive index of the analyzed medium and therefore it depends only on parameters of the sensor element. The resolution is partly influenced by the performance of the sensor element –the shape of the SPR dip may influence the accuracy with which the position of the SPR dip is determined.

As the sensing element is intended to be interrogated with non-polarized light, the sensor response to both TE and TM polarized light waves is of interest. Moreover, the response of the sensor element apart from SPR has to be analyzed as it is used as a reference. In the following analysis the influence of the sensor element parameters on the shape of the SPR dip is studied first. Then, the study of the influence of the high refractive index overlayer (which tunes the operation range of the sensor element towards aqueous environment) is presented. Finally, the influence of the design parameters on the sensor sensitivity is determined.

The following parameters were used for the modeling of the sensing element:

- An equivalent planar waveguide with the following parameters [76]: $n_{waveguide}=1.4573$, $n_{substrate, \, superstrate}=1.4533$ for a wavelength of 825 nm and $h_{waveguide}=5.26$ µm. Dispersion is taken from [79].

- The gold film permittivity is fitted using the data from [80]:

$$\varepsilon_{Au} = 20.253 - 34.4 \times 10^{-3} \lambda - 22.18 \times 10^{-6} \lambda^2 + i\left(3.57 - 8.5 \times 10^{-3} \lambda + 7.22 \times 10^{-6} \lambda^2\right), \quad (3.4.1)$$

- The refractive index of the tantalum pentoxide overlayer is assumed to be:

$$n_{Ta_2O_5} = 1.878 + 1.784 \times 10^4 \lambda^{-2} + 5.27 \times 10^8 \lambda^{-4}, \quad (3.4.2)$$

where λ is in nanometers. A homogenous, non-dispersive and infinitely thick medium with the refractive index n_{medium} is used as the model analyzed medium.

SPR Dip Shape

In Fig. 3.4.2 the relative transmitted power of the TM_0 mode assuming various thicknesses of the gold film in linear (Fig. 3.4.2b) and logarithmic (Fig. 3.4.2a) scales is shown. As it will be clear later, in the designed system a well shaped minimum in the linear scale is of interest, which corresponds to gold film thicknesses greater than 50 nm (Fig. 3.4.2b).

In Fig. 3.4.3 we can see the influence of the amount of the remaining cladding (parameter d_0) for various gold film thicknesses. From Fig. 3.4.3 it can be seen that the determination of the gold film thickness h_{Au} and the remaining amount of the cladding (d_0) from the depth and *FWHM* of then SPR dip is not unambiguous. For example, the

dip corresponding to h_{Au}=55 nm and d_0=1 µm is very similar to that with h_{Au}=65 nm and d_0=0 µm.
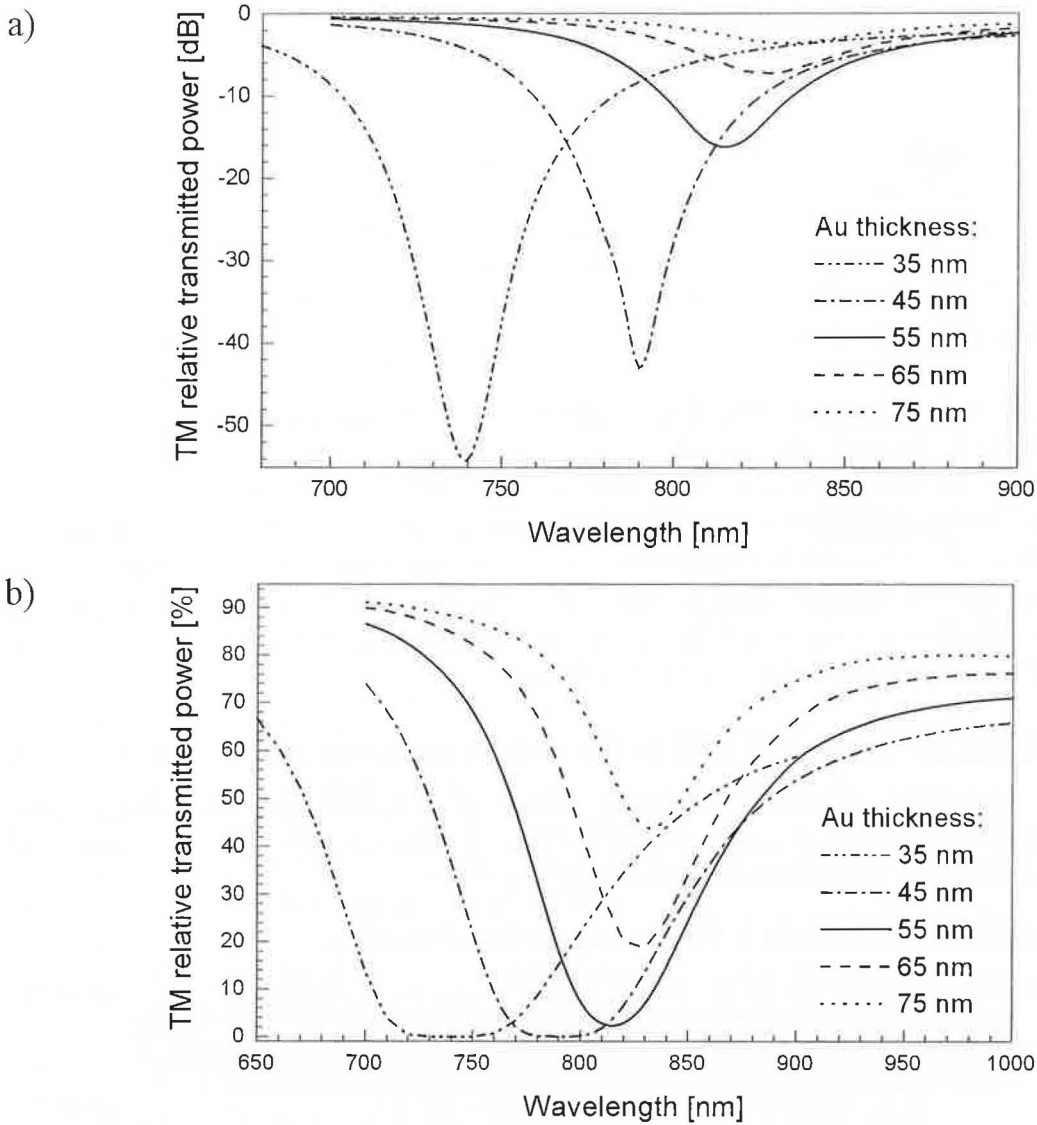
a)

b)

Fig. 3.4.2 Relative transmitted power of the TM_0 guided mode for different gold film thickness for d_0=0 µm, n_{medium}=1.3934 using logarithmic (a) and linear (b) scales.

Fig. 3.4.4 and Fig. 3.4.5 show relative transmitted powers of the TE_0 and TM_0 modes when the SPW is not excited (for n_{medium}=1). The relative transmitted power of the TE_0 mode for $n_{medium} \cong 1.3934$ (when the SPR condition for the TM_0 mode is fulfilled) was also calculated and in comparison with Fig. 3.4.4 no changes were observed. Fig. 3.4.4 and Fig. 3.4.5 were recalculated also for different thicknesses of the gold film resulting in no change. The modulation of the signal in Fig. 3.4.4 and Fig. 3.4.5 is believed to originate in the inaccuracy of the used BEM.
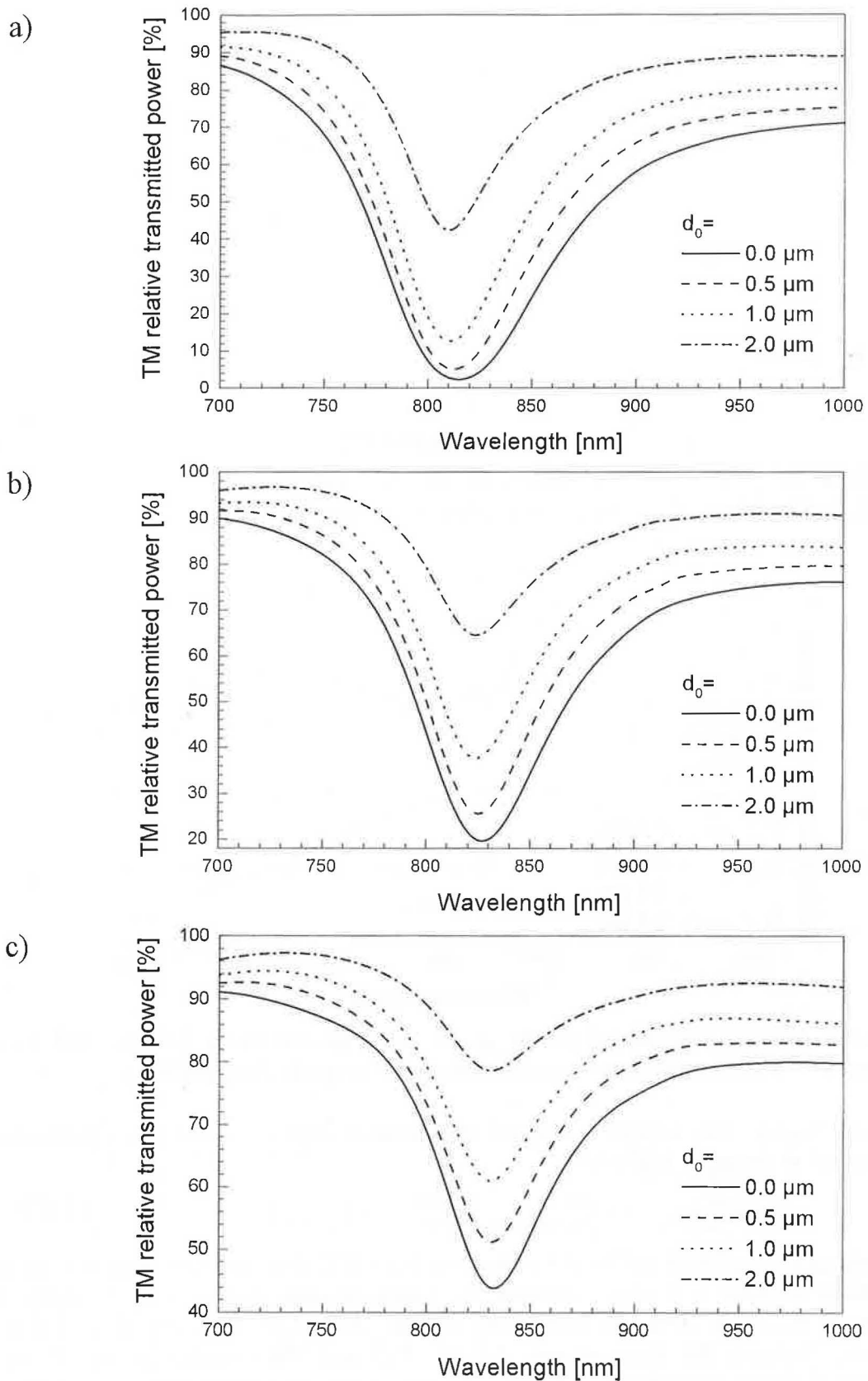
26

Fig. 3.4.3 Relative transmitted power of the TM_0 guided mode for the gold film thickness of a) 55 nm, b) 65 nm, c) 75 nm, and for different amounts of the remaining cladding, n_{medium}=1.3934.
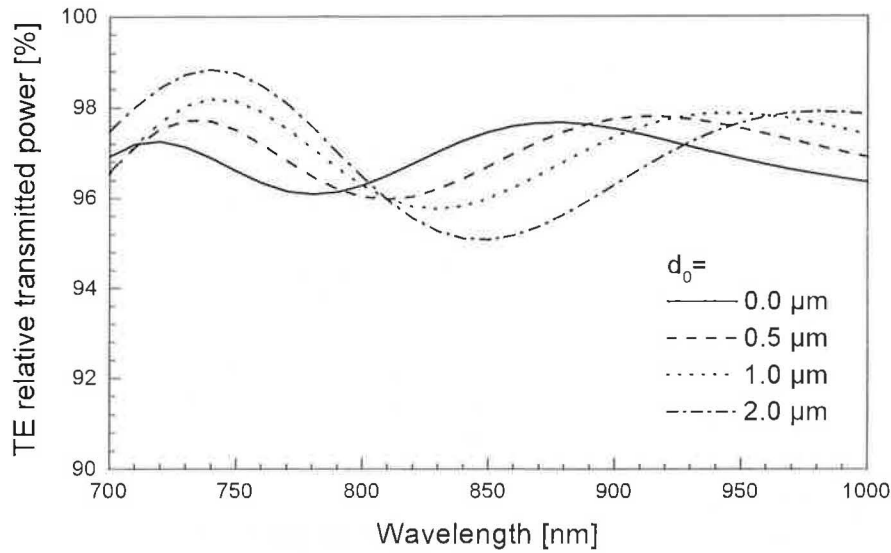
Fig. 3.4.4 Relative transmitted power of the TE$_0$ guided mode for the gold film thickness of 55 nm for different amounts of the remaining cladding and for $n_{medium}=1$.
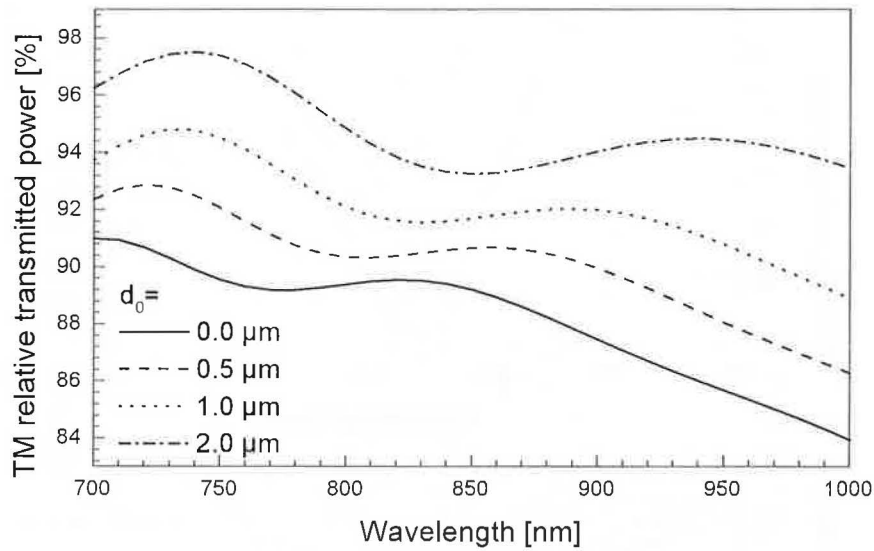

Fig. 3.4.5 Relative transmitted power of the TM$_0$ guided mode for the gold film thickness of 55 nm for different amounts of the remaining cladding and for $n_{medium}=1$.

Choosing $n_{medium}=1$ as a reference signal, the element response when a non-polarized light is used at the input is given by:

$$S = \left(I^{TM}_{n_{medium}=n_{resonant}} + I^{TE}_{n_{medium}=n_{resonant}} \right) \Big/ \left(I^{TM}_{n_{medium}=1} + I^{TE}_{n_{medium}=1} \right). \tag{3.4.3}$$

This response S is plotted in Fig. 3.4.6. Because in (3.4.3) there is a sum of the resonant TM$_0$ mode response and nearly constant TE$_0$ mode response (Fig. 3.4.4), the product leads to a shallower SPR dip comparing to the TM$_0$ mode SPR dip (Fig. 3.4.3). Moreover, because the input signals for the TE$_0$ and TM$_0$ modes are equal, the minimum in the response function S cannot be deeper than 50 percent of the signal apart from the resonance due to the TE polarized background.
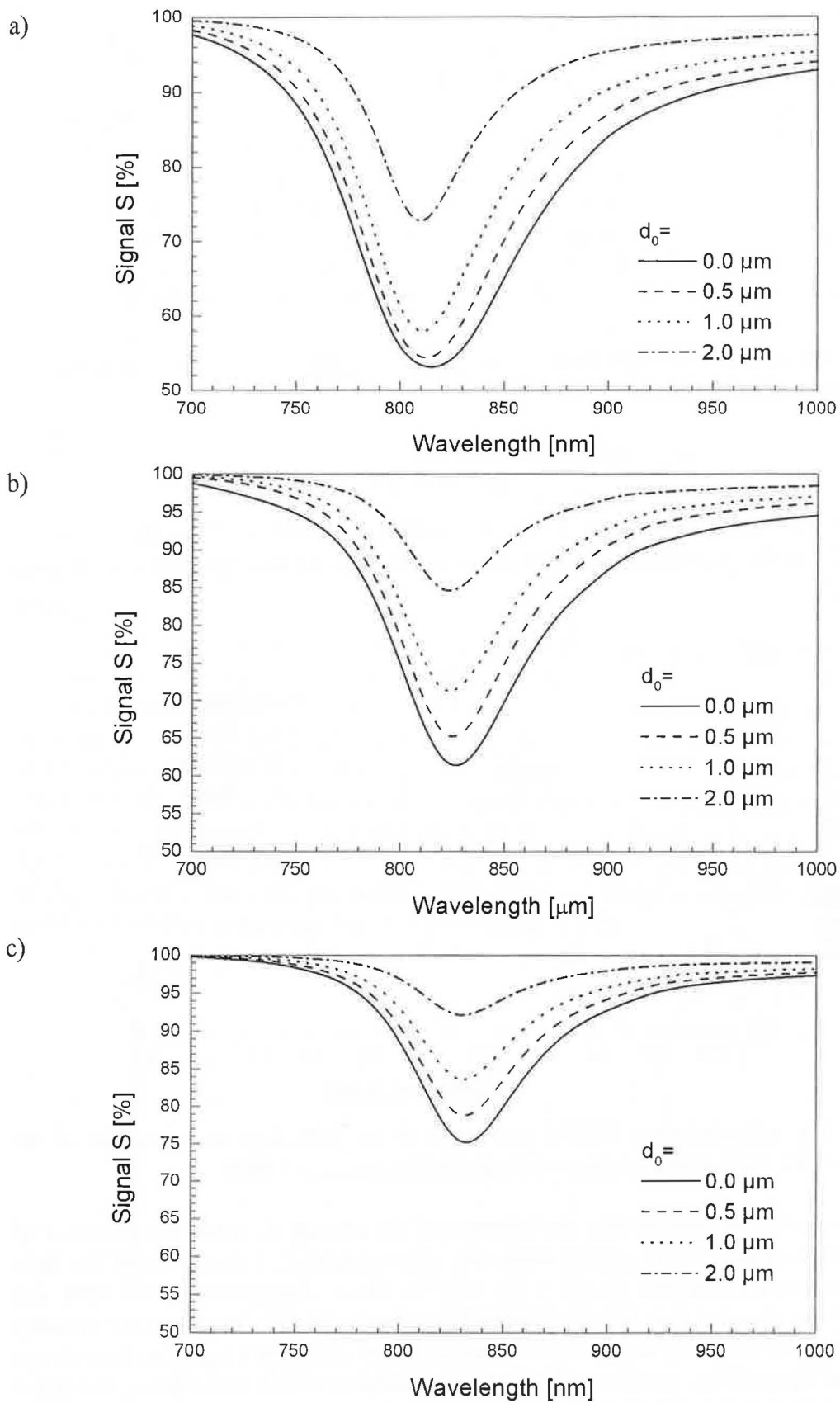
Fig. 3.4.6 Sensor element response S for the gold film thickness of: a) 55 nm, b) 65 nm, c) 75 nm, and for different amounts of remaining cladding, $n_{medium}=1.3934$.

The accuracy of resolving the position of the SPR dip, which influences the sensor resolution, could be influenced by the width (*FWHM*) as well as by the depth of the dip. Intuitively, a narrow and deep dip should be the goal of the design. From the fact that the SPR dips cannot be deeper than 50 percent of the signal out of the SPR and from Fig. 3.4.6 and Fig. 3.4.2a it follows that h_{Au}<55 nm may lead to broader, but not deeper SPR dips, which is the reason why thinner gold films are not preferred. For a thicker gold film, these relations are more complicated. We will compare the dips based on the ratio between the depth and the *FWHM* of the dips as a function of d_0 for various gold film thicknesses (Fig. 3.4.6); Fig. 3.4.7. This parameter could be minimized by a proper combination of d_0 and h_{Au}, e. g., for $d_0 \cong 1$ μm the optimum is h_{Au}=55-65 nm.

In order to derive the value of *FWHM* and depth of the SPR dips, they were fitted with a Lorentz function modified by a linear term:

$$y = y_0 + b\lambda + \frac{2A}{\pi} \cdot \frac{w}{4(\lambda - \lambda_c)^2 + w^2},$$ (3.4.4)

where y_0 is the vertical offset, A is the area below the function, w is the Lorentzian *FWHM*, λ_c is the position of the minimum of the Lorenz function and b is a linear coefficient.
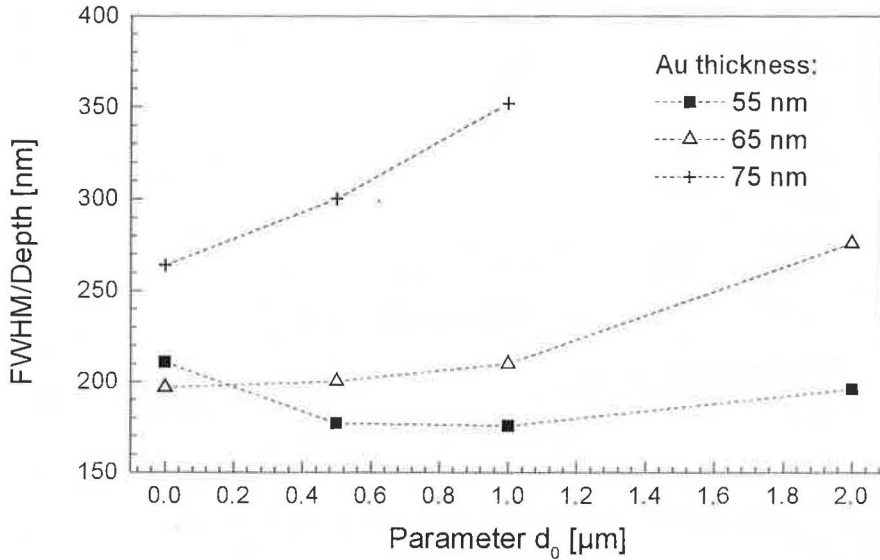

Fig. 3.4.7 The ratio between *FWHM* and depth of the SPR dips as a function of the parameter d_0 for various thicknesses of the gold film, n_{medium}=1.3934.

In order to get deeper insight into the behavior of the sensing element, the influence of the SPR on the phase of the guided wave was also calculated. Calculation of the light phase at various wavelengths accounts not only for phase changes due to the SPR, but also for phase changes due to wavelength-dependent effective length of the sensing element (the effective length is given by number of periods which light has to undergo propagating through the structure). To distinguish between these two effects, the phase difference between the TM and TE polarizations was calculated, Fig. 3.4.8. It can be seen that SPR is accompanied with a local phase shift in the TM polarization.
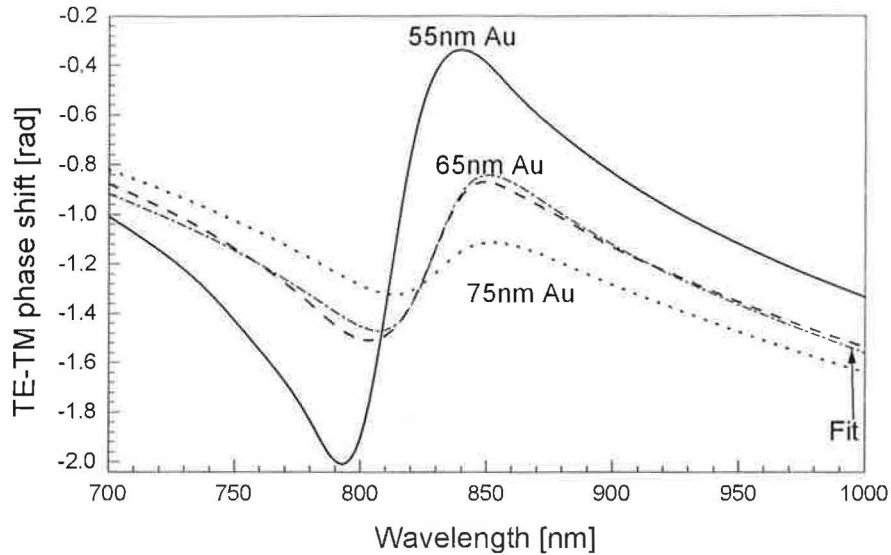
Fig. 3.4.8 Phase shift between the TM_0 and TE_0 guided modes for several values of h_{Au}, for $d_0=0$ μm and $n_{medium}=1.3934$. The fit is made using (4.3.10).

Tuning Overlayer

To develop a biosensor it is necessary to tune the operation range of the sensor element towards aqueous environment, whose refractive index is close to 1.33. On the contrary, the investigated sensing element with a bare gold film has its operation range close to the refractive index of 1.4. This mismatch can be overcome by adding a high refractive index dielectric overlayer [64, 81]. This additional layer changes the propagation constant of the SPW and consequently the spectral position of the resonance. The tuning effect of the additional tantalum pentoxide dielectric overlayer is demonstrated in Fig. 3.4.9 and Fig. 3.4.10. From Fig. 3.4.9 it can be seen that the overlayer shifts the position of the resonance, but does not significantly affect the shape of the SPR dips. This can also be seen when comparing Fig. 3.4.10 with Fig. 3.4.2b.
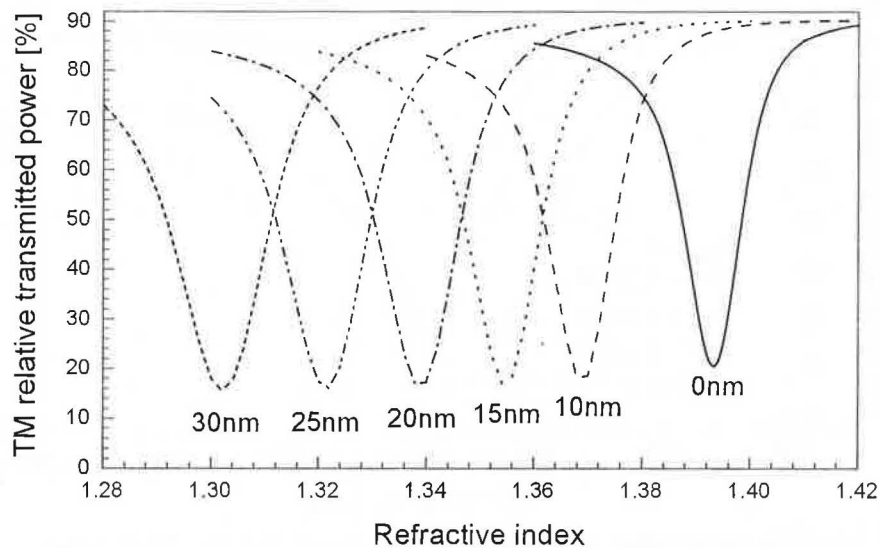

Fig. 3.4.9 Relative transmitted power of the TM_0 mode when varying the thickness of the tantalum pentoxide overlayer for a gold film thickness of 65 nm and $d_0=0$ μm.
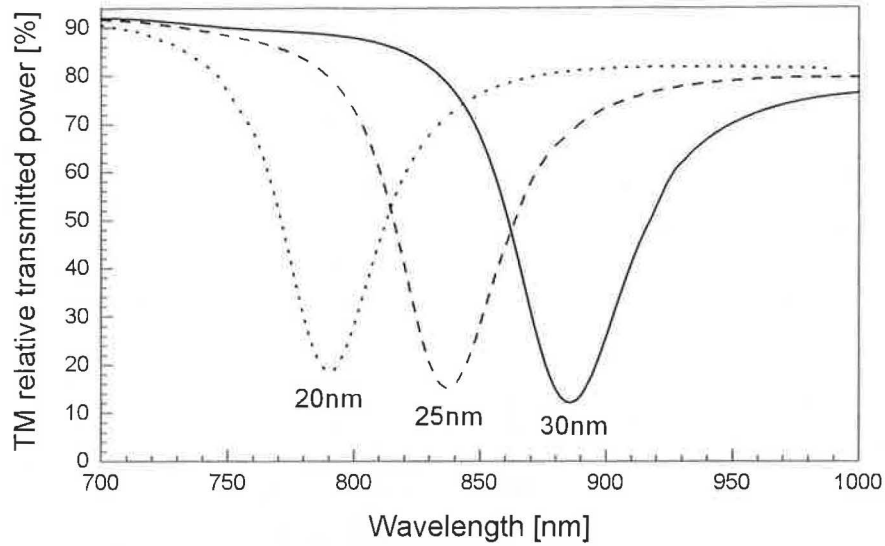
31

Fig. 3.4.10 Spectral sensor element response of the TM_0 mode when varying the thickness of the tantalum pentoxide overlayer for a gold film thickness of 65 nm, n_{medium}=1.326 (water) and d_0=0 µm.

Sensitivity

The sensitivity is defined as a spectral shift of the SPR dip induced by an unity change in the refractive index of a homogenous analyzed medium.

The influence of the thickness of the remaining cladding and the gold film thickness on the sensor sensitivity is shown in Fig. 3.4.11 and Fig. 3.4.12. As can be seen, the sensor sensitivity, which is nearly independent of the gold film thickness h_{Au} (Fig. 3.4.12) as well as of the thickness of the remaining cladding d_0 (Fig. 3.4.11), is about 7600 nm/RIU.
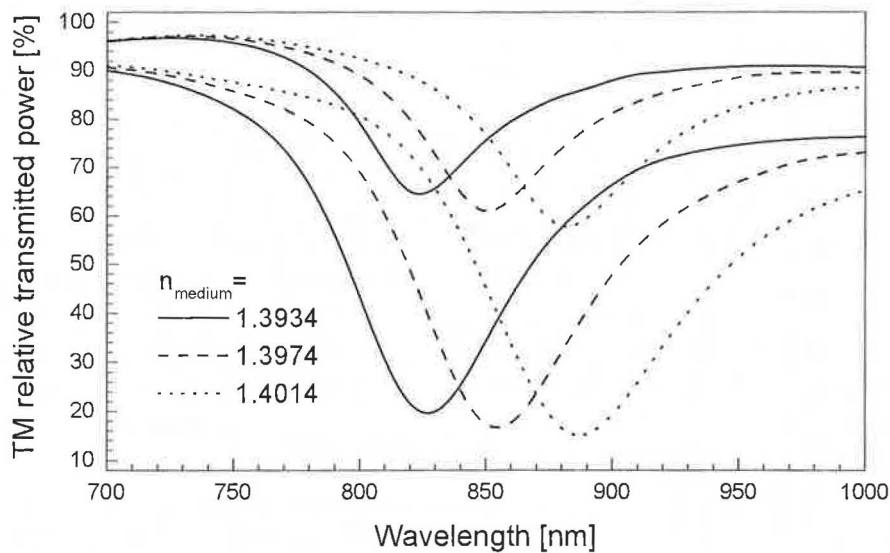

Fig. 3.4.11 Relative transmitted power of the TM_0 mode, for d_0=0 µm (deeper dips) and d_0=2 µm (shallower dips), assuming various values of n_{medium}. The gold film is 65 nm thick.
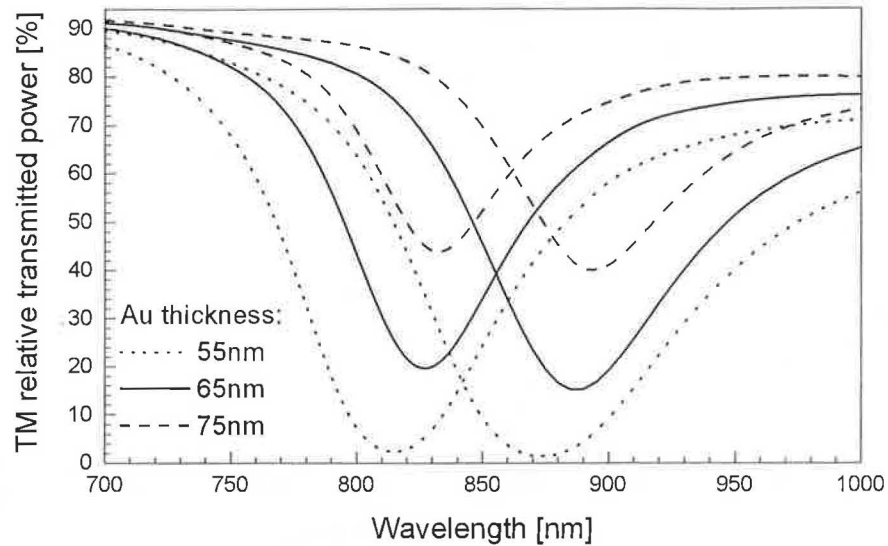
Fig. 3.4.12 Relative transmitted power of the TM_0 mode for $n_{medium}=1.3934$ (left-hand dips) and $n_{medium}=1.4014$ (right-hand dips) assuming various values of the thickness of the gold film and $d_0=0$ μm.

The influence of the tantalum pentoxide overlayer on the sensitivity of the sensor element is shown in Fig. 3.4.13. The sensitivity decrease is caused by the fact that a smaller fraction of power of the evanescent field of the SPW propagates in the analyzed medium. Tuning the operation range towards aqueous environment, for which the thickness of the tantalum pentoxide has to be 20 nm (Fig. 3.4.10), lead to sensitivity decrease down to 3100 nm/RIU (Fig. 3.4.14). This value is by a factor of 2.5 smaller than that for the structure without this overlayer (Fig. 3.4.11).
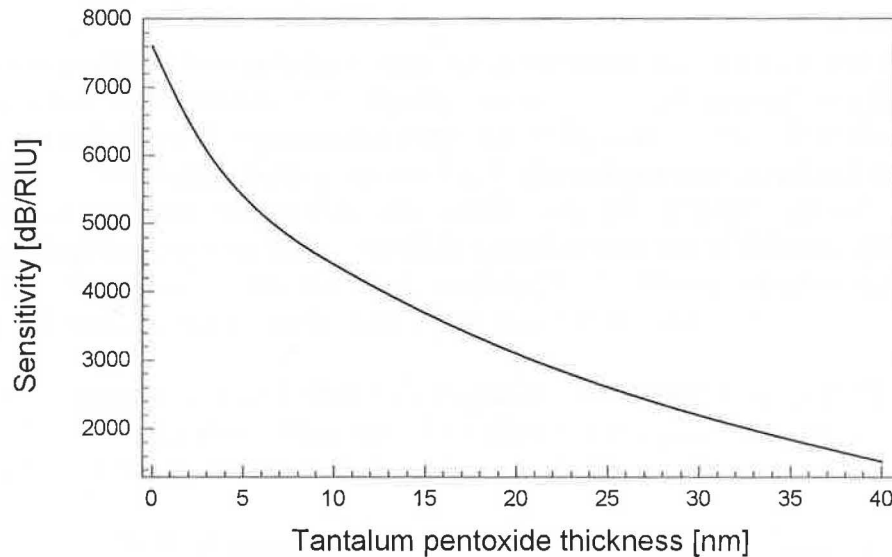

Fig. 3.4.13 Sensitivity of the sensor element as a function of the thickness of the tantalum pentoxide overlayer for the gold film 65 nm thick and $d_0=0$ μm.
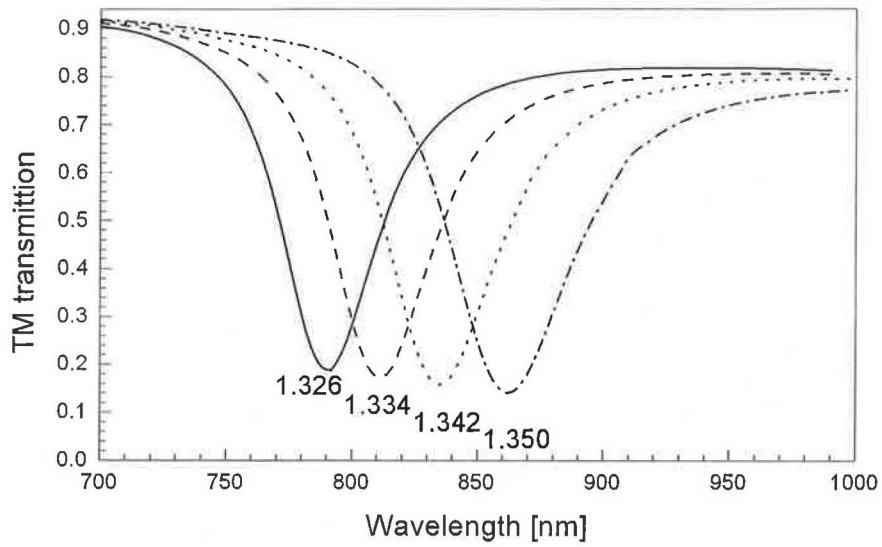
33

Fig. 3.4.14 Relative output power of the TM_0 mode for various values of n_{medium}. The tantalum pentoxide overlayer and gold film thicknesses are 20 nm and 65 nm, respectively, and d_0=0 μm.

4. Sensor System

Before building the sensor system, all its components are characterized first. Then the analysis of the whole system follows. Finally, the performance of the built sensor is tested.

4.1   Support components

Except for the sensor element, all the sensor system components are referred to as support components. To characterize the support components, fiber polarizers and polarization controllers were used. The used fiber polarizers were made in our laboratory and have an extinction ratio better than 40 dB and insertion losses less than 1 dB. The coil polarization controllers with loop diameters of 3.2 cm were fabricated in our workshop.

Light Source

The source for spectral SPR fiber optic sensor has to be capable of launching sufficient optical power into a single-mode optical fiber in a rather broad spectral range as the *FWHM* of SPR dips are in a range of 50-70 nm (Table 4.2.1).

To couple high power of a polychromatic light into a single-mode fiber, superluminiscent diodes (SLD) are currently most often used. The advantage of SLD is that the emitted light has directional characteristics similar to that of a laser diode, but has much broader spectrum similar to that of a luminescent diode – typically with a *FWHM* of 15-30 nm. The problem with the bandwidth of a standard SLD, which is narrow with respect to our requirements, can be overcome by using an SLD based on a two-state quantum well heterostructure.

We used a pigtailed two-quantum well heterostructure superluminiscent diode SLD-371, produced by Superlum Ltd., Russia. As its spectrum depends on the pumping current, we stabilized the current at a value for which the spectrum is widest. To reach stabilization of the output power, the device is also temperature stabilized at 25^0C. The specified current and temperature are maintained by 'PILOT' driver, which was purchased together with the SLD. The SLD specifications are as follows: spectral center at 816 nm, *FWHM* of 72 nm, minimal wavelength of 775 nm, maximal wavelength of 865 nm and spectral ripples of the power less than 0.6 percent.

Our SLD is spliced to a 2×2 fiber side-polished fiber-based coupler [82], which was fabricated in our laboratory. Then these two devices were packaged into a compact box and therefore all the presented source spectra were taken at the output of the coupler.

The set-up for SLD characterization is shown in Fig. 4.1.1. The Lyot depolarizer described below is used in front of the spectrum analyzer in order to suppress polarization-dependent behavior of the spectrum analyzer. The measured spectra are in Fig. 4.1.2. As the polarization controller is not capable of full polarization control in such a broad spectral region, the spectra are measured in discrete spectral regions of 20 nm wide. We assume that the light emitted by the SLD can be decomposed into non-polarized non-coherent part and polarized coherent part. 'Max' denotes a value measured when the polarization controller is in a position in which the maximum amount of light passes through the polarizer. This corresponds to the sum of the

35

intensity of the polarized part and one half of intensity of the non-polarized part of the emitted light. This is because the non-polarized light is not influenced by any change in the polarization controller and every time one half of its power passes through the polarizer. 'Min' corresponds to the minimum amount of light passing through the system. In this situation the whole power of polarized light and one half of power of the non-polarized light are lost in the polarizer. In Fig. 4.1.3 the polarized, non-polarized, and whole signals emitted by the SLD are shown. These spectra are calculated from the measured spectra in Fig. 4.1.2; the intensity of the non-polarized light is double the 'Min' intensity, the intensity of the polarized part is the difference between 'Max' intensity and the intensity of the non-polarized light.
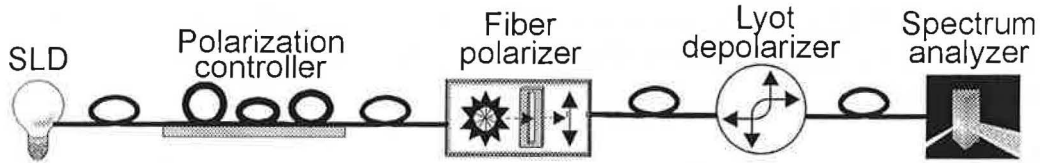

Fig. 4.1.1 Set-up for the SLD spectrum characterization.

Calculating the total power and the power carried by the polarized part of the light having passed through the system as areas under the curves in Fig. 4.1.3, we can estimate that the degree of polarization of the light emitted by the SLD is of about 63 percent.
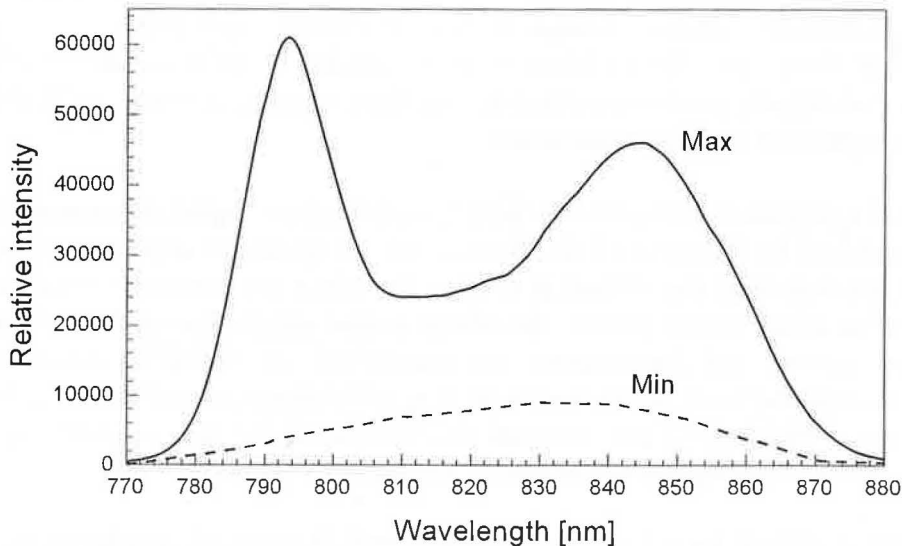

Fig. 4.1.2 Measured characteristics of the SLD obtained using the set-up in Fig. 4.1.1. 'Max' and 'Min' values correspond to maximum and minimum output signals attained by changes in the polarization controller.

For further modeling of the sensor system it is useful to fit the spectra of the SLD by an analytical function. The fits of the polarized as well as of non-polarized parts of the SLD spectra were performed using a sum of Gaussian functions:

$$I = \sum_i \frac{A_i}{w_i \sqrt{\pi/2}} \cdot \exp\left[-2 \, \frac{(\lambda - \lambda_i^c)^2}{w_i^2} \right],$$

(4.1.1)

where I is the output intensity, A is the area under the fitted curve, w is the Gaussian width and λ^c is the center of the fitted Gauss function. The fitted curves are plotted in Fig. 4.1.3, the fitted parameters are in Table 4.1.1; for the polarized part of the SLD spectrum is $i = 1,2,3$, for the non-polarized part then $i = 4,5$.

Table 4.1.1 Parameters of the SLD emitted spectra.

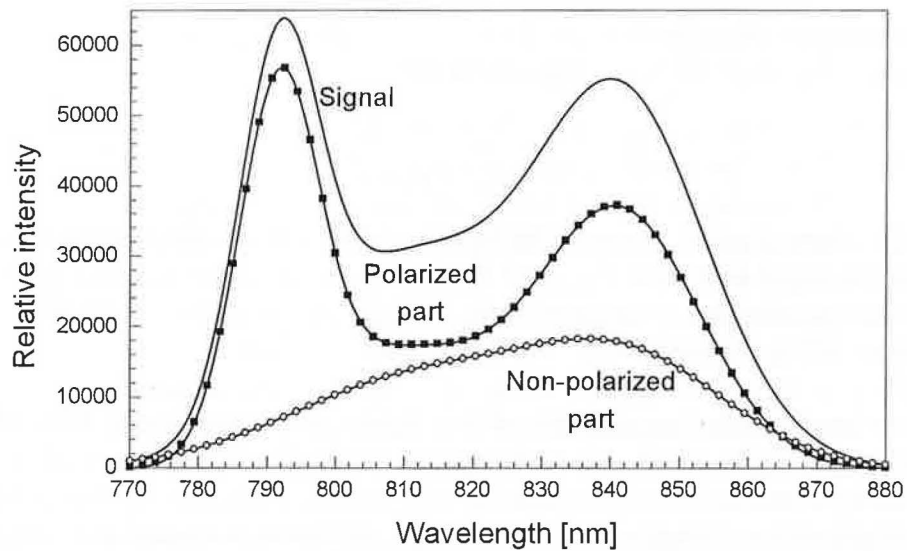| i	$A_i \times 10^5$	$w_i \; [nm]$	$\lambda_i \; [nm]$
1	7.33	11.56	791.61
2	5.11	25.43	809.23
3	10.75	23.43	841.04
4	6.01	37.469	812.67
5	5.03	28.786	842.98

Fig. 4.1.3 Spectrum of the SLD calculated from Fig. 4.1.2 (lines) and multipeak Gauss fits for polarized and non-polarized parts according to (4.1.1) and Table 4.1.1 (dots).

Fiber Lyot Depolarizer

As the Lyot depolarizer consists of high birefringent elements, its fiber version requires the use of *high-birefringent* (**HiBi**) fibers. In such a fiber, a permanent linear birefringence is induced via elasto-optic effect by applying different tension along the x and y axes (Fig. 3.1.1) or via a non-circular geometry (elliptical fiber core), so that the fiber behaves like a birefringent medium with modal birefringence B given by:

$$B = \frac{\beta_x - \beta_y}{2\pi/\lambda},$$

(4.1.2)

where β_x and β_y are the propagation constants along the principal axes of birefringence (let us denote them as x-axis and y-axis). In a HiBi fiber any mechanical disturbances cannot change β_x into β_y and vice versa, because their difference (and consequently B) is large enough.

HiBi fibers are most commonly characterized by two parameters: *h- parameter* and *beat length L_c*. The beat length corresponds to a distance L_c at which the phase delay between the light propagating in TE and TM polarized modes is equal to 2π:

$$L_c = \lambda/B. \qquad (4.1.3)$$

Typical values of L_c range from 1 mm to 5 mm at λ=633 nm. A segment of a HiBi fiber with a length of tens of cm then behaves like a high-order wave retarder with phase retardation along the principal axes given by:

$$\varphi(L,\lambda) = 2\pi \frac{\lambda_0}{\lambda} \frac{L}{L_c}, \qquad (4.1.4)$$

where L is the length of the HiBi fiber and L_c is the beat length at the wavelength of λ_0. The greater the L is comparing to the L_c, the smaller spectral width corresponds to full polarization conversion over the spectral region, as follows from (4.1.4).

The *h*-parameter characterizes the degree of *h*olding the polarization and is, in fact, a measure of fiber imperfections. It is defined as:

$$h = \frac{1}{2L} \ln \left(\frac{P_{max} + P_{min}}{P_{max} - P_{min}} \right), \qquad (4.1.5)$$

where the plane of polarization of the light launched into the fiber of length L is aligned to either principal axis, and P_{max} and P_{min} are portions of the emitted power with the polarization parallel and orthogonal to the excited axis, respectively. Typical values of h range from $10^{-6}\,\mathrm{m}^{-1}$ to $10^{-4}\,\mathrm{m}^{-1}$.

The fiber Lyot depolarizer consists of two pieces of a single-mode HiBi fiber spliced together at an angle of 45 deg with respect to their principal axes. If a broadband polarized light source is coupled into the depolarizer, each spectral component appears at the output with a different polarization state and upon averaging over the bandwidth, the output is depolarized. The choice of the 45 deg angle makes the depolarizer performance independent of the input polarization state. If depolarization is not achieved by the first fiber piece, it is achieved by the second one.

The time delay between the light propagating along the two principal axes of the first fiber piece τ_1 (length L_1) has to be greater than the coherence time τ_c of the light source, and analogously, for the second piece (length L_2) it should hold $\tau_2 \gg \tau_c$. As there is danger that the time delay τ_1 will be compensated for in the second fiber piece by τ_2, it is necessary to fulfil also: $|\tau_2 - \tau_1| \gg \tau_c$. This is the reason why the second fiber piece has to be at least twice as long as the first one. According to [83], if a HiBi fiber with a beat length of B=1.5*mm* at λ=633 nm and a luminescent diode emitting at 840 nm with a Gaussian spectrum with the *FWHM* of 15nm are used, $\tau_1 = \tau_c$ corresponds to $L_1^{\tau_1 = \tau_c} = 11$ cm.

The performance of the depolarizer depends on the accuracy of the 45 deg splice [84], the length of the fibers with respect to the HiBi fiber beat length [83,85] and on the fiber *h*-parameter [83,85]. Using a fiber with $h \approx 10^{-5}\,\mathrm{m}^{-1}$, the attainable depolarization corresponds to P~0.01 [86], where P is the degree of polarization defined through the coherence matrix [86]. As follows from [86], to reach P~0.01 it is necessary to splice

the two fiber pieces with an accuracy better than ±0.25 deg. To reach the value of $P \sim 0.01$, the shorter fiber piece has to have its length $L_1 > 4L_1^{\tau_1 = \tau_c}$ [83]. When we, however, intend to spectrally analyze the depolarized light, the length of the used HiBi fibers has to be higher, because the depolarization effect has to take place over a narrower spectral region corresponding to the used spectrum analyzer resolution.

To construct the Lyot depolarizer we used a HiBi Bow-Tie fiber from Fibercore Ltd., England, with parameters shown in Table 4.1.2.

Table 4.1.2 Parameters of the used HiBi fiber.

FIBER TYPE	HB800
Fiber diameter	125 μm
Cut off wavelength	782 nm
Numerical aperture	0.13
Beat length at 633 nm	1.5 mm
h-parameter	$1\text{-}3 \times 10^{-5}$ m^{-1}

The HiBi fiber was spliced using FFS-1000 spicing machine from Vytran Inc., USA, in IPHT, Jena, Germany, which allows adjusting the angle of the splice of the HiBi fibers with an accuracy of 0.05 deg. Because of a heating and a torsion of the fiber-ends during the splicing process, the final angle differs from the adjusted one, so that the resulted accuracy of the angle is about 0.25 deg, which allows preparation of the depolarizer with $P \sim 0.01$. A depolarizer with $L_1 = 1.3$ m and $L_2 = 2.7$ m was fabricated. Its length is sufficient to effectively depolarize the light from our source [87]. The performance of the depolarizer is limited by the inaccuracy of the 45 deg angle splice [87]. At both end-faces of the depolarizer, 1.3 m long pigtails from a standard single-mode fiber were spliced and the whole device was finally packaged.

The prepared depolarizer was characterized using the set-up shown in Fig. 4.1.4. The first fiber polarizer is employed in order to suppress the non-polarized part of light emitted by the SLD. The prepared depolarizer had $P = (8 \pm 4) \times 10^{-3}$, the deviation is given by the accuracy of the used photodetector. To verify the capability of the depolarizer to depolarize also a narrow-band spectral signal, the set-up in Fig. 4.1.5 was used, where a polarization dependent spectrum analyzer described in detail below is used. It was found that the prepared depolarizer effectively depolarized a narrow-band spectral signal the width of which is given by the spectral resolution of the used spectrum analyzer.
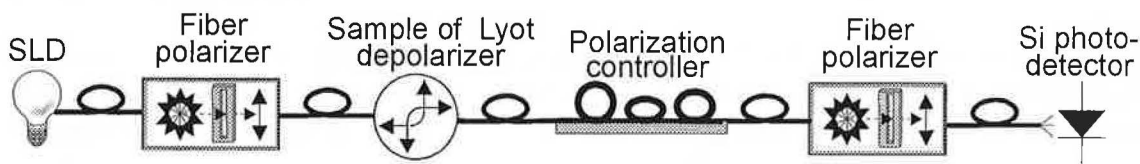

Fig. 4.1.4 The set-up for characterizing the prepared depolarizer.
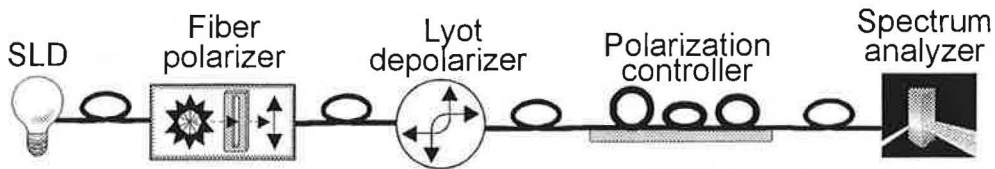
Fig. 4.1.5 The set-up for studying the capability of the prepared depolarizer to depolarize light in a narrow spectral region.

Multimode Fiber Mode Mixer

Light propagating in a multimode optical fiber may suffer decrease in the degree of coherence and polarization, because the light propagates in different fiber modes, which have different path lengths. Ideal and most stable distribution of light in a multimode fiber is the steady-state mode distribution [88]. There are several approaches to mixing fiber modes in order to attain the steady-state mode distribution [88]. The most straightforward approach includes fiber bending which results in strong intermodal coupling. It can be realized, for example, by winding the fiber around a mandrel with a small diameter (typically of 10-30 mm [88]). Another approach is based on a quasi-random fiber joining during which the fiber modes are efficiently mixed. It can be realized, for example, by etching the end-faces of one of the fibers [89], by joining step-index and gradient-index fibers [88] or by tapering a fiber [88].

Our mode mixer was fabricated of a 1.5 m long piece of a multimode fiber with TECS cladding, type FT-400-EMT, purchased from Thorlabs Ltd., USA with the core diameter of 400 µm. The used mandrel was 15 mm in diameter and the fiber was wound ten times around it. The performance of the mode mixer was studied in the set-up shown in Fig. 4.1.6. As a reference, the signal corresponding to a specific position of the polarization controller was used. Typical change in the detected spectrum induced by a change in the polarization controller is shown in Fig. 4.1.7.
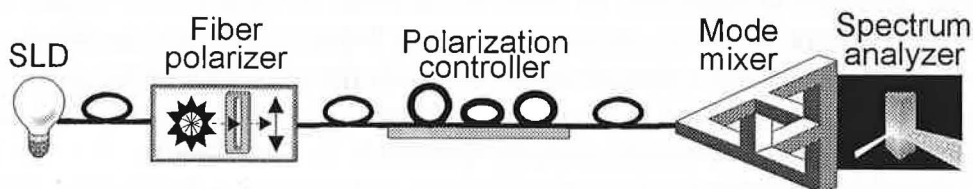

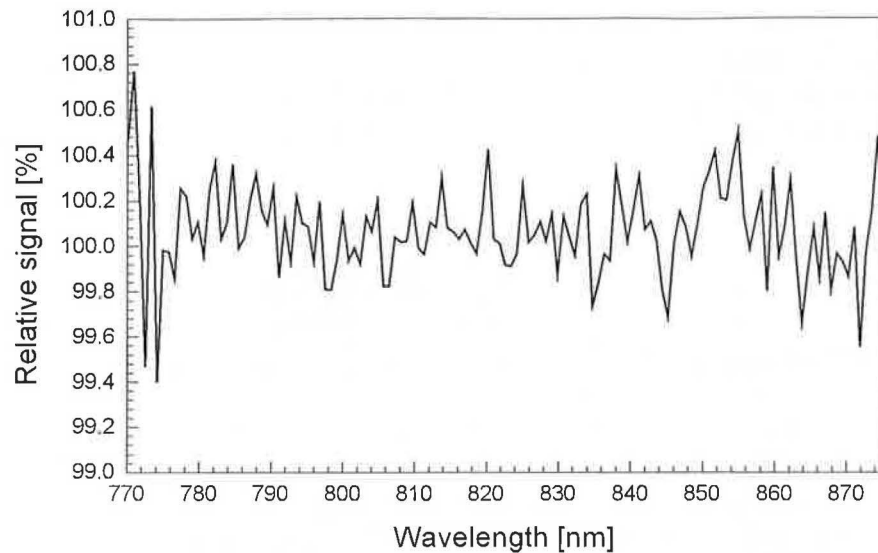**Fig. 4.1.6** The set-up for studying the mode mixer performance.

Fig. 4.1.7 Noise determined by the performance of the mode mixer measured in the set-up shown in Fig. 4.1.6. After the reference spectrum is registered, position of polarization controller is changed and the signal is measured.

Spectrum Analyzer

In our experiments we used a spectrum analyzer MSC-501 produced by Karl Zeiss, Ltd., FRG, whose photodetector element is formed by an array of silicon photodiodes. It allows simultaneous measurement of the entire spectrum. The parameters of the spectrum analyzer are as follows:

- Optical entrance: circular aperture with a diameter of 0.5 mm, numerical aperture (*NA*) equal to 0.2, the connection with the signal fiber realized via a mounted SMA 905 connector.
- Grating with flat-field correction, 248 l/mm (center), blazed for approximately 220 nm.
- Absolute wavelength inaccuracy less than 0.3 nm.
- Reproducibility better than 0.1 nm.
- The temperature-induced drift less than 0.01 nm/°C.
- Spectral distance of pixels is 0.8 nm.
- Number of pixels is 1024.
- Wavelength range is 215 nm-1015nm.
- Integration time is 12 ms-5000 ms.
- 16-bit A/D converter.

The response function of the spectrum analyzer in Fig. 4.1.9 is measured in the set-up shown in Fig. 4.1.8, where a laser diode with a narrow spectral width (*FWHM* of 0.1 nm) is used; the fit resulting in w=3.5 nm is performed using a single Gaussian function (4.1.1).

As it was intended to use single-mode fibers at the input of the spectrum analyzer, polarization properties of the spectrum analyzer were of interest. The polarization sensitivity of the spectrum analyzer originates in polarization-dependent diffraction efficiency of the grating used in the spectrum analyzer. This phenomenon was studied in the set-up shown in Fig. 4.1.10 for the spectral range of the SLD. A fiber polarizer

41

was used in order to suppress the non-polarized portion of light emitted by the SLD. Changing the position of the polarization controller, the maximum difference for various wavelengths was measured. It was found that changes in the light polarization state can change the measured signal by a factor of 4, over the entire spectral range.
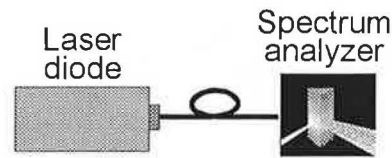

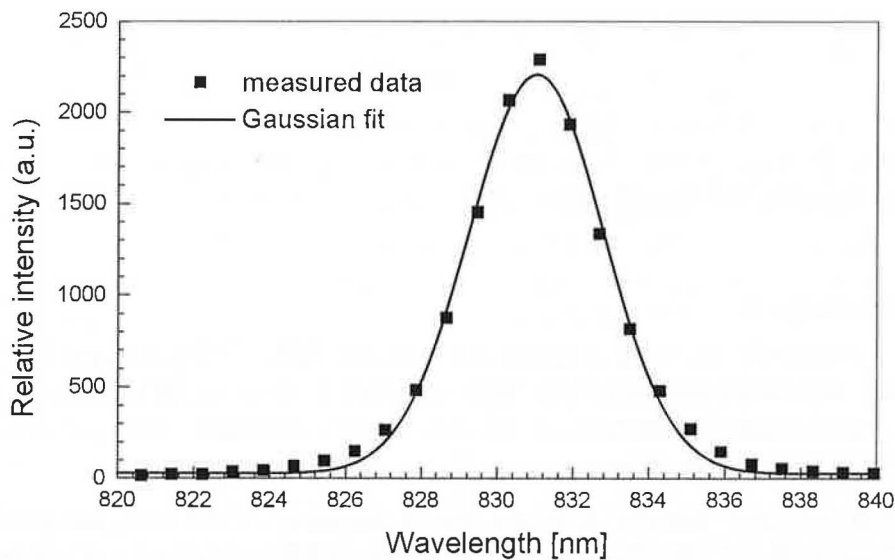**Fig. 4.1.8** Experimental set-up for measuring the response function of the spectrum analyzer.

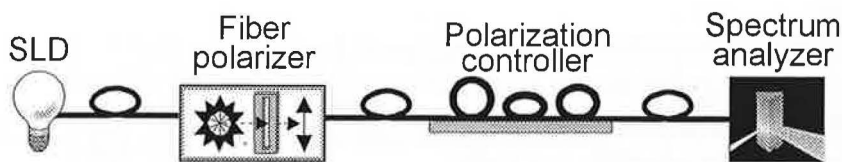**Fig. 4.1.9** Measured response function of the spectrum analyzer and its Gaussian fit.

Fig. 4.1.10 Experimental set-up for measuring polarization properties of the spectrum analyzer.

4.2   Sensor Element

Fabrication

Fiber Preparation

For our purpose single-mode fiber SM800 from Fibercore, Ltd., England, with the following parameters was used:

- core: diameter of 4.7 µm, silica doped with 5 percent (wgt.) of germanium,
- cladding: diameter of 125 µm, silica, inner part is phosphorous/fluorine-doped,
- coating: diameter of 233 µm, single coat acrylate,

- cut-off wavelength: 724 nm,
- numerical aperture (*NA*): 0.12,
- attenuation: 4.3 dB/km at 830 nm.

To get access to the field of the guided fiber mode the side-polishing technique [90,91,92] was chosen. This technique is well known from fiber optic polarizers and adjustable or polarization holding 2×2 couplers. In this technique the fiber is first bonded into a curved slot (radius *R*) engraved by a diamond saw into a fused silica block. Then, the structure is abraded and polished in order to get access to the field of the guided mode. There are generally two possibilities how to get access to the field of the guided mode – through the evanescent field of the guided mode or by a contact with the fiber core. The first approach could be realized by polishing the fiber to the vicinity of the core, the second one by polishing the fiber into the core [93]. The polishing into the core may result in structures which interact with the surrounding medium more strongly than evanescent structures. On the other hand, polishing into the core [94] results in SPR structures which exhibit large difference in the attenuation of the TE and TM polarizations of the fiber mode (typically up to 10 dB [94]), which may lead to shallowing of the SPR dips in the built sensor system (3.4.1). This argument suggests the employment of evanescent field-based structures.

Formerly developed technique of side-polishing [93] was improved in order to increase reproducibility and in order to simplify the polishing process. Using the current approach only one method for determining and controlling the parameter d_0 is used – the measurement of radiation losses by immersing the side-polished surface into a single immersion liquid with a specific refractive index.

Radiation losses γ_{rad} can be derived using mode-coupling theory. In this way we get [95]:

$$\gamma_{rad} = 10\log(e)\frac{4\pi\beta N_0^2[1-(w/V)^2]}{n_{clad}^2 k_0^2}\sqrt{\pi Ra}\int_0^1 \frac{\sqrt{1-x^2}}{\sqrt[4]{(V^2-w^2)x^2+w^2}} \tag{4.2.1}$$

$$\cdot\exp\left(-2\frac{d_0-a}{a}\sqrt{(V^2-w^2)x^2+w^2}\right)dx,$$

where:

$$w = a\sqrt{\beta^2 - n_{clad}^2 k_0^2} \;,\; V = k_0 a\sqrt{n_{sur}^2 - n_{clad}^2} \;, \tag{4.2.2}$$

where β is the propagation constant of the fundamental guided mode, N_0 is the normalization constant of the electromagnetic field of the guided mode, k_0 is the wavenumber in vacuum, a is the fiber core radius, n_{sur} *and* n_{clad}, are the refractive indices of the surrounding medium and fiber cladding, respectively and x is an integration variable.

The results for our fiber are plotted in Fig. 4.2.1. The picture shows that the coupling between the guided mode and free-space modes in the surrounding medium is a resonant effect. The resonance occurs when n_{sur} is slightly greater than the effective refractive index of the fiber guided mode.
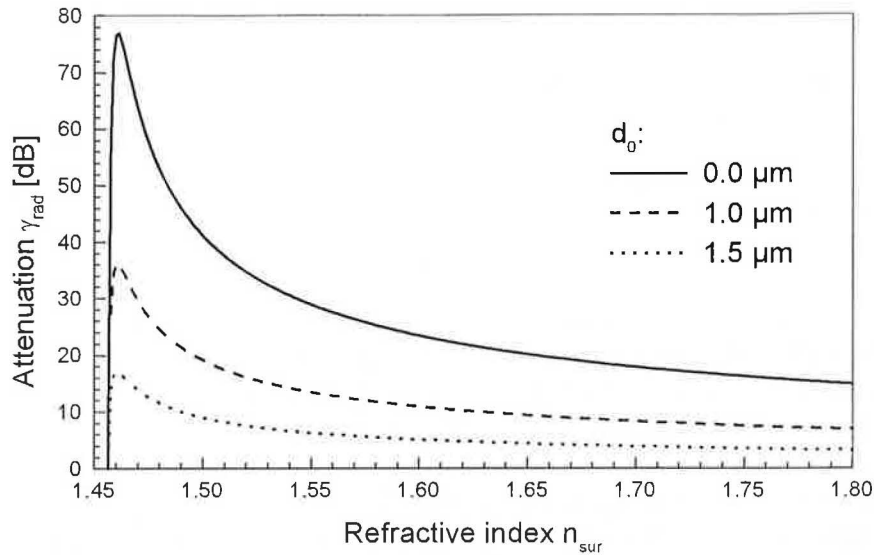
Fig. 4.2.1 Radiation losses γ_{rad} as a function of n_{sur} for various values of the parameter d_0.

Our method uses anise oil with $n_{sur}=1.556$ (measured with Abbe refractometer at wavelength of 589 nm at room temperature) as a model surrounding medium. As can be seen in Fig. 4.2.1, in the surrounding medium refractive index corresponding to the anise oil is γ_{rad} almost insensitive to n_{sur} variations, which allows us to neglect changes in the refractive indices of the anise oil due to temperature variations. Moreover, at this analyzed medium refractive index γ_{rad} strongly depends on the parameter d_0 even for 'large' d_0 ($d_0 \cong 2-3$ μm) and is also measurable for $d_0 \to 0$ μm.

The side-polishing consists of the following steps:
- In the middle of 2 m long fiber, about 2 cm of the fiber jacket is removed with a blade.
- The fiber is fixed by polyester-based glue into a curved grove made with a 150 μm thin diamond saw blade in a silica block ($23 \times 23 \times 11$ mm^3). The radius of the curved grove is $R=25$ cm, its width is about 250 μm.
- The glue is removed from the top silica block surface using abrading paper which works in wet environment. The free abrasive powder is not used, because in such case the powder is trapped in the glue.
- The surface is hand-abraded on cast iron surface with 20 μm diamond abrasive powder till the fiber begins to be abraded.
- Using 8 μm diamond abrasive powder and inspecting the radiation losses using the anise oil with $n_{sur}=1.556$, the evanescent field region is reached (there are measurable changes in γ_{rad} for $n_{sur}=1.556$ in comparison with $n_{sur}=1$ (air)).
- The polishing is performed using a paper-based polishing pad and ceroxide powder. Measuring γ_{rad}, the polishing is finished reaching the required value of d_0. If the surface is still not polished enough, sample with smaller d_0 has to be prepared.

In practice, (4.2.1) does not accurately predict the value of the parameter d_0. It is because the polished surface is not perfectly flat, as supposed in (4.2.1), but has some mild roughness. A value of d_0 in a range from 0 μm to 1 μm is attainable with the

described technique. The upper limit is given by the fact that the surface must be polished enough after reaching the evanescent field during the abrading process.

Thin Film Deposition

The polished surface was first washed in acetone and cleaned by Balzers *No.2* cleaner. Then it was dried by a flow of clean nitrogen. The electron beam evaporation of the gold film took place in evaporation machine PFEIFFER PLS 570 with a non-oil vacuum system at a temperature of 165^0C. The vacuum during the evaporation process was in order of 10^{-8} Pa, the rate of evaporation was $0.5 - 0.7$ nm/s. After cooling the samples down to the room temperature, they were moved to evaporation machine BALZERS BA510 with an oil-based vacuum pumping system. After drying by liquid nitrogen and obtaining the vacuum of approximately 10^{-8} Pa, the samples were heated up to 220^0C. Then, clean oxygen resulting in a pressure of 4×10^{-6} Pa was injected. The next step was electron beam evaporation of the tantalum pentoxide overlayer with the rate of evaporation of 0.1 nm/s.

Characterization

Experimental Set-Ups

For the fiber sensor elements analysis, three set-ups were used. The first one characterizes the interaction between the guided fiber mode and the SPW at a fixed wavelength (Fig. 4.2.2). The light from a stabilized laser diode with a wavelength of 825 nm was coupled via a microscope objective into the input fiber. The fiber passed through a coil polarization controller, which allowed us to adjust the desired polarization state in the interaction region of the sensor element. The output signal was measured with a silicon photodiode.

Fig. 4.2.2 Experimental set-up for the characterization of the sensor element samples at a fixed wavelength.

The second set-up allows observing spectral sensor element behavior with the possibility of controlling the fiber mode polarization state in the sensing element (Fig. 4.2.3). The light from an argon laser pumped Ti:sapphire laser passed through a beam splitter in order to get a reference signal. The signal light was then coupled into the input fiber via a microscope objective. In front of the sensor element sample the polarization controller was placed in order to adjust the desired polarization state in the interaction region of the sensor element. The used silicon photodetectors were wavelength-calibrated to compensate for their spectral sensitivities.

The third set-up tests the ability of the element to work in depolarized light (Fig. 4.2.4). The light from the pigtailed superluminiscent diode (SLD) passed through the Lyot depolarizer and the sensor element sample. The output was analyzed by the spectrum analyzer. After measuring the reference spectrum (using $n_{medium}=1$), no movement was performed with the output fiber of the sensor element to avoid changes in the output polarization state and thus to avoid changes due to polarization sensitivity of the spectrum analyzer.
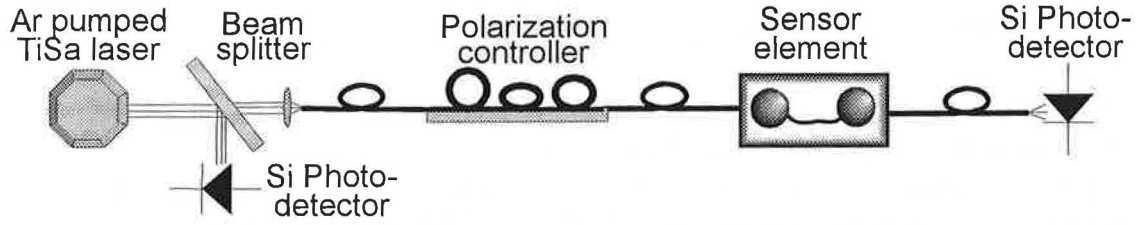
Fig. 4.2.3 Experimental set-up for the characterization of the sensor element samples in spectral domain with the possibility of controlling fiber mode polarization state in the sensing element.
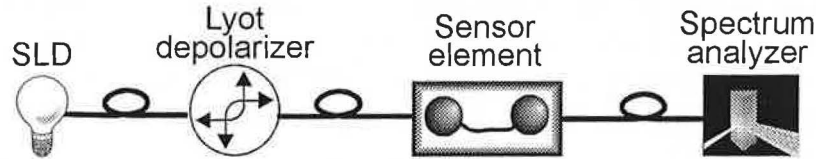

Fig. 4.2.4 Experimental set-up for the characterization of spectral properties of the sensor sample element in depolarized light.

As a model analyzed media, water-diethyleneglycol mixtures were used. Its refractive indices were measured by an Abbe refractometer at a wavelength of $\lambda=589$ nm. The dispersion properties have been accounted for using the following model:

$$n(\lambda) = \frac{n_w(\lambda) - n_d(\lambda)}{n_w(\lambda_D) - n_d(\lambda_D)} \cdot \left(n(\lambda_D) - n_d(\lambda_D)\right) + n_d(\lambda), \tag{4.2.3}$$

where $\lambda_D=589$ nm is the wavelength at which the refractive indices was measured by the Abbe refractometer, n_w is the refractive index of water, and n_d is the refractive index of diethyleneglycol. In this model it is supposed that both the mixture components contribute to the refractive index of the mixture with its refractive indices in a ratio corresponding to its fraction in the mixture. The following dispersion relationship of diethyleneglycol in the infrared region was measured by the critical angle method using a tunable Ti:sapphire laser as the source, the wavelength λ is in [nm]:

$$n(\lambda) = 1.811 - 8.40 \times 10^{-4} \lambda + 4.601 \times 10^{-7} \lambda^2. \tag{4.2.4}$$

The dispersion relationship of water was taken from [96]. In the following analysis the refractive indices of the model analyzed media are for $\lambda=825$ nm.

Results

Using the set-up in Fig. 4.2.4, ten prepared samples were characterized using the model analyzed media with various refractive indices. The typical performance is shown in Fig. 4.2.5 (sample Bolaso 35). There were, however, three samples, which exhibited different behavior. The difference can be seen comparing Fig. 4.2.5 with Fig. 4.2.6 (sample Bolaso 38). In Fig. 4.2.5, in contrast to Fig. 4.2.6, the depth of the SPR dips is nearly independent of the dip spectral position and the spectral position of the SPR dips corresponding to the same refractive index of the analyzed medium is shifted by about 10 nm (measured for $n_{medium}=1.3956$). The deposited gold film is not responsible for any difference, as the two samples were coated together in one evaporation cycle. The same difference was observed also for samples Bolaso 31 and 37 with a slightly different gold film thickness (60 nm) which were also coated in the same cycle. In order to explain the observed difference, the samples were studied more thoroughly.
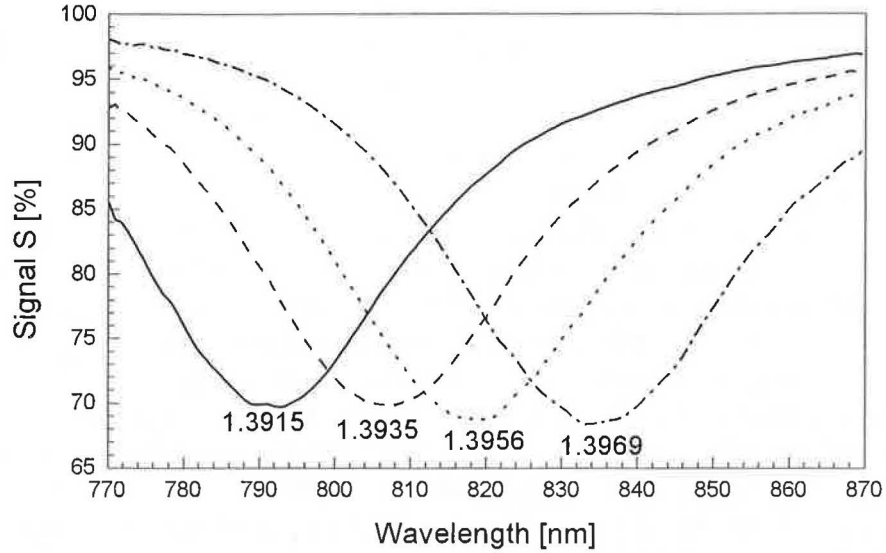
46

Fig. 4.2.5. The signal S as a function of wavelength for various n_{medium} for Bolaso 35 with a 65 nm thin gold film in the set-up shown in Fig. 4.2.4.
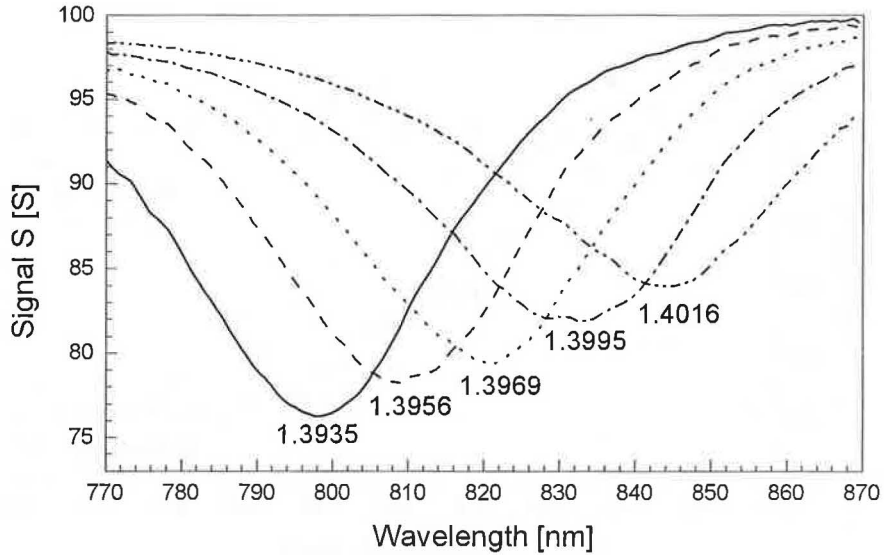

Fig. 4.2.6. The signal S as a function of wavelength for various n_{medium} for Bolaso 38 with a 65 nm thin gold film in the set-up shown in Fig. 4.2.4.

The detailed study consisted of using the set-ups shown in Fig. 4.2.2 and Fig. 4.2.3. The SPR dip shallowing should be understood by observing Fig. 4.2.7 and Fig. 4.2.8 together with (3.4.1). Fig. 4.2.7 shows the comparison of TM transmitted relative power of the two different samples (Bolasos 35 and 38) when the SPW in not excited ($n_{medium}=1$) using the set-up from Fig. 4.2.3. For each wavelength the measured TM and reference TE polarizations are adjusted by the polarization controller. Fig. 4.2.8 shows the relative transmitted power for sample Bolaso 38 in and off the SPR. As follows from Fig. 4.2.7 and Fig. 4.2.8, for Bolaso 38 (in contrast to Bolaso 35), the relative value of I^{TM} for longer wavelengths is smaller than I^{TE}, under SPR as well as off the SPR, which results in the SPR dip shallowing for longer wavelengths according to (3.4.1). For the shift of the detected SPR wavelength, the difference shown in Fig. 4.2.7 is also responsible. The actual SPR dip position for Bolaso 38 shown in Fig. 4.2.8 is

47

806 nm, which corresponds to the SPR dip position measured with Bolaso 35 (Fig. 4.2.5, n_{medium}=1.3956). In Fig. 4.2.9 is calculated the SPR dip minimum by (3.4.1) using data from Fig. 4.2.8. The resulted SPR dip position (799 nm) agrees well with the SPR dip position in Fig. 4.2.6. In this way it is clear that the difference in the SPR dip position in Fig. 4.2.5 and Fig. 4.2.6 originates in different attenuation of the TM mode off the SPR for the two samples. The reason of this difference is, however still not clear. It may be suggested that the different amount of the remaining cladding (parameter d_0) could be responsible for the difference according to Fig. 3.4.5. The agreement of Fig. 3.4.4 with Fig. 4.2.7 is, however, only qualitative. On the other hand, the reduction of d_0 should result in a shift in the SPR wavelength as follows from Fig. 3.4.3, which is, however, not confirmed by the experimental results. On the contrary, comparing the two SPR dips at a fixed wavelength (Fig. 4.1.9, the set-up in Fig. 4.2.2) confirms the d_0 should be responsible for the difference, as the decrease in d_0 leads also to the deepening of the SPR dip (Fig. 3.4.3). As the polished surface is not ideally flat, variations in the d_0 may cause that locally $d_0<0$ μm. As follows from [94], sensor element polished into the fiber core ($d_0<0$ μm) exhibits at a fixed wavelength out of the SPR much higher attenuation for the TM mode than for the TE mode. Therefore it is believed that the three similar samples perform locally $d_0<0 \mu m$ in contrast to the remaining seven samples.
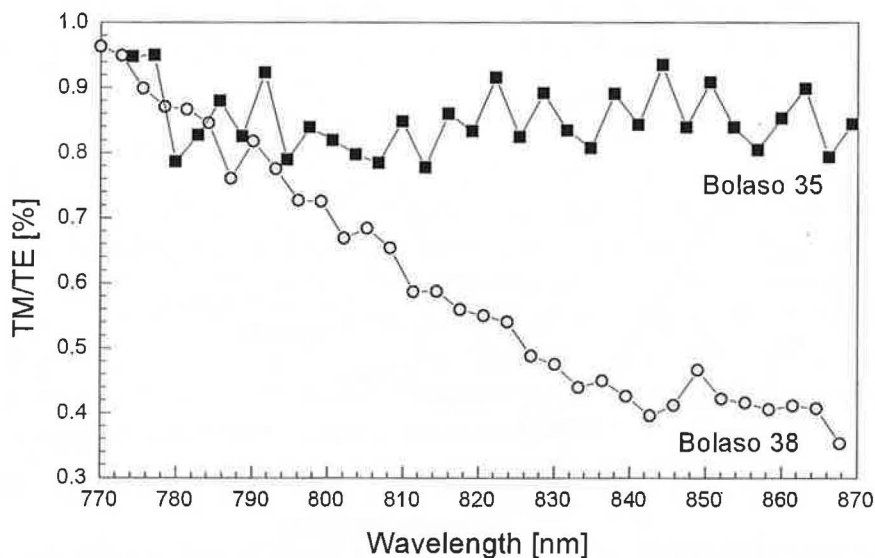

Fig. 4.2.7. Spectral TM mode relative output power of samples Bolaso 35 and 38 with a 65 nm thin gold film off the SPR (n_{medium}=1) using the set-up from Fig. 4.2.3. TE mode is used as a reference.

In the following analysis only samples which do not exhibit shallowing of the SPR dip for longer wavelengths are used (their behavior is very similar to that of Bolaso 35 - Fig. 4.2.5). For these samples d_0 is estimated to be $d_0 \approx 1$ μm. To study the influence of the gold film thickness on the SPR minimum shape, the SPR dips were measured using model analyzed media with different refractive indices (n_{medium}) in order to adjust all the dips to a similar wavelength position (Fig. 4.2.11). For absolute comparison of the SPR dips from Fig. 4.2.11, the set-up from Fig. 4.2.2 was used resulting in Fig. 4.2.12. There it is possible to observe deepening of the SPR dip and shift of the SPR dip position due to a decrease of the gold film thickness in accordance with the theoretical analysis (Fig. 3.4.2).
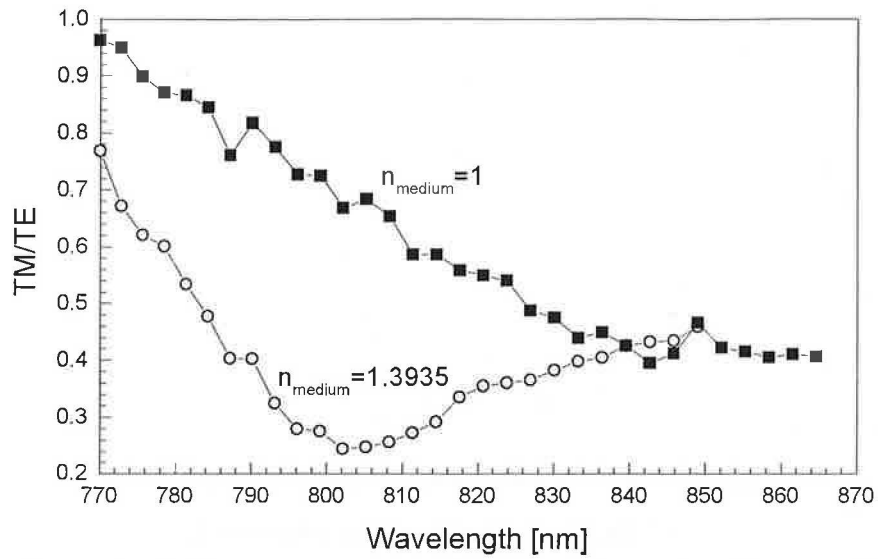
Fig. 4.2.8. Spectral relative output power of sample Bolaso 38 with a 65 nm thin gold film for TM polarization off the SPR ($n_{medium}=1$) and in SPR ($n_{medium}=1.3935$) using the set-up from Fig. 4.2.3. TE mode is used as a reference.
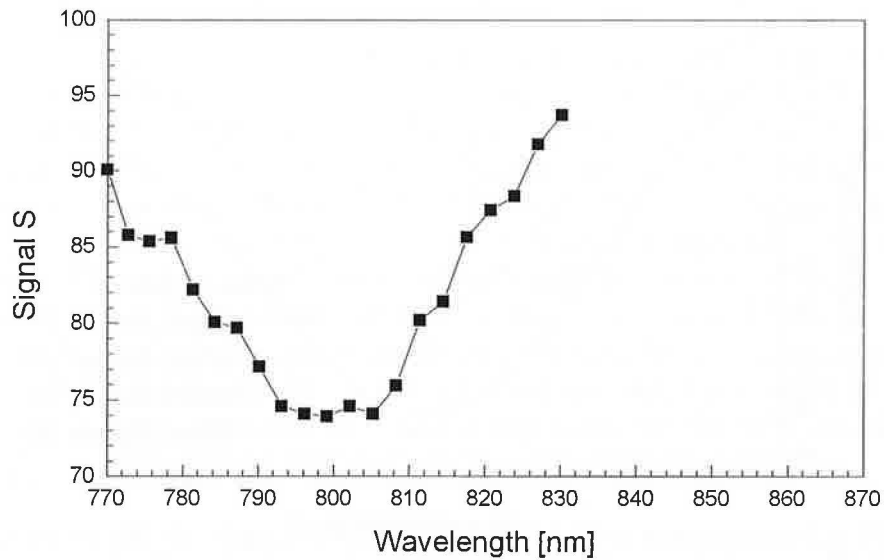

Fig. 4.2.9. Signal S measured with the sample Bolaso 38 with a 65 nm thin gold film calculated from (3.4.1) using data shown in Fig. 4.2.8.

From Fig. 4.2.11, narrowing and shallowing of the SPR dips induced by the increasing thickness of the gold film is seen. To compare the SPR dips more in detail, a method of data extraction has to be used.

49

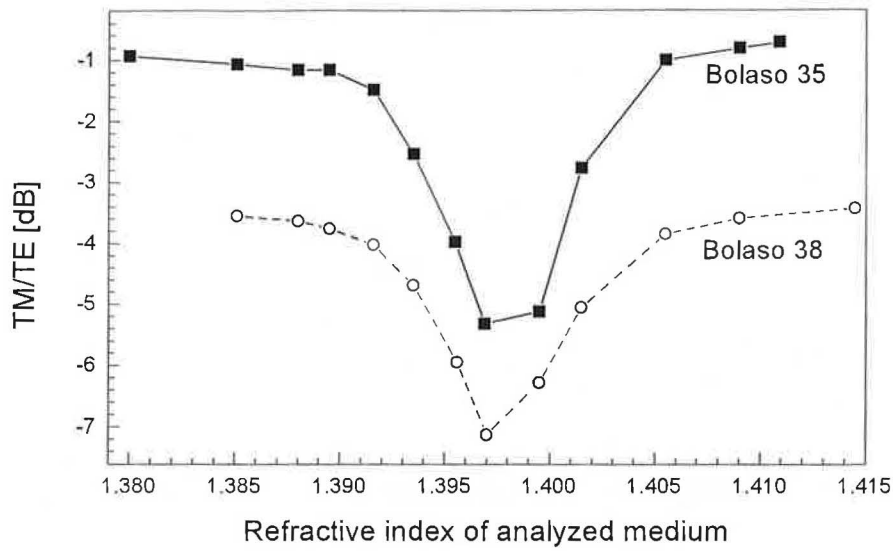**Fig. 4.2.10.** TM mode attenuation as a function of n_{medium} for sensor element samples Bolaso 35 and 38 with a 65 nm thin gold film in the set-up shown in Fig. 4.2.2. The TE mode is used as a reference; λ=825 nm.
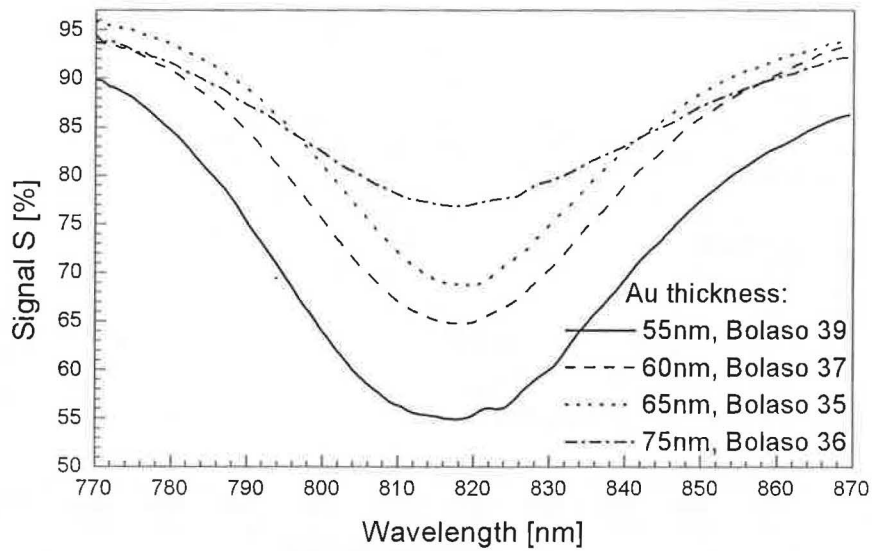

Fig. 4.2.11 The spectral response S of the SPR sensor elements in the set-up from Fig. 4.2.4 for various sensor element samples using different gold film thicknesses.
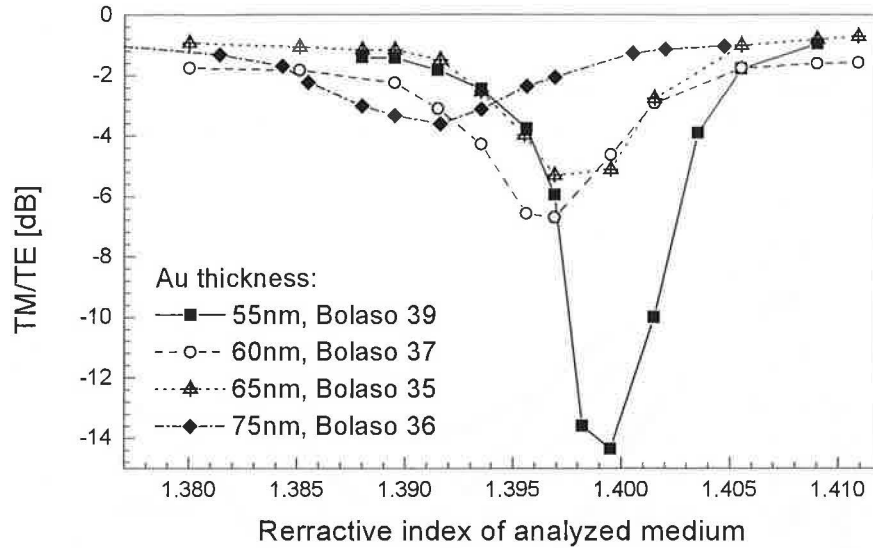
Fig. 4.2.12 The TM mode response of the sensor element in the set-up from Fig. 4.2.2 for various samples using different gold film thicknesses, λ=825 nm.

Analysis of SPR Spectra

The information that is of major interest in sensor applications is the position of the SPR dip, which corresponds to changes in the refractive index of the analyzed medium. To extract this information from the measured spectrum a fitting procedure could be used. The most popular is polynomial regression. The shape of SPR dip is, however, different from polynomial and only a limited part of the spectrum at the bottom of the SPR dip can be used for the polynomial regression. In our case this approach is not suitable as the obtained SPR response functions are shallow and the noise is relatively high (see, for example Fig. 4.1.7) in comparison with the response obtained from an ATR SPR coupler. In order to obtain the maximum signal to noise ratio, it is advantageous to use the entire SPR dip for the fit. The search for a suitable function resulted in a Lorentz function with a linear term (3.4.2), which compensate for the SPR dip slight non-symmetry.

The adequacy of the developed fitting function (3.4.2) is demonstrated in Fig. 4.2.13, where the data from Fig. 4.2.11 are fitted. The standard deviation *SD* is given as:

$$SD = \sqrt{\frac{1}{n-1}\sum_{i=1}^{n}\left(X_i - \overline{X}\right)^2}, \tag{4.2.1}$$

where *n* is the sample size and $\overline{X}$ is the mean. The fit standard deviation (4.2.1), fitted width *FWHM*, accuracy of the spectral position $\Delta\lambda$ of the Lorentz minimum, the depth *d* and the parameter *FWHM/d* of the minimum are shown in Table 4.2.1.

As was suggested in the theoretical analysis, the minimum in the parameter *FWHM/d* should correspond to the most suitable SPR dip. Table 4.2.1 suggests that the gold film thickness 60-65 nm should be the best choice from this point of view. It corresponds to the theoretically predicted values, assuming $d_0 \approx 1$ μm. The experimentally achieved sensitivity was evaluated using data from Fig. 4.2.5 fitted by the function (3.4.2). This value, which is of about 7900 dB/RIU, is in good agreement with the theoretically predicted value of 7600 dB/RIU. The experimentally achieved SPR width and depth

51

(Table 4.2.1) are comparable with the theoretically predicted values (obtained fitting data from Fig. 3.4.6 by (3.4.2). Observing the experimentally obtained trend of *FWHM/d* increase for the gold film thickness over 65 nm (Table 4.2.1) with the theoretical values (Fig. 3.4.7), it may be confirmed that the realized samples have $d_0 \approx 1$ µm.
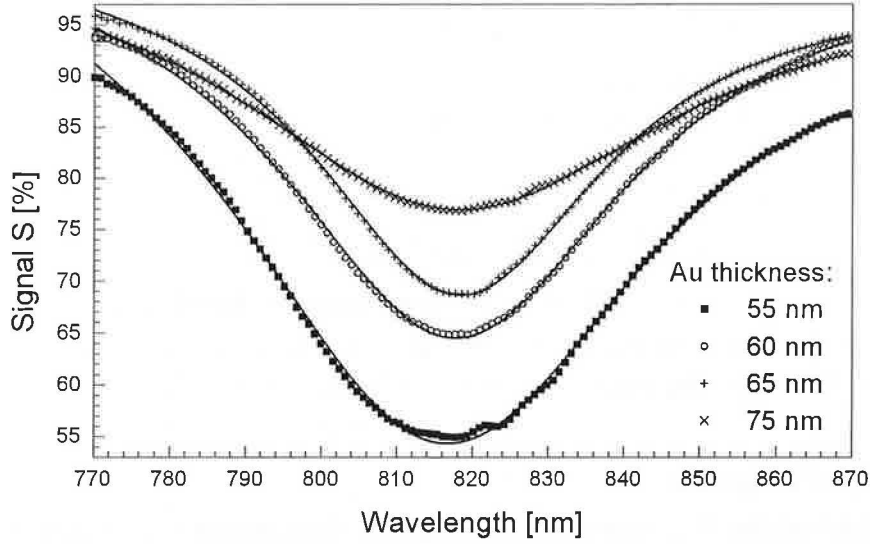

Fig. 4.2.13 The spectral response *S* of the SPR element in the set-up from Fig. 4.2.4 for various sensor element samples using different gold film thicknesses (symbols) and fitted by function (3.4.2) (lines).

Table 4.2.1 The fitted parameters

Sample	Bolaso 39	Bolaso 37	Bolaso 35	Bolaso 36
Standard deviation $SD \times 10^{-3}$	1,8	0.7	0.4	0.2
Thickness h_{Au} [nm]	55	60	65	75
FWHM [nm]	70	57	48	71
Accuracy $\Delta\lambda$ [nm]	0.1	0.06	0.05	0.08
depth *d* [%]	41	31	27	19
FWHM/d [nm]	170	185	180	385

4.3 Sensor System Analysis

The light from the SLD is depolarized by the Lyot depolarizer and then it passes through the sensor element (Fig. 4.3.1). After passing the sensor element the signal is similar to that shown in Fig. 4.3.2. This response was calculated in the following way. Let us describe the SLD as a partially, along the *x*-axis linearly polarized source with totally coherent (and thus also polarized [97]) and totally non-coherent (let us suppose this part is totally non-polarized) part. As follows from (4.1.1), the polarized electric field intensity is described as:

$$\begin{pmatrix} E_x \\ E_y \end{pmatrix}^P = \begin{pmatrix} \sqrt{\sum_{i=1}^{3} \frac{A_i}{w_i \sqrt{\pi/2}} \exp\left(\frac{-2(\lambda - \lambda_i)^2}{w_i^2} \right)} \\ 0 \end{pmatrix} \tag{4.3.1}$$

and the non-polarized electric field intensity:

$$\left(E_x\right)^N = \left(E_y\right)^N = \frac{1}{2}\sqrt{\sum_{i=4}^{5}\frac{A_i}{w_i\sqrt{\pi/2}}\exp\left(\frac{-2(\lambda-\lambda_i)^2}{w_i^2}\right)}, \qquad (4.3.2)$$

where all the used parameters are in Table 4.1.1. Each element of the Lyot depolarizer (a piece of a HiBi fiber) is described by the Jones matrix:

$$\hat{J}(\varphi_i) = \begin{pmatrix} e^{-i\varphi_i} & 0 \\ 0 & 1 \end{pmatrix}, i = 1, \ 2, \qquad (4.3.3)$$

where φ_i is given by (4.1.4), index i corresponds to the i-th birefringent element. Supposing the first element of the Lyot depolarizer is rotated with respect to the SLD polarization state by an angle α and that between the Lyot elements there is an angle of $\pi/4$, the responses of the system from Fig. 4.3.1 for totally polarized and for totally non-polarized part are as follows:

$$\begin{pmatrix} E'_x \\ E'_y \end{pmatrix}^P = \hat{M}(-\beta)\cdot\hat{K}\cdot\hat{M}(\beta)\cdot\hat{M}\left(-\alpha-\frac{\pi}{4}\right)\cdot\hat{J}(\varphi_2)\cdot\hat{M}\left(\frac{\pi}{4}\right)\cdot\hat{J}(\varphi_1)\cdot\hat{M}(\alpha)\cdot\begin{pmatrix} E_x \\ E_y \end{pmatrix}^P \qquad (4.3.4)$$

and

$$\begin{pmatrix} E'_x \\ E'_y \end{pmatrix}^N = \hat{M}(-\beta)\cdot\hat{K}\cdot\hat{M}(\beta)\cdot\begin{pmatrix} E_x \\ E_y \end{pmatrix}^N, \qquad (4.3.5)$$

where $\hat{M}(\alpha)$ is a rotation matrix (α is the angle of rotation) defined as:

$$\hat{M}(\alpha) = \begin{pmatrix} \cos\alpha & -\sin\alpha \\ \sin\alpha & \cos\alpha \end{pmatrix} \qquad (4.3.6)$$

and $\hat{K}$ is the Jones matrix of the sensor element:

$$\hat{K} = \begin{pmatrix} 1 & 0 \\ 0 & f\cdot e^{-i\phi} \end{pmatrix}. \qquad (4.3.7)$$

$\hat{K}$ is in coordinates perpendicular and parallel to the metal film, so f is the transmissivity of the element for TM polarized light wave and ϕ is phase retardation between the TM and TE polarized light waves. β is the angle of rotation of the sensor element with respect to the SLD. The attenuation of the TE polarization is neglected. In order to determine f and ϕ, a sensor element with the following model parameters: h_{Au}=65 nm and d_0=0 μm is taken into account. The TM polarization sensor element response out of SPR (for n_{medium}=1, Fig. 3.4.5) is fitted by a linear function:

$$f = 1.06 - 2.2\times10^{-4}\lambda \qquad (4.3.8)$$

and the response corresponding to the SPR (for n_{medium}=1.3934, Fig. 3.4.3) by the modified Lorentz function (3.4.2):

$$f = 1.456 - 6.4\times10^{-4}\lambda - \frac{180}{\pi}\cdot\frac{79}{4(\lambda-828.6)^2+79^2}. \qquad (4.3.9)$$

The phase shift under SPR is fitted by the derivative of the Lorentz function modified by a linear term (Fig. 3.4.8):

$$\phi = 1.35 + 3.0 \times 10^{-3} + 1.54 \frac{(\lambda - 829) \cdot 52}{4(\lambda - 829)^2 + 52^2},$$ (4.3.10)

where the wavelength λ is in nanometers and the phase shift ϕ in radians.

The spectral power density for a given wavelength at the output (Fig. 4.3.2) is then given as a sum of intensities in both polarizations of totally polarized and totally non-polarized signals:

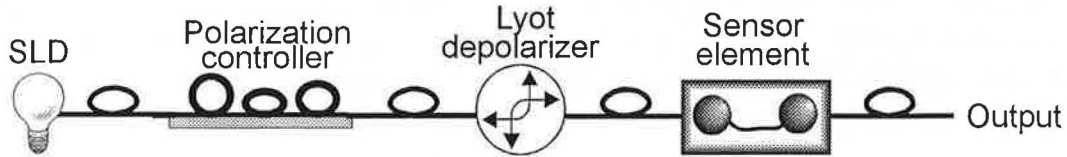$$I = \left(|E'_x|^2 + |E'_y|^2 \right)^P + \left(|E'_x|^2 + |E'_y|^2 \right)^N.$$ (4.3.11)

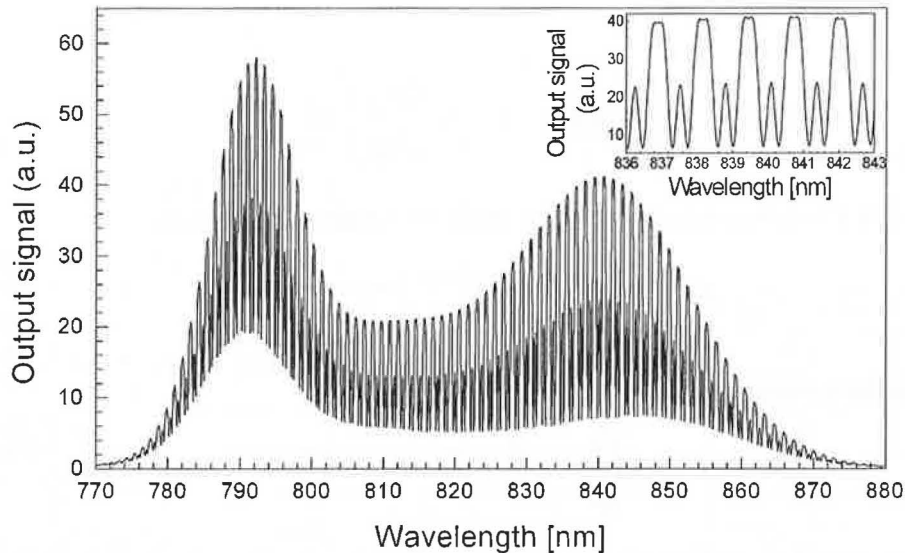**Fig. 4.3.1** A part of the sensor set-up.

Fig. 4.3.2 Calculated typical output signal obtained in the set-up shown in Fig. 4.3.1.

The output signal of the system in Fig. 4.3.1 is partially polarized, which is a consequence of polarization dependent losses in the sensor element. As the performance of the used spectrum analyzer is also polarization dependent, twisting or bending of the sample output fiber can cause changes in the polarization state of the guided mode [70] and thus affects also information coming from the spectrum analyzer. This can affect the SPR dip and consequently also the position of the fitted SPR minimum. As can be concluded from [83] it might be very difficult to depolarize a signal with complicated spectral shape by a Lyot depolarizer. This is the reason why a multimode fiber mode mixer is used at the sample output, where the signal has rather complicated spectrum (Fig. 4.3.2). This device should be capable of efficient depolarization of the signal produced by the system in Fig. 4.3.1. Here we assume that the mode mixer together with the spectrum analyzer form a polarization and phase insensitive device so that the signal given by (4.3.11) is not further affected. Taking the Gaussian response function of the spectrum analyzer with w=3.5 nm (Fig. 4.1.9), the signal received by a

photodiode which collects light in a spectral interval $\langle \lambda - \Delta\lambda, \lambda + \Delta\lambda \rangle$ in the spectrum analyzer photodiode array is:

$$I^\lambda = \frac{1}{2\Delta\lambda} \int_{\lambda-\Delta\lambda}^{\lambda+\Delta\lambda} \frac{1}{w\sqrt{\pi/2}} \int e^{-2\left(\frac{\overline{\lambda}-\lambda}{w}\right)^2} I \, d\overline{\lambda} d\lambda ,$$

(4.3.12)

where $2\Delta\lambda$ is the distance between pixels on the diode array. This equation represents the convolution of the signal coming from the output fiber with the response function of the spectrum analyzer and averaging over the spectral width covered by an element of the spectrum analyzer diode array detector. The expected output signal of the sensor system (Fig. 4.3.3) calculated from (4.3.12) for above-announced parameters of the sensor components is shown in Fig. 4.3.4. In Fig. 4.3.4 there is also shown the reference spectrum obtained by using f from (4.3.8) and $\phi=0$ rad, which is the case corresponding to $n_{medium}=1$. Varying the angles α and β, there were no changes of the results exceeding numerical error of the calculations. The division of the signal by the reference shown in Fig. 4.3.4 is the response S, which is shown together with its fit (3.4.2) in Fig. 4.3.5. The shape parameters of the fit slightly differ from the parameters of the sensor element response (4.3.9):

$$S = 1.197 - 0.0241\lambda - \frac{92}{\pi} \cdot \frac{78.1}{4(\lambda - 828.83)^2 + 78.1^2} .$$
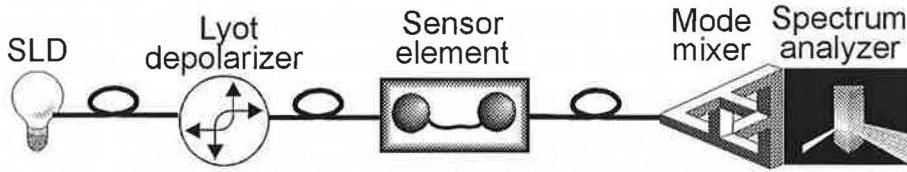
(4.3.13)

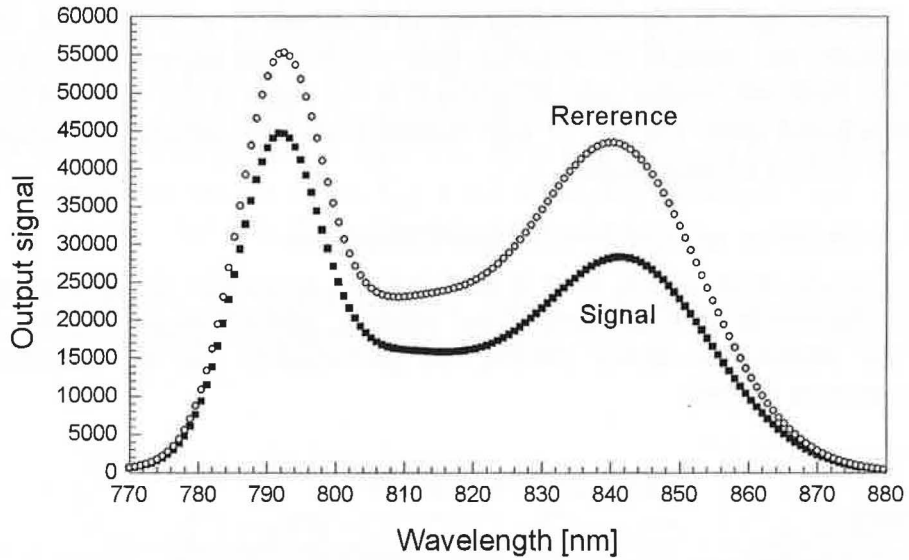**Fig. 4.3.3** Sensor system set-up.

Fig. 4.3.4 Sensor system response when SPR occurs, $n_{medium}=1.3934$ (Signal) and $n_{medium}=1$ (Reference) in the set-up from Fig. 4.3.3. Each dot corresponds to one diode element in the detector diode array.
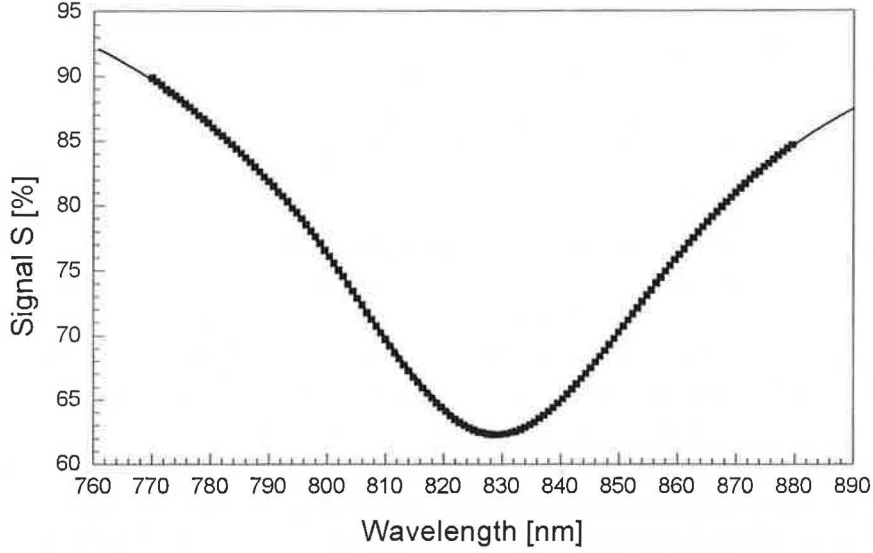
Fig. 4.3.5 Sensor SPR response for n_{medium}=1.3934 calculated from Fig. 4.3.4 dividing the Signal by the Reference. Each dot corresponds to one diode element in the detector diode array; the line corresponds to the fit by the modified Lorentz function (3.4.2).

System Limitations

Resolution of the sensor system is limited, by residual polarization of light in the system and by the accuracy of the used data extraction method. The residual polarization of light is caused by imperfection of the Lyot depolarizer and by the sensing element. Bending and twisting of the sensor element input fiber spectrally changes the polarization state of the residually polarized light [98,99], and causes changes in the detected SPR minimum. This effect is in detail described below. The residual polarization influences also the reference spectrum because of the different spectral attenuation of the TE and TM modes (Fig. 3.4.4 and Fig. 3.4.5). As the reference spectrum is measured only once, it does not influence the sensor system performance because only changes in the position of the SPR minimum are of interest. Beside the sensor element, the residual polarization may originate in imperfection of the mode mixer. This, however, causes only an increase in the noise of the detected SPR dip, as can be concluded from Fig. 4.1.7, and therefore may be reduced by employing an appropriate method of data analysis.

Residual Polarization of Light from the Lyot Depolarizer

A standard single-mode optical fiber is modeled by a zero-order phase retarder with the retardation dependent on fiber bending and twisting, which induces fiber birefringence through the elasto-optic effect [98,99]. Its performance can be described in the following manner [98,99]:

$$\begin{pmatrix} E_x \\ E_y \end{pmatrix}^{PP} = \hat{M}(-\gamma) \cdot \hat{L}(\Delta\varphi) \cdot \hat{M}(\gamma) \cdot \begin{pmatrix} E_x \\ E_y \end{pmatrix}^{P}, \tag{4.3.14}$$

where $\hat{L}(\Delta\varphi)$ is the Jones matrix of the phase retardation $\Delta\varphi$ ($\Delta\varphi < 2\pi$ corresponds to a zero-order behavior):

56

$$\hat{L}(\theta) = \begin{pmatrix} \exp(-i\Delta\varphi \dfrac{\lambda_0}{\lambda}) & 0 \\ 0 & 1 \end{pmatrix}, \tag{4.3.15}$$

the index PP denotes the signal originating in the polarized part of the SLD spectrum which was not depolarized by the Lyot depolarizer, and γ is an angle of rotation of the fiber mode polarization caused e. g., by a fiber bending.

Now we are able to derive the spectral light intensity at the sensor element output as a sum of the originally non-polarized light (4.3.5), light depolarized by the Lyot depolarizer (4.3.4) and residually polarized light given as:

$$\begin{pmatrix} E'_x \\ E'_y \end{pmatrix}^{PP} = \hat{M}(-\beta) \cdot \hat{K} \cdot \hat{M}(\beta) \cdot \begin{pmatrix} E_x \\ E_y \end{pmatrix}^{PP}, \tag{4.3.16}$$

which is:

$$I = P \cdot \left(|E'_x|^2 + |E'_y|^2 \right)^{PP} + (1-P)\left(|E'_x|^2 + |E'_y|^2 \right)^{P} + \left(|E'_x|^2 + |E'_y|^2 \right)^{N}. \tag{4.3.17}$$

The used Lyot depolarizer exhibits $P < 0.012$. The response of the spectrum analyzer is then calculated using (4.3.12) with I from (4.3.17). Changing the parameters α, β, γ, $\Delta\varphi$ in an interval $(0, 2\pi)$, dividing the result by the reference spectrum (Fig. 4.3.4) and fitting the resulted SPR minimum, it was found that for $P=0.012$ the residual polarization changes the position of the SPR minimum by up to 0.09 nm.

4.4 Realization and Testing of the Sensor System

The sensor system was built according to Fig. 4.3.3. To verify the independence of the sensor performance on the fiber bending, two polarization controllers were utilized, Fig. 4.4.1. The first one is placed at the input fiber of the sensor element and the other at the output fiber of the sensor element. In order to monitor in situ the evolution of the SPR minimum, the software developed in C language based on the Lorenz function fitting procedure (3.4.2) by Petr Tobiška was used. The applied delivery system for the media under study is depicted in Fig. 4.4.2. The flow cell had cylindrical shape, its depth was of about 1 mm and it had volume approximately of 40 μl. The plastic input/output tubes had inner diameters of about 0.5 mm. The flow was induced by a level difference between the reservoir and the waste, Fig. 4.4.2. Changing the level of the reservoir, the flow was controlled. The flow ranged from 0 to 0.2 ml/min.

In order to evaluate the sensor system, simple refractometric measurement was performed first. Then the capability of the sensor to work as a biosensor was proven by a model immunodetection.
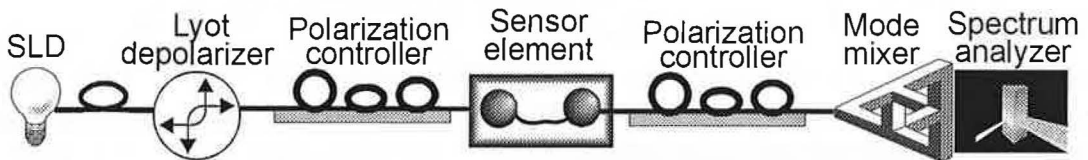

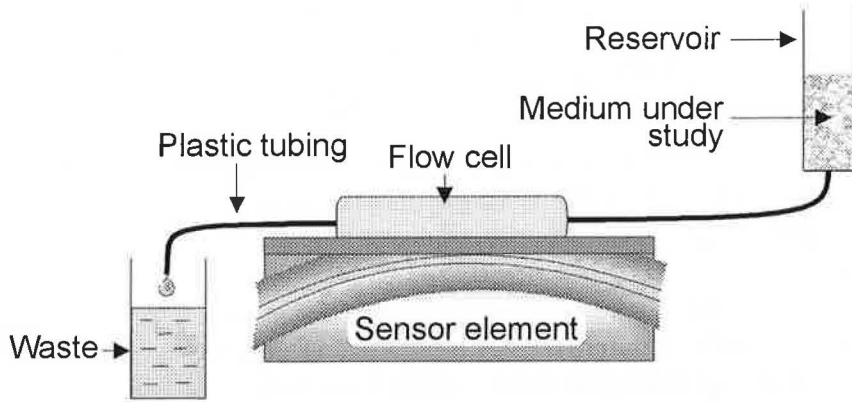**Fig. 4.4.1** Experimental set-up for the sensor system characterization.

Fig. 4.4.2 Delivery system for the media under study.

Refractometric measurement

As the sensor element surface was not stable in water environment, which was indicated by drift in the detected SPR dip wavelength, a chemo-optical transducer described below was deposited on the sensor element surface first. This procedure resulted in stable sensor surface. Then, the flow cell was soaked with the model media under study with known refractive indices as shown in Fig. 4.4.3. During this experiment, no movement of the polarization controllers was performed. From Fig. 4.4.3 it can be seen that the sensor behavior is reproducible and the sensitivity was calculated to be 3100 nm/RIU, which agrees well with the theoretical prediction. To evaluate the resolution of the sensor, another experiment was made. In this experiment, the positions of the coils of the input and output polarization controllers were changed in order to reproducibly simulate fiber bending. The result of this experiment is depicted in Fig. 4.4.4. The SPR dips, which correspond to the most different positions of the SPR minims, are shown in Fig. 4.4.5.
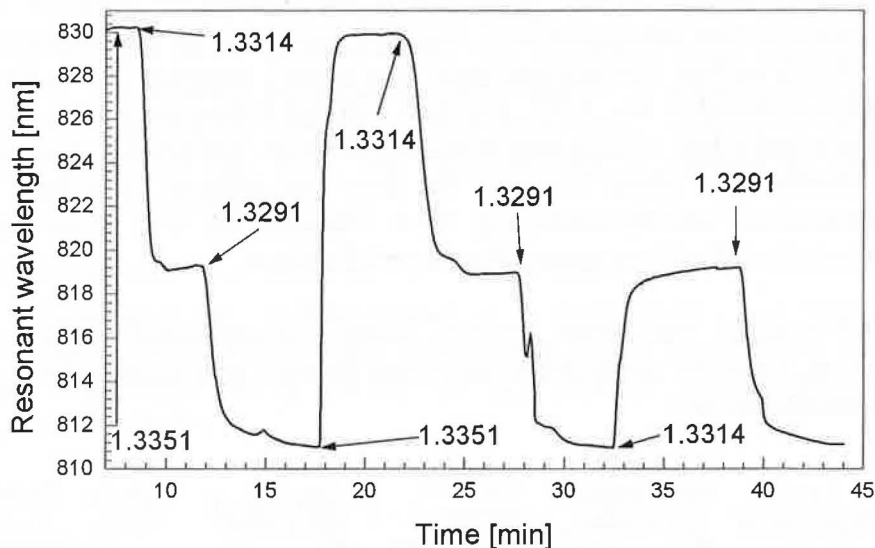

Fig. 4.4.3 Refractometirc measurement. The flow cell was soaked with the model media under study with different refractive indices.

On the basis of inspection of Fig. 4.4.4, two modes of operation of the sensor system were suggested. In the first one, the input and output sensor element fibers movement is

not allowed, so the displacement of the sensor element is not possible – the *static mode* of operation. In another mode of operation, the displacement of the sensor element and thus also movement (bending) of the input and output fibers is allowed – the *dynamic mode* of operation. In the static mode of operation, the calculated resolution of the sensor is of 1.5×10^{-3} nm. The resolution was determined as the standard deviation (4.2.1) of the curve from Fig. 4.4.4 using the time period ranging from 29.5 min to 31 min. For the dynamic mode of operation the uncertainty in determination of the resonant wavelength resolution increases up to 9×10^{-2} nm.

Fig. 4.4.4 Bolaso 35 sample with a 60 nm gold film, 20 nm tantalum pentoxide overlayer and the chemo-optical transducer with water as the model medium under study. The steps on the curve correspond to variations of the used polarization controllers.
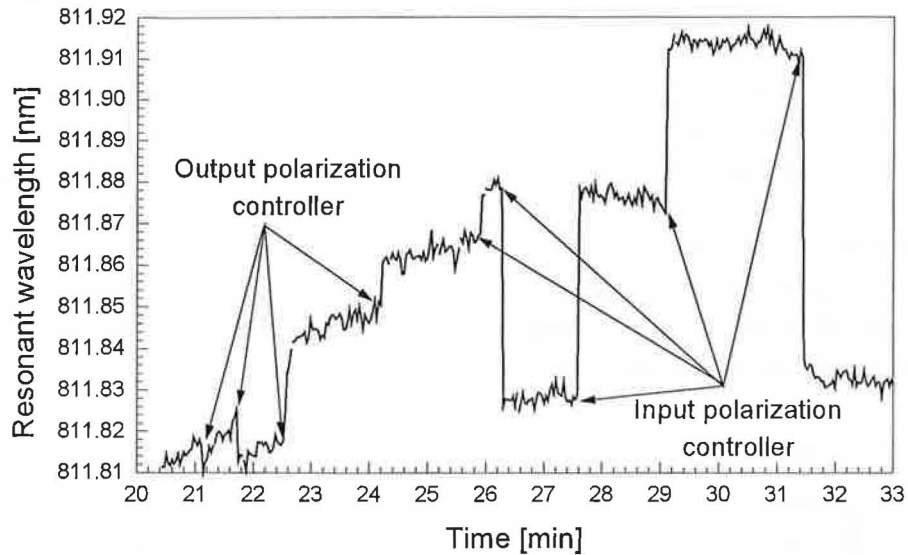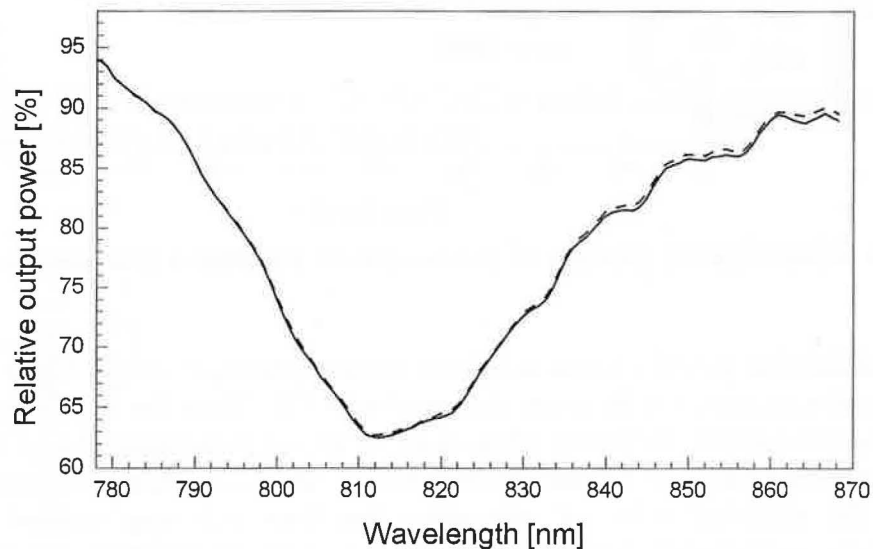

Fig. 4.4.5 Bolaso 35 sample with a 60 nm gold film, 20 nm tantalum pentoxide overlayer and the chemo-optical transducer with water as the model medium under study. The sensor system responses which correspond to maximum (time 30 min) and minimum (time 32 min) SPR wavelengths in Fig. 4.4.4 are shown.

59

Immunodetection

In order to prove the potential of the built SPR fiber optic sensor system for biosensing, a model bio-experiment in which model analyte was detected by means of the sensor functionalized with respective antibodies was carried out.

Reagents

Human immunoglobulin (IgG), monoclonal antibody against IgG (a-IgG) were obtained from Seva Immuno, Prague; dextran sulfate sodium salt (DS), average molecular weight of approximately 5000, and bovine serum albumin (BSA), purity better than 99 percent by agrose electrophoresis, were purchased from Sigma. Glutaraldehyde (GA) was freshly vacuum—distilled at 20 kPa under nitrogen into water to form a stock solution containing 20 percent of GA. Solutions were prepared using citrate buffer (CB), 0.1 M, pH of 3.96 and phosphate buffered saline (PBS), pH of 7.26. Molecular weights of the used reagents were as follows: 1.5×10^5 for IgG and a-IgG, and 6.5×10^4 for BSA.

Chemo-Optical Transducer

For specific detection of IgG, network of the respective nomoclonal antibodies (a-IgG) was immobilized on the sensor element surface by covalent crosslinking of two a-IgG molecular layers prepared using the consecutive adsorption [100].
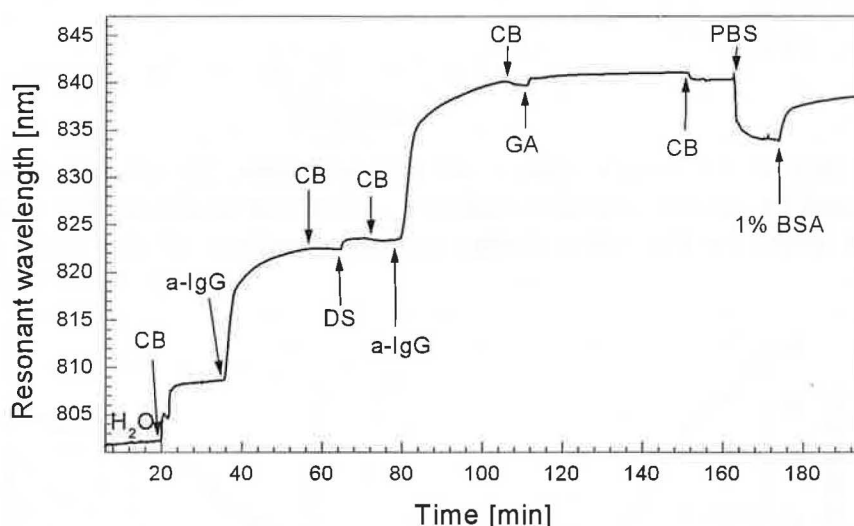
Fig. 4.4.6 Immobilization process of chemo-optical transducer (two monolayers of a-IgG).

The immobilization procedure was as follows (sensorgram is shown in Fig. 4.4.6). First, the flow cell was soaked with water followed with CB. Then the flow cell was filled with a-IgG (100 µg/ml) containing CB in order to form a monolayer of a-IgG molecules on the tantalum pentoxide surface, mainly due to the hydrophobic interaction. After attaining the saturated value of adsorption the flow cell was washed with CB. Subsequently, consecutive adsorption of DS was realized injecting solution of DS (1 mg/ml) in CB into the flow cell. After saturation, the flow cell was washed again with CB. Then, the flow cell was again filled with a-IgG containing CB, and the second molecular layer of a-IgG was formed due to electrostatic interaction between DS polyanions and the positively charged a-IgG proteins below their isolelectric point. After saturation, the flow cell was washed with CB again. Then, GA was injected into the flow cell and covalent crosslinking of the adsorbed a-IgG was performed using GA

(0.2 percent in CB). After washing with CB, the PBS solution was injected, which leads to washing out DS molecules of the a-IgG network by reverting the a-IgG protein charge in PBS.

Sensor Response

Injecting the PBS and consequently BSA (1 percent in PBS) solutions (Fig. 4.4.6), it was found that the resulting network of the a-IgG on the sensor surface was stable. The response of the sensor with the a-IgG network to IgG molecules was measured while flowing through the cell BSA (1 percent in PBS) solutions containing increasing IgG concentrations (Fig. 4.4.7). The concentration isotherm is shown in Fig. 4.4.8. The concentration of 40 ng/ml of IgG caused a shift in the resonant wavelength of 0.05 nm. Interpolating the concentration isotherm in Fig. 4.4.8 and considering the sensor resolution, it can be concluded that the ultimate sensor resolution is 1 ng/ml for the static mode of operation and 90 ng/ml for the dynamic mode of operation. For high IgG concentration starting saturation in the sensor response is observed (Fig. 4.4.8).
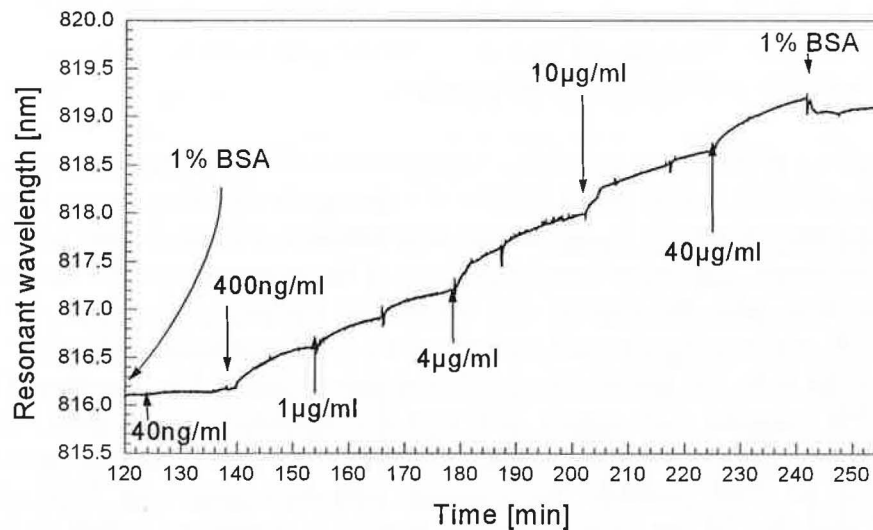

Fig. 4.4.7 Model immunoreaction. The flow cell is soaked with increasing concentration of IgG in the solution of 1 percent BSA in PBS.
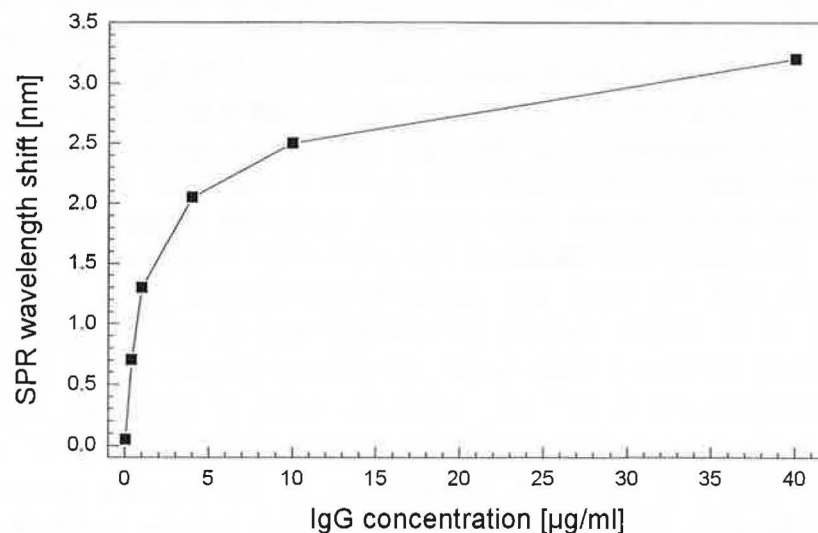

Fig. 4.4.8 Sensor response to IgG molecules (concentration isotherm).

61

5. Conclusions

5.1 Results

An all-fiber-optic biosensor based on surface plasmon resonance (SPR) has been designed, built and tested.

The sensor element structure was analyzed theoretically by the beam expansion and propagation method (BEM) and optimal parameters were designed. For amount of the remaining fiber cladding corresponding to $d_0 \approx 1$ μm, the optimal thickness of the SPW supporting gold film was found to be of 55-65 nm. The thickness of the tantalum pentoxide overlayer, which allows adjustment of the operation range of the sensor towards aqueous environment, is 20 nm. The theoretically predicted sensitivity to changes in the refractive index of the analyzed medium was found to be almost independent of the gold film thickness and also on the amount of the remaining fiber cladding (i.e. of d_0). The sensitivity was determined to be 7600 nm/RIU (*Refractive Index Unit*) for the structure without an overlayer and 3100 nm/RIU for the structure with a 20 nm thick tantalum pentoxide overlayer.

The technology of fiber side-polishing was customized in order to prepare samples with required parameters and to attain sufficient reproducibility. The sensor elements were then studied experimentally using various experimental set-ups, which were built in the frame of this thesis. The experimental analysis of the prepared samples resulted in rather good agreement with the carried out theoretical analysis. The shape of the sensor element SPR response agrees well with the theoretical predictions, if uncertainty in the experimentally achieved parameter d_0 is taken into account. The position of the sensor element SPR response also agrees well with the theoretical predictions including the tuning effect of the tantalum pentoxide overlayer. The sensor element sensitivity was measured to be 7900 nm/RIU for samples with bare gold and 3100 nm/RIU for structures with the 20 nm thick tantalum pentoxide overlayer, which is in excellent agreement with the theoretical predictions.

Theoretical analysis of the sensor system was carried out in order to estimate sensor limitations. It was estimated that the residual polarization of light from the Lyot depolarizer might influence the detected position of the SPR dip by less then 0.09 nm. The tests of the sensor system were performed by a simple refractometric measurement. The influence of disturbances of the input and output sensor element fibers (their bending) on the stability of the system was studied. It was found that disturbances of the input and output sensor element fibers caused considerable changes in the detected SPR dip position. As a result, two modes of operation of the sensor were suggested – static (no movement with the input and output sensor element fibers and thus also no displacement of the sensor element are allowed) and dynamic (displacement of the sensor element is allowed). It leads to the resolution of the system of 1.5×10^{-3} nm (static mode of operation) and 9×10^{-2} nm (dynamic mode of operation), respectively. It corresponds to the sensor refractive index resolutions of 5×10^{-7} and 3×10^{-5} for the static and dynamic modes of operation, respectively, all for aqueous environment. The resolution for the static mode of operation is comparable with the best bulk optics-based SPR sensors. The resolution for the dynamic mode of operation is considerably smaller, but still better than that of the other fiber optic SPR sensors.

The capability of the sensor to work as a biosensor was demonstrated on an a-IgG – IgG immunoreaction monitoring. It was found that the ultimate concentration of IgG which was possible to detect by the sensor was 1 ng/ml in the static mode of operation and 90 ng/ml in the dynamic mode of operation, respectively.

The results of the theoretical analysis of the sensor element together with its experimental verifications were published in several original papers in scientific journals and presented at international conferences during the preparation of this thesis [101.102,103]. To the author's knowledge, the capability of the sensor elements based on single-mode optical fibers to work in sensor systems for immunoreaction monitoring was also for the first time published during the preparation of the thesis [104]. Technology for preparation of highly miniaturized sensor elements which were 1 cm long and only 0.6 mm in diameter and which used only a single fiber for delivery and collection of light wave to and from the sensor element, was also developed [105].

5.2   Further Improvements

In order to meet commercial requirements, two basic improvements have to be made. The more important of them is the requirement of multiplexing, which allows at least compensation for changes in the sensor system, which are not related to the event being sensed (changes in temperature, source spectrum, changes in the transducer which are not caused by analyte, etc.). Moreover, the multiplexing may allow multicomponent sensing. Achievable miniaturization of the sensor element together with packing more sensor elements together can help in attaining this goal. The second one is the requirement of higher sensor resolution, which may allow the detection of lower analyte concentrations or analytes with smaller molecules. It can be attained by suppressing the residually polarized light passing through the system, by improving the data analysis, by reducing the noise originating in the multimode fiber mode mixer, and by narrowing the SPR dips. The amount of the residually polarized light can be reduced by preparing a Lyot depolarizer with better performance, which is now becoming available or by employing an additional depolarization element, such as a polarization scrambler. The data analysis can be improved by using a more sophisticated fitting procedure. The employment of a more sophisticated method of mode mixing could reduce the noise caused by the multimode fiber mode mixer. The SPR dips could be in principle narrowed by the excitation of the so-called long-range surface plasma waves, which may exist in more complex mutilayered structures. Narrowing SPR dips may enable development of multichannel sensing structures in which two sensing channels with SPR dips located at slightly different wavelengths may be interrogated using a single optical system.

References

[1] K. T. V Grattan, A. W. Palmer, and D. P. S. Saini, Frustrated-Total-Internal-Reflection Fiber-Optic Pressure Sensor, IEEE J. Lightwave Technology, LT-3 (1985) 1130-1134.

[2] M. Croke, A. D. Kersey, D. A. Jackson, and J. D. C. Jones, All Fiber Michelson Thermometer, Electronics Letters, 19 (1983) 471-473.

[3] H. Nishihara, J. Koyma, N. Hoki, F. Kajaya, M. Hironaga, and M. Kauo, Optical Fiber Laser Doppler Velocimeter for High Resolution Measurement of Pulsatile Blood Flow, Applied Optics, 21 (1982) 1785-1790.

[4] M. Martinelli, A. Cesarani, and M. Polini, fiber Optic Vibrometer, Proc. 2nd Int. Conf. Optical Fiber Sensors, Stuttgart (1984) 403-414.

[5] B. Moslehi, M. W. Foster, and P. Harvey, Optical Magnetic and Electric Field Sensors based on Surface Plasmon Polariton Resonant Coupling, Electronics Letters, 27 (1991) 951-953.

[6] A. R. Bergh, H. C. Lefevre, and H. J. Shaw, An Overview of Fiber-Optic Gyroscopes, IEEE J. Lightwave Technology, LT-2, (1984) 91-107.

[7] N. Yamazoe and N. Miura, Environmental Gas Sensing, Sensors and Actuators B, 20 (1994) 95-102.

[8] H. Offengacher, O. S. Wolfbeis, and E. Furlinger, Fluorescence Optical Sensor for continuous Determination of Near Neutral pH Values, Snensors and Actuators, 9 (1986) 73-84.

[9] J. F. Giuliani, H. Wohltjen, and N. L. Jarvis, Reversible Optical Waveguide Sensor for Ammonia Vapors, Optics Letters, 8 (1983) 54-56.

[10] J. Homola and R. Slavik, Fibre-Optic Sensor based on Surface Plasmon Resonance, Electronics Letters, 32 (1996) 480-482.

[11] J. Homola, G. Schwotzer, H. Lehmann, R. Willsch, W. Ecke, and H. Bartelt, Fiber Optic Sensor for Adsorption Studies using Surface Plasmon Resonance, Proceedings SPIE, Vol. 2508 (1995) 324-333.

[12] T. Yoshino, K. Kurosawa, K. Itoh, and T. Ose, Fiber Optic Fabry-Perot Interferometer and its Sensor Applications, IEEE J. Quantum Electronics, QE-18 (1982) 1624-1633.

[13] A. Yariv and H. V. Winsdor, Proposal for Detection of Magnetic Fields through Magnetostrictive Perturbation of Optical Fibre, Optics Letters, 5 (1980) 87-89.

[14] W. Ecke, J. Schauer, K. Usbeck, R. Willsch, and J. P. Dakin, Improvement of the Stability of Fiber Grating Interrogation Systems, Using Active and Passive Polarization Scrambling Devices, 12th International Conference on Optical Fiber Sensors, Williamsburg, U:S.A., OSA Technical Digest Series, Vol. 16 (1987) 484-487.

[15] W. B. Spillman and D. H. McMahon, Multimode Fiber Optic Sensors based on the Photoelastic Effect, Proc. SPIE, Vol. 412 (1983) 110-114.

[16] J. P. Dakin: Optical Fiber Sensors – Principles and Applications, Proc. SPIE, Vol. 374 (1983) 172-182.

[17] P. Tobiška, D. Berková, I. Huttel, M. Chomát, and V. Matějec, Investigation of Fiber-Optic Evanescent-Wave Sensors for Detection of Liquid Hydrocarbons, Sensors and Actuators B, 51/1-3 (1998) 152-158.

[18] A. G. Mignani, M. Gacci, C. Trono, and A. Mencaglia, Optical Fibers for Monitoring the Effects of Temperature on Picture Varnishes, Proc. SPIE, Vol. 3105 (1997) 154-158.

[19] H. Raether, Surface Plasmons on Smooth and Rough Surfaces and on Gratings, Springer Verlag, Berlin, 1988.

[20] G. Boisde and A. Harmer, Chemical and Biochemical Sensing with Optical Fibers and Waveguides, Boston: Artech House, 1996.

[21] E. Engval and P. Perlmann, Enzyme-Linked Immunosorbent Assay (ELISA) – Quantitative Assay of Immunoglobulin G, Immunochmistry, 8 (1971) 871-874.

[22] R. M. Nakamura, Y. Kasahara, and G. A. Rechnitz, Eds., Immunochemical Assays and Biosensor Technology for the 1990's, Washington, DC: American Society for Microbiology (1992) 3-23.

[23] B. Liedberg, I. Lundström, E. Stenberg, Principles of Biosensing with an Extended Coupling Matrix and Surface Plasmon Resonance, Sensors And Actuators B, 11 (1993) 63-72.

[24] B. Liedberg, C. Nylander, and I. Lindström, Biosensing with Surface Plasmon Resonance-How it all Started, Biosensors Bioelectronics, 10 (1995) 1-11.

[25] W. Lukosz, Principles and Sensitivities of Integrated Optical and Surface Plasmon Sensors for Direct Affinity Sensing and Immunosensing, Biosensors and Bioelectronics, 6 (1991) 215-225.

[26] A. Brecht, J. Ingenhoff, and G. Gauglitz, Direct Monitoring of Antigen-Antibody Interactions by Spectral Interferometry, Sensors and Actuators B, 6 (1992) 96-100.

[27] E. F. Schipper, R. P. H. Kooyman, R. G. Heidemann, and J. Greve, Feasibility of Optical Waveguide Immunosensors for Pesticide Detection: Physical Aspects, Sensors and Actuators B, 24/25 (1995) 90-93.

[28] R. Cush, J. M. Cronin, W. J. Stewart, C. H. Maule, J. O. Molloy, and N. J. Goddard, The Resonant Mirror: A Novel Optical Biosensor for Direct Sensing of Biomolecular Interactions Part 1: Principle of Operation and Associated Instrumentation, Biosensors Biolelectronics, 8 (1993) 347-363.

[29] N. J. Goddard, D. Pollard-Knight, C. H. Maule, Real-Time Biomolecular Interacttion Analysis Using the Resonant Mirror Sensor, Analyst, 119 (1994) 583-588.

[30] K. S. Johnston, M. Mar, and S. Yee, Prototype of a Multi-Channel Planar Substrate SPR Probe, Sensors and Actuators B, 54 (1999) 57-65.

[31] C. Nylander, B. Liedberg, and T. Lind, Gas Detection by Means of Surface Plasmons Resonance, Sensors and Actuators, 3 (1982/83) 79-88.

[32] J. Homola, S. S. Yee, and G. Gauglitz, Surface Plasmon Resonance Sensors: Review, Sensors and Actuators B, 54 (1999) 3-15.

[33] J. Homola, I. Koudela, and S. S. Yee, Surface Plasmon Resonance Sensors based on Diffraction Gratings and Prism Couplers: Sensitivity Comparison, Sensors and Actuators B, 54 (1999), 16-24.

[34] B. Liedberg, C. Nylander, and I. Linström, Surface Plasmon Resonance for Gas Detection and Biosensing, Sensors and Actuators, 4 (1983) 299-304.

[35] M. M. B. Vidal, R. Lopez, S. Aleggeret, J. Alonso-Chamarro, I. Garces, and J. Mateo, Determination of Probable Alcohol Yield in Musts by Means of an SPR Optical Sensor, Sensors and Actuators B, 11 (1993) 455-459.

[36] L. M. Zhang, and D. Uttamchandani, Optical Chemical Sensing Employing Surface Plasmon Resonance, Electronics Letters, 23 (1988) 1469-1470.

[37] R. C. Jorgenson, and S. S. Yee, A Fiber-Optic Chemical Sensor Based on Surface Plasmon Resonance, Sensors and Actuators B, 12 (1993) 213-220.

[38] P. Pfeifer, U. Aldinger, G. Schwotzer, S. Diekmann, P. Steinrucke, Real Time Sensing of Specific Molecular Binding Using Surface Plasmon Resonance Spectroscopy, Sensors and Actuators B, 54 (1999).

[39] K. Matsubara, S. Kawata, S. Minami, Optical Chemical Sensor Based on Surface Plasmon Measurement, Applied Optics, 29 (1988) 1160-1163.

[40] A. A. Kruchynin, Y. G. Vlasov, Surface Plasmon Resonance Monitoring by Means of Polarization State Measurement in Reflected Light as the Basis of a DNA Probe Biosensor, Sensors and Actuators B, 30 (1996) 77-80.

[41] S. G. Nelson, K. S. Johnston, and S. S. Yee, High Sensitivity Surface Plasmon Resonance Sensor Based on Phase Detection, Sensors and Actuators B, 35-36 (1996) 187-191.

[42] P. I. Nikitin, A. A. Beloglazov, A. V. Kabashin, M. V. Valeiko, and V. E. Kochergin, Surface Plasmon Resonance Interferometry for Sensor Applications, 4th European Conference on Optical Chemical Sensors and Biosensors, March 1997, Munster, Germany, Book of Abstracts, 145-146.

[43] M. A. Ordal, L. L. Long, R. J. Bell, S. E. Bell, R. R. Bell, R. W. Alexander, J. Ward, and C. A. Ward, Opitcal Properties of metals Al, Co, Cu, Au, Fe, Pb, Ni, Pd, Pt, Ag, Ti, and W in the infrared and far infrared, Applied Optics, 11 (1983) 1099-1119.

[44] A. Trouillet, C. Ronot-Trioli, C. Veillas, and H. Gagnaire, Chemical Sensing by Surface Plasmon Resonance in a Multimode Optical Fibre, Pure Applied Optics, 5 (1996) 227-237.

[45] A. D. Boardman (editor), Electromagnetic Surface Modes, John Wiley & Sons, 1982.

[46] D. C. Cullen, R. G. Brown, and C. R. Lowe, Detection of Immuno-Complex Formation via Surface Plasmon Resonance on Gold-Coated Diffraction Gratings, Biosensors, 3 (1987/88) 211-225

[47] D. C. Cullen and C. R. Lowe, A Direct Surface Plasmon-Polariton Immunosensor: Preliminary Investigation of the Non-Specific Adsorption of Serum Components to the Sensor Interface, Sensros and Actuators B, 1 (1990) 576-579.

[48] P. S. Vukosic, G. P. Bryan-Brown, and J. R. Sambles, Surface Plasmon Resonance on Grating as Novel Means for Gas Sensing, Sensors and Actuators B, 8 (1992) 155-160.

[49] M. J. Jory, P. S. Vukosic, and J. R. Sambles, Development of a Prototype Gas Sensor Using Surface Plasmon Resonance on Gratings, Sensros and Actuators B, 17 (1984) 203-209.

[50] http://www.biacore.com

[51] H. Morgan, D. M. Taylor, A Surface Plasmon Resonance Immunosensor based on the Streptavidin Biotin Complex, Biosensors Bioelectronics, 7 (1992) 405-410.

[52] C. D. Bain, E. B. Troughton, Y. Y. Tao, J. Evall, G. M. Whitesides, and R. G. Nuzzo, Formation of Monolayer Films by Spontaneous Assembly of Organic Thiols from Solution onto Gold, J. American Chemical Society, 111 (1089) 321.

[53] http://www.ti.com

[55] http://www.biosensor.com

[54] http://www.biotul.com

[56] S. R. Karlsen, K. S. Johnston, S. S. Yee, and C. C. Jung, First-Order Surface Plasmon Resonance Sensor System based on a Planar Light Pipe, Sensors and Actuators B, 32 (1996) 137-141.

[57] J. Homola, and S. S. Yee, Surface Plasmon Resonance Sensor based on Planar Light Pipe: Theoretical Optimization Analysis, Sensors and Actuators B, 37 (1996) 145-150.

[58] P. V. Lambeck, Integrated Opto-Chemical Sensors, Sensors and Actuators B, 8 (1992) 103-116.

[59] J. Homola, J. Čtyroký, M. Skalský, J. Hradilová , and P. Kolářová, A Surface Plasmon Resonance Based Integrated Optical Sensor, Sensors and Actuators B, 38-39 (1997) 286-290.

[60] C. Mouvert, R. D. Harris, C. Maciag, B. J. Luff, J. S. Wilkinson, J. Piehler, A. Brecht, G. Gauglitz, R. Abuknesha, and G. Ismail, Determination of Simazine in Water Samples by Waveguide Surface Plasmon Resonance, Analytica Chimica Acta, 338 (1997) 109-117.

[61] B. J. Luff, R. D. Harris, J. S. Wilkinson, R. Wilson, and D. J. Schiffrin, Integrated-Optical Directional Coupler Biosensor, Optics Letters, 21 (1996) 618-620.

[62] R. D. Harris and J. S. Wilkinson, Waveguide Surface Plasmon Resonance Sensors, Sensors And Actuators B, 29 (1995) 261-267.

[63] C. R. Lavers and J. S. Wilkinson, A waveguide-coupled Surface-Plasmon Sensor for an Aqueous Environment, Sensors and Actuators B, 22 (1994) 75-81.

[64] J. Čtyroký, J. Homola, M. Skalský, Tuning of Spectral Operation Range of a Waveguide Surface Plasmon Resonance Sensor, Electronics Letters, 33 (1997) 1246-1248.

[65] M. N. Weiss, R. Srivastava, and H. Groger, Experimental Investigation of a Surface Plasmon-Based Integrated-Optic Humidity Sensor, Electronics Letters, 32 (1996) 842-843.

[66] A. J. C. Tubb, F. P. Payne, R. B. Millington, and C. R. Lowe, Single-Mode Optical Fibre Surface Plasma Wave Chemical Sensor, Sensors and Actuators B, 41 (1997) 71-79.

[67] J. Homola, Optical Fiber Sensor Based on Surface Plasmon Excitation, Sensors and Actuators B, 29 (1995) 213-220.

[68] R. E. Dessy, W. J. Bender, Feasibility of a Chemical Microsensor Based on Surface Plasmon Resonance on Fiber Optics Modified by Multilayer Vapor Deposition, Analytical Chemistry, 66 (1994) 963 – 970.

[69] A. W. Snyder and J. D. Love, Optical Waveguide Theory, London, England: Chapman and Hall, (1981) Chapters 12,13, and 30.

[70] A. M. Smith, Birefringence Induced by Bends and Twists in Single-Mode Optical Fiber, Applied Optics, 19 (1980) 2606-2610.

[71] M. D. Feit, and J. A. Fleck, Light Propagation in Graded-Index Optical Fibers, Applied Optics, 17 (1978) 3990.

[72] Y. Chung, and N. Dagli, An Assessment of Finite-Difference Beam Propagation Technique, IEEE Journal of Quantum Electronics, 8 (1990) 1335-1339.

[73] D. Schulz, C. Glingener, M. Bludszuweit, and E. Voges, Mixed Finite Element Beam Propagation Method, Proceedings of European Conference on Integrated Optics, Stockholm (1997), 226-229.

[74] J. Gerdes, and R. Pregla, Beam Propagation Algorithm based on the Method of Lines, J. of Optical Society of America B, 8 (1991) 389-394.

[75] G.Guekos (Ed.), Photonic Devices for Telecommnications, Springer-Verlag, Berlin, 1999.

[76] J. Homola, Fiber Optic Surface Plasmon Polarizer, PhD. thesis, IREE AS CR, Prague 1992 (in czech).

[77] J. Chilwell and I. Hodgkinson, Thin-Films Field-Transfer Matrix Theory of Planar Multilayer Waveguides and Reflection Prism-Loaded Waveguides, J. of Optical Society of America A, 1 (1984) 742-753.

[78] A. S. Sudbø, Improved Formulation of the Film Mode Matching Method for Mode Field Calculations in Dielectric Waveguides, Pure Applied Optics (Journal of European Optical Society A), 2 (1994) 381-388.

[79] J. W. Fleming, Material Dispersion in Lightguide Glasses, Electronics Letters, 14 (1978) 326-328.

[80] American Institute of Physics Handbook, 1972.

[81] J. Homola, J. Čtyroký, M. Skalský, J. Hradilová, and P. Kolářová, A Surface Plasmon Resonance Based Integrated Optical Sensor, Sensors and Actuators B, 38-39, (1997) 286-290.

[82] M. J. F. Digonnet and H. J. Shaw, Analysis of a Tunable Single Mode Optical Fiber Coupler, IEEE Journal of Quantum Electronics, GE-18 (1982) 746-754.

[83] W. K. Burns, R. P. Moeller, and Ch. Chen, Depolarization in a Single-Mode Optical Fiber, J. of Lightwave Technology, LT-1 (1983) 44-49.

[84] K. Mochizuki, Degree of Polarization in Jointed Fibers: the Lyot depolarizer, Applied Optics, 23 (1984) 3284-3288.

[85] W. K. Burns, Degree of Polarization in the Lyot Depolarizer, J. of Lightwave Technology, LT-1 (1983) 475-479.

[86] K. Böhm, K. Petermann, and D. Weidel, Performance of Lyot Depolarizers with Birefringent Single-Mode Fibers, J. of Lightwave Technology, LT-1 (1983) 71-74.

[87] Experimental experience of Dr. Ecke, IPHT, Jena, FRG.

[88] A. K. Agarwal and U. Untau, Comparative Study of Methods to Produce Stationary Mode Power Distribution for Optical Fiber Measurements, Journal of Optical Communications, 4 (1983) 126-133.

[89] M. Ikeda, A. Sugimura, and T. Ikegami, Multimode Optical Fibers: Steady State Mode Exciter, Applied Optics 15 (1976) 2116-2120.

[90] S. M. Tseng, Ch. L. Chen, Side-Polished Fibers, Applied Optics, 31 (1992) 3438-3447.

[91] M. J. F. Digonnet, J. R. Feth, L. F. Stokes, H. J. Shaw, Measurement of the Core Proximity in Polished Fiber Substrates and Couplers, Optics Letters, Vol. 10, No. 9, (1985) 463-465.

[92] C. V. Annovazzi-Lodi, S. Donati, Technology of Lapped Optical-Fiber Couplers, Journal of Optical Communications, 11 (1990) 107-121.

[93] R. Slavík, Optical Sensors with Surface Plasmons, Diploma thesis, Charles University, Prague, 1996.

[94] R. Slavík, J. Homola, and J. Čtyroký, Novel Surface Plasmon Resonance Sensor Based on Single-Mode Optical Fiber, Chemical, Biochemical, and Environmental Fiber Sensors IX, Munich, FRG, Proc. SPIE, Vol. 3105 (1997) 325-331.

[95] O. G. Leminger, R. Zengerle, Determination of Single-Mode Fiber Coupler Design Parameters from Loss Measurement, Journal of Lightwave Technology, 12 (1987) 211-213.

[96] G. M. Hale and M. R. Querry, Optical Constants of Water in the 200-nm to 200-µm Wavelength Region, Applied Optics, 12 (1973) 555-563.

[97] M. Born and E. Wolf, Principles of Optics, Pergamon Press, New York, Chapter 10, 1964.

[98] A. M. Smith, Birefringence Induced by Bends and Twists in Single-Mode Optical Fiber, Applied Optics, 19 (1980) 2606-2611.

[99] J. Sakai and T. Kimura, Birefringence and Polarization Characteristics of Single-Mode Optical Fibers Under Elastic Deformations, IEEE Journal of Quantum Electronics, QE-17 (1981) 1041-1051.

[100] E. Brynda, M. Houska, J. Škvor, and J. J. Ramsden, Immobilisation of Multilayer Bioreceptor Assemblies on Solid Substrates, Biosensors and Biolectronics, 13 (1998) 165-172.

[101] R. Slavík, J. Homola, and J. Čtyroký, Optical Fiber Surface Plasmon Resonance Sensor for an Aqueous Environment, 12th International Conference on Optical Fiber Sensors, Williamsburg, U:S.A., OSA Technical Digest Series, Vol. 16 (1987) 436-439.

[102] R. Slavík, J. Homola, and J. Čtyroký, Single-Mode Optical fiber Surface Plasmon Resonance Sensor, Sensors and Actuators B, 54 (1999) 74-79.

[103] J. Homola, R. Slavík, and J. Čtyroký, Interaction between Fiber Modes and Surface Plasmon Waves: Spectral Properties, Optics Letters, 22 (1997) 1403-1405.

[104] R. Slavík, E. Brynda, J. Homola, and J. Čtyroký, Miniature Fiber Optic Surface Plasmon Resonance Biosensor, Bios'98 – Biomedical Sensors, Fibers, and Optical Delivery Systems, Stockholm, Sweeden, Book of Abstracts 88, Proc. SPIE, Vol. 3570 (1999), 184-191.

[105] R. Slavík, J. Homola, and J. Čtyroký, Miniaturization of Fiber Optic Surface Plasmon Resonance Sensor, EUROPT(R)ODE IV, Munster, FRG, Book of Abstracts (1998), 171-172, Sensors and Actuators B, 51/1-3 (1998) 311-315.